A Measurement of the F_2 Structure Function of the Neutron and the Proton

A Dissertation

Presented to

the Faculty of the Department of Physics

University of Houston

In Partial Fulfillment

of the Requirements for the Degree

Doctor of Philosophy

by

David Alan Sanders

August 1993

A Measurement of the F_2 Structure Function of the Neutron and the Proton

David Alan Sanders

APPROVED:

Dr. Roy Weinstein, Chairman

Dr. Billy W. Mayes

Dr. Lawrence S. Pinsky

Dr. Lowell T. Wood

Dr. Roland Glowinski

Dean, College of Natural Sciences and Mathematics

Preface

This thesis was done in partial fulfillment of the requirements for a degree of Doctor of Philosophy in physics at the University of Houston. It is the result of four years of work (1989-1993) with the New Muon Collaboration at CERN. It includes the data analysis and the hardware involvement of maintaining the W67 detector system and the target moving mechanism during the 1989 running of the experiment. This thesis does not include the work done on the design, construction and testing of the ST67 detector system, the replacement for W67 in the third generation of the experiment, the SMC; nor does it include three years work on the construction and testing of detectors for the Large Volume Detector (LVD) experiment at the Gran Sasso laboratory in Italy.

This thesis is organized in the following manner:

- An introduction to the history of deep inelastic scattering experiments and the statement of the goals of the NMC experiment.
- The basic theories used in deep inelastic scattering, including the quark-parton model and perturbative QCD.
- A description of the experimental apparatus.
- A description of the data processing.
- Two chapters of results, the first dealing with the ratio F_2^n/F_2^p and the second dealing with the structure functions F_2^p and F_2^p. These chapters include a discussion of the results and a comparison of the data with the current theories.
- The conclusions.

Acknowledgments

I would like to thank Dr. Weinstein, my advisor. I would also like to thank the members of my thesis committee: Dr. Mayes, Dr. Pinsky and Dr. Wood from Physics and Dr. Glowinski from Mathematics.

I would like to thank the New Muon Collaboration for letting me take part in their experiment and for all the help that various members have given me. I would especially like to thank Dr. Ger van Middelkoop for reading my thesis and all his useful comments and corrections. I would like to thank Ewa Rondio for all the help that she has given me on my thesis and for increasing my understanding of nuclear structure functions. I would like to thank Eva Kabuß, Margriet van der Heijden and Jona Oberski for their help with this thesis and my analysis.

I would like to thank Anna Dyring for her help with the *Geometry* reprocessing, for continuing the structure function analysis and for making work (and what little free time left over) at CERN so pleasant. I would like to thank Ursula Gaul for her help on the ratio analysis and for showing me around Heidelberg. I would also like to thank the rest of the students from NMC: Maarten Ballintijn, Peter Bjorkholm, Alan Paic, Reiner Seitz, and Andreas Witzmann for their help with the analysis and for the fun after work.

I would also like to thank the SMC collaboration, especially the students for the help with work and the fun after: Lachazar, Jack, Tom, Damon, Peter, Mayda...

I would like to thank Yolande Camp for her help with the production and for putting up with my poor French. I would like to thank Jean Marc Demolis for his help in the construction of ST67 and knowing that if something had to be done he could do it. Last, but far from least, I would like to thank Liz Cumiskey who made this “stranger in a

strange land" welcome, who helped with so many things outside of her normal "job", lent her expertise, and ensured that, instead of remembering my 3-1/2 years at CERN as a time of hard lonely work, I will always look back to that time as one of pleasure and joy.

I would like to thank a few other people: S. L. Clemens for a lesson on how to use statistics, the friends I made at CERN for making life there a pleasurable experience: Jos, Sabine, Martin, Rob...

I am dedicating this thesis, in loving memory, to my mother Elaine.

A Measurement of the F_2 Structure Function of the Neutron and the Proton

An Abstract of a Dissertation

Presented to

the Faculty of the Department of Physics

University of Houston

In Partial Fulfillment

of the Requirements for the Degree

Doctor of Philosophy

by

David Alan Sanders

August 1993

Abstract

Presented in this thesis are the results and conclusions from one period of data taking by the NMC experiment at CERN. This period was conducted with a muon beam energy of 280 GeV and covered the kinematics range $0.002 \le x_{Bj} \le 0.800$ and $0.5\ (\mathrm{GeV/c})^2 \le Q^2 \le 200\ (\mathrm{GeV/c})^2$. This experiment made simultaneous high luminosity deep inelastic muon scattering measurements on liquid hydrogen and liquid deuterium targets. These measurements of the structure functions F_2^p and F_2^d, of $F_2^n - F_2^p$, of the ratio F_2^n/F_2^p and their Q^2 dependence are used to test the Gottfried sum rule and the assumption of a flavor symmetric "sea"; to determine the onset of shadowing in deuterium; to determine the difference $R^d - R^p$ between the deuteron and the proton of R, the ratio of longitudinally and transversely polarized absorption cross sections for the virtual photons.

Table of Contents:

1. Introduction

The structure of the nucleon has been studied for over two decades by experiments using scattering of electrons, muons and neutrinos. Elastic scattering measures the electromagnetic form factor of the nucleon. The cross section for elastic scattering can be expressed in terms of a constant and a form factor by[1]:

$$\frac{d\sigma}{dq^2} = \frac{4\pi\alpha^2}{q^4}\left(F\left(q^2\right)\right)^2, \tag{1.1}$$

where $\alpha = e^2/4\pi$ is the electromagnetic coupling constant, q^2 is the square of the four-momentum transfer between the initial and final states and $F\left(q^2\right)$ is the nuclear form factor. By analogy, the cross section for deep inelastic scattering can be expressed in a similar form.

Deep inelastic scattering measures the internal structure of the nucleon. The process is considered to be deep inelastic when energy is transferred to the nucleon as in the reaction $\mu + N \rightarrow \mu' + X$. The cross section of the inclusive process contains a summation of all the possible hadronic final states. Then, by analogy to elastic scattering, this cross section can be described in terms of two structure functions. For inelastic scattering they are usually chosen to be F_2 and R, where R is the ratio of longitudinally and transversely polarized absorption cross sections for the virtual photons.

The first measurements of Deep Inelastic Scattering (DIS) were performed at the Stanford Linear Accelerator Center (SLAC)[2]. These measurements were performed using a beam of electrons with energies of up to 20 GeV and have since been rewarded with the Nobel Prize (1990). The interpretation of those results has led to the Quark-Parton Model

(QPM)[3] which implies that the nucleon consists of point-like particles called partons. These partons were identified with the fractional charged quarks introduced independently, as mathematical entities, by Gell-Mann and Zweig[4]. The quantum numbers of the nucleon are determined by what are called valence quarks, q_v. The additional quark and antiquark pairs are from the Dirac sea, $q_s \overline{q}_s$, and carry the quantum numbers of the vacuum. It is customary to define the total quark distribution as the sum of those for the valence and sea quark distributions: $q = q_v + q_s$.

In the quark-parton model the structure function F_2 is dependent only on the Bjorken scaling variable x_{Bj} and the ratio R is zero. The variable x_{Bj} is the fraction of the total nucleon momentum carried by the interacting parton. x_{Bj} is defined in terms of the nucleon mass (M) and the energy (ν) and square of the four-momentum transfer (Q^2) of the virtual exchange photon, by the formula:

$$x_{Bj} \overset{Lab}{=} \frac{Q^2}{2M\nu}. \tag{1.2}$$

Further electron deep inelastic scattering measurements were made at SLAC[5], and experiments were also performed using muon and neutrino beams. The muon DIS experiments include two experiments with high statistical accuracy conducted at the Conseil Européen pour la Recherche Nucléaire (CERN). These were the European Muon Collaboration (EMC)[6] and the Bologna-CERN-Dubna-Mainz-Saclay (BCDMS)[7] group. At Fermi National Accelerator Laboratory (FNAL) a muon experiment was done by a Chicago-Harvard-Illinois-Oxford (CHIO)[8] group, which had lower statistics. Neutrino DIS experiments include two experiments conducted at CERN, BEBC[9] and, with high statistics, CDHSW[10]. At FNAL the CCFR[11] experiment was also done with high

statistics. These experiments are given in table 1.1, (those experiments with the lower statistics are denoted by an *).

Table 1.1:
Previous Deep Inelastic Experiments

Electron	Muon	Neutrino
SLAC[5]	EMC[6] (CERN)	*BEBC[9] (CERN)
	BCDMS[7] (CERN)	CDHSW[10] (CERN)
	*CHIO[8] (FNAL)	CCFR[11] (FNAL)

The SLAC[12], BCDMS[6], NMC[13] and re-analyzed EMC-NA2[14] results are shown in figure 1.1. It was observed that the structure function F_2 was also slightly dependent on Q^2, where Q^2 is defined as the negative of the four-momentum transfer. This non zero slope of the structure function F_2 is a violation of Bjorken scaling and has led to the inclusion in the theories concerning DIS of effects from the strong nuclear force. The theory that describes the strong interactions is called Quantum Chromodynamics (QCD)[15]. It is built by analogy to the theory describing electromagnetic interactions, Quantum electrodynamics (QED)[16]. In a domain where the strong coupling constant, α_S, is small; perturbation theory can be used to describe the effects of strong interactions on the quark distributions. The theory of perturbative QCD[17] predicts a weak dependence on Q^2 of the structure function F_2. The electron, neutrino and muon experimental results are in good agreement with this theory.

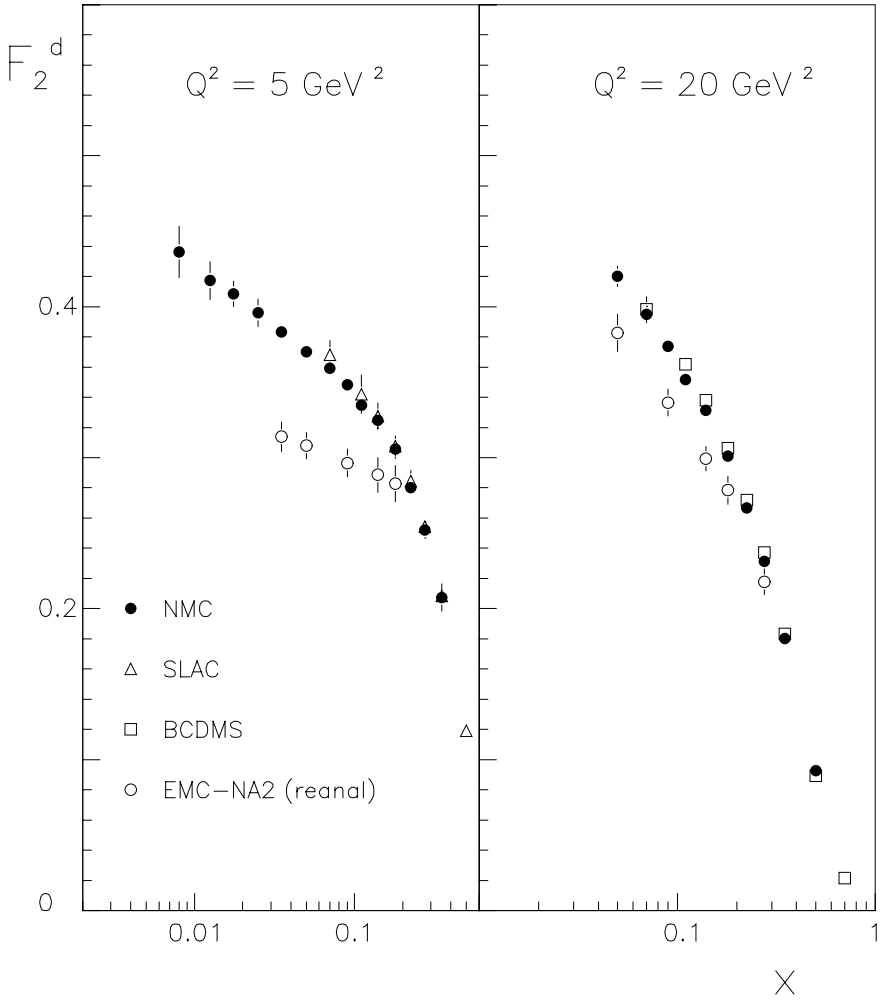

Figure 1.1: The structure function F_2^d versus x_{Bj}.
Showing the regions of overlap for
the EMC, NMC and SLAC experiments (at $Q^2 = 5\ (\mathrm{GeV/c})^2$) and for
the BCDMS, EMC and NMC experiments (at $Q^2 = 20\ (\mathrm{GeV/c})^2$).

However there was a disagreement of the results as seen in figure 1.1 at $Q^2 = 20\ (\mathrm{GeV/c})^2$, between the two muon experiments at CERN, the EMC and BCDMS.

While their results individually agreed with perturbative QCD, there were discrepancies between the experimental results. The SLAC data could not resolve the difference because, as seen in figure 1.2, there was not enough overlap of the range of the kinematical variables x_{Bj} and Q^2. Therefore a new experiment was proposed to CERN, by the New Muon Collaboration (NMC), which was expected to resolve the differences.

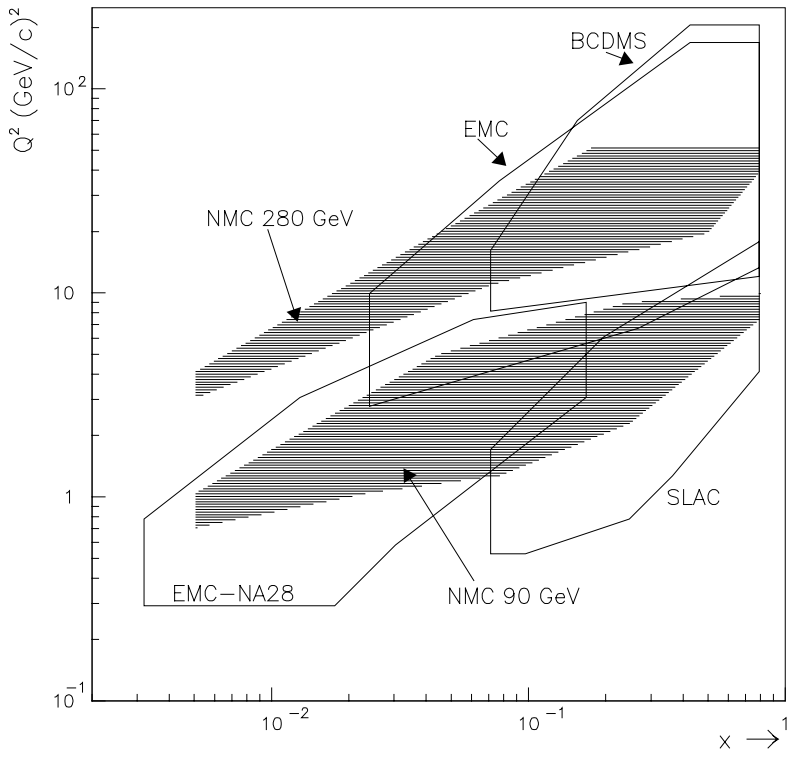

Figure 1.2:
The kinematical region of x_{Bj} and Q^2 covered[18] by the
BCDMS, EMC, EMC-NA28[19], NMC and SLAC experiments.

In figure 1.2 the shaded areas have been explored by the NMC experiment at two separate beam energies. These two energies, along with the future analysis of data from

the 120 and 200 GeV beam energies, provide an overlap in the range of the kinematical variables x_{Bj} and Q^2. The NMC experiment is the major subject of this thesis.

The NMC proposed to study deep inelastic muon-nucleon scattering in a wide range of Q^2 (0.5 - 200$\left(\mathrm{GeV/c}\right)^2$) and a wide range of x_{Bj} (0.002 - 0.8). This experiment used muon energies of 90, 120, 200 and 280 GeV incident on a variety of targets (H, D, He, Li, Be, C, Ca, Fe, Sn, Pb). The NMC experiment collected data from 1986 to 1989. Its main goals were:

1) To make a simultaneous high luminosity measurement of the structure functions F_2 and *R* of hydrogen and deuterium.

2) To perform a high precision measurement of the ratio F_2^n/F_2^p and to test the Gottfried sum rule[20].

3) To investigate the *A* and Q^2 dependence of the "EMC effect"[21].

4) To study the gluon distribution in nucleons and nuclei through J/ψ production[22].

In this thesis only the first two points will be discussed. In particular the discussion will center on the data from the hydrogen and deuterium targets, for the period of data taking called P3A89, which was a period in 1989 involving a muon beam energy of 280 GeV. During this period, NMC made a high luminosity measurement of the structure function F_2, simultaneously on both hydrogen and deuterium targets.

In NMC, the large range of x_{Bj}, in particular going down to very small values of x_{Bj}, provides a substantial improvement in the accuracy of the knowledge of the structure functions F_2^p and F_2^d, of $F_2^n - F_2^p$, of the ratio F_2^n/F_2^p and their Q^2 dependence. Here both

the difference $F_2^n - F_2^p$ and the structure function ratio F_2^n/F_2^p are derived from the relation:

$$\frac{F_2^n}{F_2^p} = 2\frac{F_2^d}{F_2^p} - 1. \tag{1.3}$$

The validity of the Gottfried sum rule and the assumption of a flavor symmetric sea can also be tested. The data also allows further tests of perturbative QCD, including higher order (called higher twist) effects. The data from DIS experiments is widely used in determinations of the quark and gluon distributions. Therefore studies of the x_{Bj} and Q^2 distributions of quarks and gluons with reduced experimental uncertainties, as well as of the ratio of the down to up quark distributions in the valence region can be made. The NMC data is used to put strong constraints on the parametrization of parton distributions. An example of the wide range of possible distributions, made without the low x_{Bj} constraint from the NMC data, is shown by figure 1.3, generated by the CERN program library's PDFLIB[23].

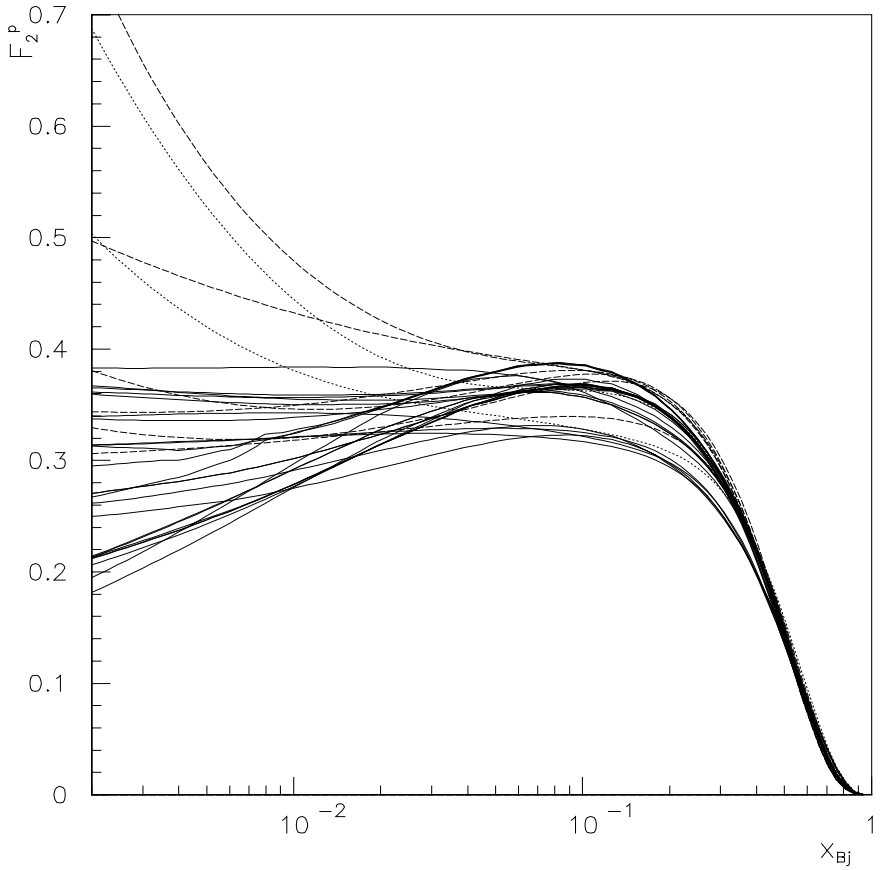

Figure 1.3:
Parametrizations of F_2^p from the program PDFLIB.

References: Chapter 1

---

1 D. H. Perkins, *Introduction to High Energy Physics*, Addison-Wesley, Menlo Park (1987).

2 SLAC-MIT, E. D. Bloom *et al*., *Phys. Rev. Lett.* **23** (1969) 930;
SLAC-MIT, M. Briedenbach *et al*., *Phys. Rev. Lett.* **23** (1969) 935.

3 J. D. Bjorken and E. A. Paschos, *Phys. Rev.* **185** (1969) 1975;
R. P. Feynman, *Photon-hadron interactions,* Benjamin, New York (1972).

4 M. Gell-Mann, *Phys. Lett.* **8** (1964) 214;
G. Zweig, CERN Reports 8182/TH 401, 8419/TH 412 (1964).

5 A. Bodek *et al*., *Phys. Rev. D* **20** (1979) 1471;
M. D. Mesteyer *et al*., *Phys. Rev. D* **27** (1983) 285.

6 EMC, J. J. Aubert *et al*., *Nucl. Phys.* **B259** (1985) 189;
EMC, J. J. Aubert *et al*., *Nucl. Phys.* **B293** (1987) 740.

7 BCDMS, A. C. Benvenuti *et al*., *Phys. Lett.* **B223** (1989) 485;
BCDMS, A. C. Benvenuti *et al*., *Phys. Lett.* **B237** (1990) 592.

8 CHIO, Collaboration, B. A. Gordon *et al*., *Phys. Rev. D* **20** (1979) 2645.

9 BEBC, K. Varvell *et al*., *Z. Physik* **C36** (1987) 1;
CERN WA25 and WA59, J. Guy *et al*., *Z. Physik* **C36** (1987) 337.

10 P. Berge *et al*., *Z. Physik* **C49** (1991) 187.

11 CCFR, D. B. MacFarlane *et al*., *Z. Physik* **C26** (1984) 1.

12 L. Whitlow *et al., Phys. Lett.* **B282** (1992) 475.

13 NMC, P. Amaudruz *et al., Phys. Lett.* **B295** (1992) 159.

14 K. Bazizi and S. J. Wimpenny, preprint UCR/DIS/91-02;
H. Peschel, Ph. D. thesis, University of Wuppertal (1990).

15 M. R. Pennington, "Cornerstones of QCD." *Rep. Prog. Phys.* **46** (1983) 393.

16 R. P, Feynman, *Quantum electrodynamics*, Benjamin, New York (1962).

17 G. Altarelli and G. Parisi, *Nucl. Phys.* **B126** (1977) 298.

18 I. G. Bird, Ph. D. thesis, Vrije Universiteit, Amsterdam (1992).

19 EMC, M. Arneodo *et al., Nucl. Phys.* **B333** (1990) 1.

20 K. Gottfried, *Phys. Rev. Lett.* **18** (1967) 1174.

21 EMC, J. J. Aubert *et al., Phys. Lett.* **B123** (1983) 275.

22 NMC, D. Allasia, *et al., Phys. Lett.* **B258** (1991) 493.

23 H. Plothow-Besch, "Parton Density Functions", Proc. 3rd Workshop on detector and Event Simulations in High Energy Physics, Amsterdam, 8-12 April 1991;
Program PDFLIB; CERN Program Library Pool W5051 (1991).

2. Theory

2.1. Deep inelastic scattering

The lowest order Feynman diagram[1] for deep inelastic scattering of a charged lepton on a nucleon is pictured in figure 2.1 for the case of muons, in the interaction $\mu + N \rightarrow \mu' + X$.

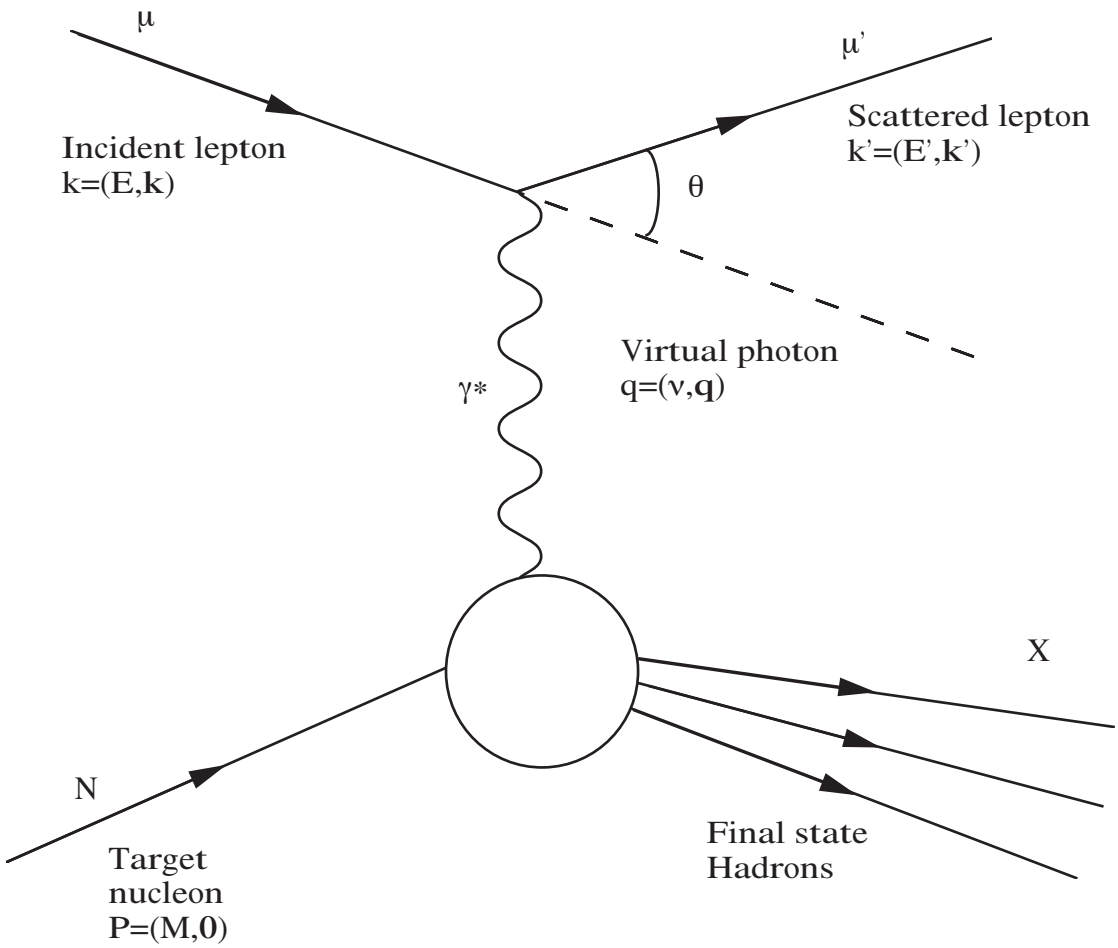

Figure 2.1:
The One-Photon exchange interaction.
Four-vectors are noted, e.g. as $P = (E, \mathbf{p})$.

In this process the nucleus breaks up and details of the final state, consisting of hadrons denoted by *X*, are not considered in this thesis.

This process has the electromagnetic interaction mediated by a single virtual photon, γ^*. The momenta of the incoming and outgoing muon are described by four-vectors $k = (E, \mathbf{k})$ and $k' = (E', \mathbf{k}')$. The four-momentum of the nucleon is given by $p = (M, \mathbf{0})$, because the nucleon, of mass M, is assumed to be initially at rest in the laboratory coordinate system. The four-momentum of the virtual photon is given by $q = (\nu, \mathbf{q})$, where the momentum transfer q is defined by $q = k - k'$. It is customary to define Q^2 as the negative of the square of the four-momentum transfer[1], i.e.:

$$Q^2 \equiv -q^2 = -(k - k')^2 \overset{Lab}{\approx} 4EE' \sin^2 \frac{\theta}{2}, \tag{2.1}$$

where θ is the scattering angle of the muon in the laboratory reference frame. The energy of the virtual photon is given by[1]:

$$\nu = \frac{p \cdot q}{M} \overset{Lab}{=} E - E'. \tag{2.2}$$

Eqs. 2.1 and 2.2 relate Q^2 and ν to measurements in the laboratory coordinate system. This permits the calculation of x_{Bj}, y or W^2, given below from the measured values of energy, momentum and the scattering angle. Where x_{Bj} is the fraction of the nucleon momentum carried by the struck quark and y is the fraction of the total energy transferred by the virtual photon.

The Lorentz invariant scaling parameters, the Bjorken variable x_{Bj}, and y are given by[1]:

$$x_{Bj} = \frac{Q^2}{2P\cdot q} \overset{Lab}{=} \frac{Q^2}{2M\nu}, \tag{2.3}$$

$$y = \frac{p\cdot q}{p\cdot k} \overset{Lab}{=} \frac{\nu}{E}. \tag{2.4}$$

The invariant mass of the final hadronic system $W = M^{*}_{Hadronic}$ is defined as[1]:

$$W^2 = \left(P+q\right)^2 = M^2 + 2P\cdot q + q^2 \overset{Lab}{=} M^2 + 2M\nu - Q^2. \tag{2.5}$$

Because W^2 is given in terms of the same kinematical variables as the leptons, the entire kinematics of the interaction is determined from a measurement of the kinematic variables of the incident and scattered leptons. The ranges of these variables defined above for deep inelastic scattering are:

$$0 < y < 1,$$
$$0 < x_{Bj} < 1,$$
$$0 < \nu < E,$$
$$0 < Q^2 < 2M\nu \le 2M\,\nu_{Max.} < 2ME.$$

Throughout this thesis the system of units are used where $\hbar = c = 1$ and energy is measured in GeV, momentum in GeV/c and mass in GeV/c^2.

The cross section for elastic scattering can be expressed in terms of a constant and a form factor by[2]:

$$\frac{d\sigma}{dq^2} = \frac{4\pi\alpha^2}{q^4}\left(F\left(q^2\right)\right)^2, \tag{2.6}$$

where $\alpha = e^2/4\pi$ is the electromagnetic coupling constant and $F(q^2)$ is the nuclear form factor. By analogy, the cross section for deep inelastic scattering can be expressed in a similar form.

The cross section for the one-photon exchange may be expressed in terms of α, the leptonic and hadronic tensors $L_{\mu\nu}$ and $W^{\mu\nu}$, and by Q^2, E and E' by the expression[1]:

$$\frac{d^2\sigma}{d\Omega dE'} = \frac{\alpha^2}{Q^4}\frac{E'}{E}L^{\mu\nu}W_{\mu\nu}. \tag{2.7}$$

The leptonic tensor is defined by[1]:

$$L^{\mu\nu} = \frac{1}{2}\sum_{s,s'}\left[\bar{u}(k',s')\gamma^{\mu}u(k,s)\right]\left[\bar{u}(k',s')\gamma^{\nu}u(k,s)\right]^{*}, \tag{2.8}$$

where s and s' are the respective spins of the initial and final states and $\bar{u}(k',s')\gamma^{\mu}u(k,s)$ is the electromagnetic current of the lepton[1] (in this case a muon.) Because the muon can be treated as a true Dirac point particle the leptonic tensor can be explicitly calculated. It is given by[1]:

$$L^{\mu\nu} = 2k^{\mu}k'^{\nu} + 2k'^{\mu}k^{\nu} - Q^2 g^{\mu\nu}. \tag{2.9}$$

While the leptonic tensor may be exactly calculated from QED, the hadronic tensor is more complicated, requiring integration over all the final hadronic states. Thus the hadronic tensor is less well know, since it involves expectation values of currents. It is given by[1] the expression:

$$W_{\mu\nu} = \frac{1}{4\pi M}\frac{1}{2}\sum_{s,s'}\int\frac{d^3p'}{(2\pi)^3 2p'_0}\langle P,s|\tilde{J}^{\dagger}_{\mu}|p',s'\rangle\langle p',s'|\tilde{J}_{\nu}|P,s\rangle(2\pi)^4\delta^4(P+q-p'), \tag{2.10}$$

where s and s' are the respective spins of the initial and final hadronic states and $\langle P,s|\tilde{J}_\mu^\dagger|p',s'\rangle$ is the matrix element for the electromagnetic current J between the nucleon and the final state X. The tensor $W_{\mu\nu}$ is hermitian and gauge invariant and, for an unpolarized target, symmetric. Using the most general form for the current J and assuming invariance under parity and time reversal, the tensor can be written as a linear combination of two independent terms, W_1 and W_2. For unpolarized targets a summation should be made over the final spin states. The hadronic tensor is then given by[1]:

$$W_{\mu\nu} = \left(g_{\mu\nu} - \frac{q_\mu q_\nu}{q^2} \right) W_1\left(\nu, Q^2\right) + \left(P_\mu - q_\mu \frac{q \cdot P}{q^2} \right)\left(P_\nu - q_\nu \frac{q \cdot P}{q^2} \right) W_2\left(\nu, Q^2\right). \tag{2.11}$$

Contracting the leptonic and hadronic tensors and using eqs. 2.1-3 and 2.7, the double differential cross section in the laboratory frame is given by[1]:

$$\frac{d^2\sigma}{d\Omega dE'} = \frac{4\alpha^2 E'^2}{Q^4}\left[W_2\left(\nu, Q^2\right)\cos^2\frac{\theta}{2} + 2\,W_1\left(\nu, Q^2\right)\sin^2\frac{\theta}{2} \right]. \tag{2.12}$$

The two functions W_1 and W_2 describe the structure of the nucleon and must be determined by experiment. In the present work we follow the convention to express the cross section in terms of the dimensionless structure functions F_1 and F_2 defined as[3]:

$$F_1\left(x_{Bj}, Q^2\right) = M\,W_1\left(\nu, Q^2\right), \tag{2.13}$$

$$F_2\left(x_{Bj}, Q^2\right) = \nu\,W_2\left(\nu, Q^2\right). \tag{2.14}$$

This leads to the expression of the double differential cross section, given in terms of x_{Bj} and Q^2:

$$\frac{d^2\sigma}{dQ^2 dx_{Bj}} = \frac{4\pi\alpha^2}{Q^4}\frac{F_2\left(x_{Bj},Q^2\right)}{x_{Bj}}\frac{E'}{E}\left[\cos^2\frac{\theta}{2} + 2\frac{\nu}{M}\frac{F_1\left(x_{Bj},Q^2\right)}{F_2\left(x_{Bj},Q^2\right)}\sin^2\frac{\theta}{2}\right], \tag{2.15}$$

which, using the equations 2.1-2.4, reduces to the expression:

$$\frac{d^2\sigma}{dQ^2 dx_{Bj}} = \frac{4\pi\alpha^2}{Q^4}\frac{F_2\left(x_{Bj},Q^2\right)}{x_{Bj}}\left[\left(1 - y - \frac{Q^2}{4E^2}\right) + \frac{2x_{Bj}F_1\left(x_{Bj},Q^2\right)}{F_2\left(x_{Bj},Q^2\right)}\frac{y^2}{2}\right], \tag{2.16}$$

where x_{Bj}, Q^2 and y are no longer independent variables.

In order to express the differential cross section in terms of primarily one structure function, $F_2\left(x_{Bj},Q^2\right)$, we can rewrite the cross section by assuming that it can be expressed by the absorption cross sections for the longitudinally (σ_L) and transversally (σ_T) polarized photon. For this purpose these cross sections are defined as[1]:

$$\sigma_T \equiv \frac{1}{2}\left(\sigma_+^{total} + \sigma_-^{total}\right) = \frac{4\pi^2\alpha W_1\left(x_{Bj},Q^2\right)}{\left(\nu - Q^2/2M\right)}, \tag{2.17}$$

$$\sigma_L \equiv \sigma_0^{total} = \frac{4\pi^2\alpha}{\left(\nu - Q^2/2M\right)}\left[\left(1 + \frac{\nu^2}{Q^2}\right)W_2\left(x_{Bj},Q^2\right) - W_1\left(x_{Bj},Q^2\right)\right]. \tag{2.18}$$

Using eqs. 2.1, 2.13 and 2.14 and by introducing the ratio $R\left(x_{Bj},Q^2\right)$ of the longitudinal and transverse absorption cross sections, where:

$$R\left(x_{Bj},Q^2\right) = \frac{\sigma_L}{\sigma_T} = \left(1 + \frac{4M^2x_{Bj}^2}{Q^2}\right)\frac{F_2\left(x_{Bj},Q^2\right)}{2x_{Bj}F_1\left(x_{Bj},Q^2\right)} - 1, \tag{2.19}$$

one can write the double differential cross section for the one-photon exchange in terms of $F_2\left(x_{Bj},Q^2\right)$ and $R\left(x_{Bj},Q^2\right)$ in the form:

$$\frac{d^2\sigma}{d\,x_{Bj}\,d\,Q^2}=\frac{4\pi\alpha^2 F_2\left(x_{Bj},Q^2\right)}{Q^4\,x_{Bj}}\left[1-y-\frac{Q^2}{4\,E^2}+\frac{y^2+Q^2/E^2}{2\left(1+R\left(x_{Bj},Q^2\right)\right)}\right]. \tag{2.20}$$

$R\left(x_{Bj},Q^2\right)$ implicitly includes the structure function $F_1\left(x_{Bj},Q^2\right)$.

2.2. The Quark-Parton model

Within the quark-parton model the deep inelastic cross section is described by as the incoherent sum of elastic scattering from point-like particles inside the nucleon, which are called partons. In this picture the partons are considered to be quasi free, even though they are bound by the strong nuclear force. In this model the parton mass can be neglected and the partons are considered to move parallel to the nucleon, each carrying a fraction of the total nucleon momentum. The Feynman diagram for the elastic scattering off a point-like parton within a nucleon is shown in figure 2.2, where the parton has initial momentum *p*, a fraction of the total nucleon momentum *P*.

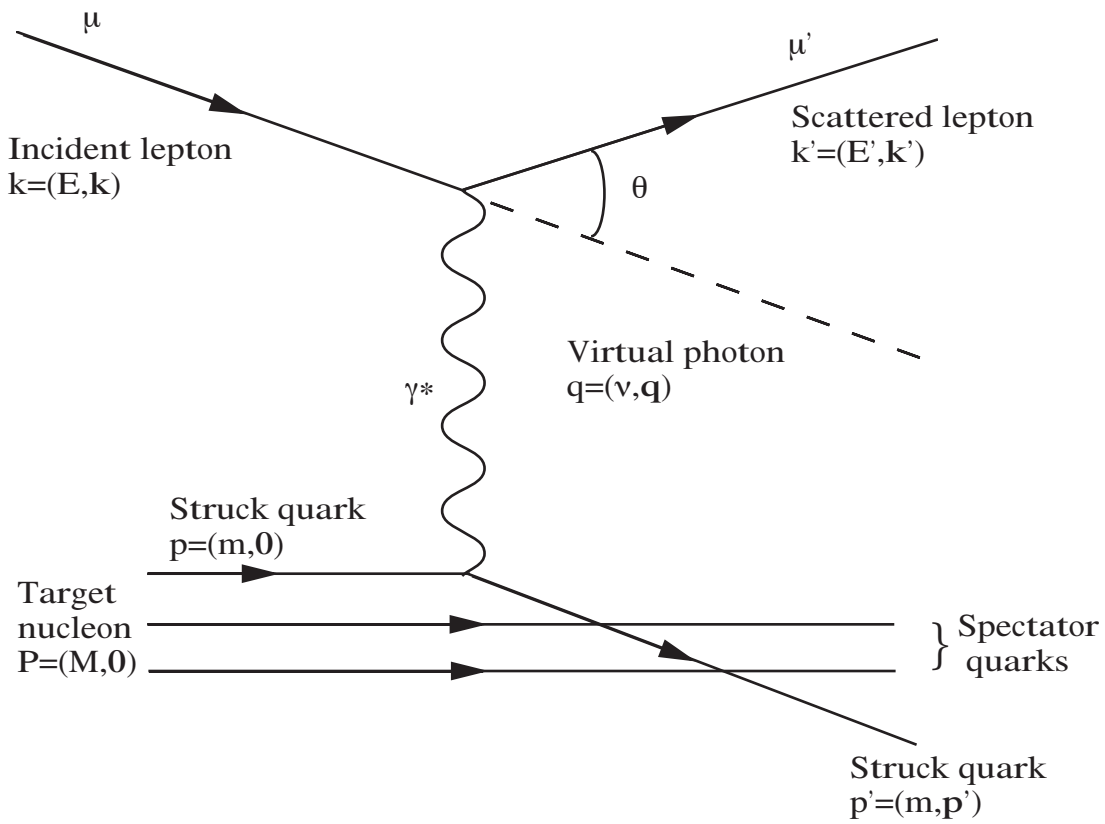

Figure 2.2:
The Quark-Parton Model.

By conservation of the four-momentum it follows for the final parton momentum p' that:

$$p'^2 = p^2 + 2p\cdot q + q^2. \tag{2.21}$$

Since this is an elastic scattering one has $p'^2 = p^2$ so that with equation 2.21 this leads to $2p\cdot q = -q^2$. From equations 2.1 and 2.3 one obtains $2p\cdot q = -q^2 = x_{Bj}2P\cdot q$. Therefore x_{Bj} is the fraction of the total nucleon momentum carried by the interacting parton.

In the quark-parton model, because the structure function F_2 is only a function of x_{Bj}, $F_2\left(x_{Bj},Q^2\right) = F_2\left(x_{Bj}\right)$. This implies that the partons are spin 1/2 point-like fermions.

In the Bjorken, or infinite momentum, limit where both $Q^2 \to \infty$ and $\nu \to \infty$ while $x_{Bj} = Q^2/2M\nu$ remains finite, the longitudinal absorption cross section, σ_L, vanishes. This means that $R \xrightarrow{Q^2 \to \infty} 0$ and consequently the relation between F_1 and F_2, in the limit $Q^2 \to \infty$, simplifies to the Callan-Gross relation[4]: $F_2(x_{Bj}) = 2\,x_{Bj} F_1(x_{Bj})$. The partons, discovered experimentally by the observation of scaling in the measurement of the structure function[5], have been identified with the fractionally charged quarks postulated by Gell-Mann and Zweig[6]. The charge, spin and flavor of the six expected quarks are given in table 2.1. While six quarks are expected by present theory, so far only the first five have been observed experimentally.

Table 2.1: The quark quantum numbers

Flavor	**u**p	**d**own	**s**trange	**c**harm	**b**ottom	**t**op*
Charge	+2/3	-1/3	-1/3	+2/3	-1/3	+2/3
Spin	1/2	1/2	1/2	1/2	1/2	1/2
Baryon number	1/3	1/3	1/3	1/3	1/3	1/3
Isospin (I_3)	+1/2	−1/2	0	0	0	0

*not yet observed by experiments.

In this model, the proton is made up of three quarks, two "up" quarks and one "down" quark; while the neutron is made from two "down" quarks and one "up" quark.

The nucleon quantum numbers are determined by what are called valence quarks, q_v. Additional quark and antiquark pairs, from the Dirac sea, $q_s \overline{q}_s$, carry the quantum numbers of the vacuum. The quark sea is made up of all flavors but, at the energies available to this experiment, only "up", "down", "strange" and "charm" quarks are expected to contribute. The masses of the “top” and “bottom” quarks are so large that

quark-antiquark pairs of these quarks are highly suppressed. In the QPM, the total quark momentum distribution is the sum of those for the valence and sea quark distributions:

$$q(x_{Bj}) = q_v(x_{Bj}) + q_s(x_{Bj}). \tag{2.22}$$

Since the valence quarks are not accompanied by antiquarks, the valence quark distribution is the difference between the quark and antiquark distributions. Therefore:

$$q_v(x_{Bj}) = q(x_{Bj}) - \overline{q}(x_{Bj}), \tag{2.23}$$

which implies that $q_s(x_{Bj}) = \overline{q}(x_{Bj})$.

The deep inelastic scattering cross section for muons is interpreted in the quark-parton model[7] as the summation of the elastic scattering from the quarks and antiquarks within the nucleon. The structure function F_2, in the limit $Q^2 \to \infty$, can be written[1] as x_{Bj} times the sum over the number of flavors N_f of the quark and antiquark probability distributions, $q_i(x_{Bj})$ and $\overline{q}_i(x_{Bj})$, weighted with the square of the quark charge, e_i^2:

$$F_2(x_{Bj}) = x_{Bj} \sum_{i=1}^{N_f} e_i^2 \left[q_i(x_{Bj}) + \overline{q}_i(x_{Bj}) \right]. \tag{2.24}$$

Then the structure function F_2 for the proton becomes[1]:

$$F_2^p(x_{Bj}) = x_{Bj} \left[\frac{4}{9}\left\{ u(x_{Bj}) + \overline{u}(x_{Bj}) \right\} + \frac{1}{9}\left\{ d(x_{Bj}) + \overline{d}(x_{Bj}) \right\} + \frac{1}{9}\left\{ s(x_{Bj}) + \overline{s}(x_{Bj}) \right\} + \frac{4}{9}\left\{ c(x_{Bj}) + \overline{c}(x_{Bj}) \right\} \right] . \tag{2.25}$$

Using isospin symmetry arguments, the structure function F_2 for the neutron is given by:

$$F_2^n(x_{Bj}) = x_{Bj}\left[\frac{1}{9}\left\{u(x_{Bj}) + \bar{u}(x_{Bj})\right\} + \frac{4}{9}\left\{d(x_{Bj}) + \bar{d}(x_{Bj})\right\} + \frac{1}{9}\left\{s(x_{Bj}) + \bar{s}(x_{Bj})\right\} + \frac{4}{9}\left\{c(x_{Bj}) + \bar{c}(x_{Bj})\right\}\right] \quad . \tag{2.26}$$

For neutrino-proton scattering the structure function F_2 becomes:

$$F_2^{\nu p}(x_{Bj}) = 2\,x_{Bj}\left[d(x_{Bj}) + \bar{u}(x_{Bj}) + s(x_{Bj}) + \bar{c}(x_{Bj})\right], \tag{2.27}$$

and, by similar isospin symmetry arguments, the structure function F_2 for the neutron becomes:

$$F_2^{\nu n}(x_{Bj}) = F_2^{\bar{\nu} p}(x_{Bj}) = 2\,x_{Bj}\left[u(x_{Bj}) + \bar{d}(x_{Bj}) + \bar{s}(x_{Bj}) + c(x_{Bj})\right]. \tag{2.28}$$

In neutrino-nucleon scattering one also has to take into account charged current interactions, the exchange of the charged weak vector boson $W^{\pm}$. This exchange results in the change of charge of the lepton and hadron. To describe the charged current interaction a third structure function, $x_{Bj}F_3(x_{Bj})$, is introduced. This structure function is given for the proton as:

$$x_{Bj}F_3^{\nu p}(x_{Bj}) = 2\,x_{Bj}\left[d(x_{Bj}) - \bar{u}(x_{Bj}) + s(x_{Bj}) - \bar{c}(x_{Bj})\right], \tag{2.29}$$

and for the neutron by:

$$-x_{Bj}F_3^{\nu n}(x_{Bj}) = x_{Bj}F_3^{\bar{\nu} p}(x_{Bj}) = 2\,x_{Bj}\left[u(x_{Bj}) - \bar{d}(x_{Bj}) - \bar{s}(x_{Bj}) + c(x_{Bj})\right]. \tag{2.30}$$

The quark-parton model predicts that the ratio F_2^n/F_2^p should approach unity in the limit $x_{Bj} \to 0$, because at x_{Bj}=0 the valence quark distributions are expected to vanish and the sea is assumed to be flavor symmetric. (See equations 2.22, 2.23, 2.25 and 2.26) Any difference from unity in the ratio F_2^n/F_2^p, in the low x_{Bj}, region would be attributed

by the theory to the residual valence quark distributions and to possible asymmetries in the quark sea.

However at low x_{Bj}, a "shadowing" has been observed in the ratios of nuclei scattering cross sections with respect to deuterium[8]. The cross section ratio σ_d/σ_p is given in terms of the proton and deuteron cross sections, σ_p and σ_d respectively. The cross section for the neutron, ignoring the effects of nuclear binding, is calculated to be $\sigma_n = \sigma_d - \sigma_p$. This "shadowing" is seen as a reduction of the total scattering cross section of nucleons bound in the nucleus relative to the cross section measured for free nucleons.

Shadowing may also be observed for deuterium, thus effecting the ratio σ_n/σ_p, where the ratio σ_n/σ_p is conventionally defined as:

$$\frac{\sigma_n}{\sigma_p} = \frac{\sigma_d - \sigma_p}{\sigma_p} = \frac{\sigma_d}{\sigma_p} - 1. \tag{2.31}$$

Real-photon experiments have also been done for γ - d and γ - p scattering[9]. In these cases, by definition Q^2=0 and hence x_{Bj}=0, a depletion in the ratio σ_d/σ_p has been observed. For photon energies of 16-18 GeV the measured ratio σ_n/σ_p, as determined from the ratio σ_d/σ_p using equation 2.29, of the scattering cross sections was found to be 0.898(15). This significant deviation from unity at x_{Bj}=0 has been interpreted in terms of the shadowing of real photons in deuterium[10]. If one assumes that the total cross section is continuous between real and virtual photons , shadowing would be expected for virtual photons at very low x_{Bj}.

In the region x_{Bj}>0.3 the valence quarks dominate. In this region all the structure functions can be approximated by functions of only the two valence quarks $u_v\left(x_{Bj}\right)$ and

$d_v(x_{Bj})$. In this region the formulae for the structure functions, given in terms of the quark density functions reduce to the following formulae; for neutrino scattering:

$$F_2^{\nu n}(x_{Bj}) \to 2\,x_{Bj}\,u_v(x_{Bj}), \tag{2.32}$$

$$F_2^{\nu p}(x_{Bj}) \to 2\,x_{Bj}\,d_v(x_{Bj}), \tag{2.33}$$

while for muon scattering:

$$F_2^{n}(x_{Bj}) \to x_{Bj}\left[\frac{1}{9}u_v(x_{Bj}) + \frac{4}{9}d_v(x_{Bj})\right], \tag{2.34}$$

$$F_2^{p}(x_{Bj}) \to x_{Bj}\left[\frac{4}{9}u_v(x_{Bj}) + \frac{1}{9}d_v(x_{Bj})\right]. \tag{2.35}$$

Then the formulae for the ratios $F_2^{\nu n}/F_2^{\nu p}$ and F_2^{n}/F_2^{p} reduce, in terms of $u_v(x_{Bj})$ and $d_v(x_{Bj})$, to the two following equations:

$$\frac{F_2^{\nu n}}{F_2^{\nu p}}(x_{Bj}) \to \frac{u_v(x_{Bj})}{d_v(x_{Bj})}, \tag{2.36}$$

$$\frac{F_2^{n}}{F_2^{p}}(x_{Bj}) \to \left[1 + 4\frac{d_v(x_{Bj})}{u_v(x_{Bj})}\right] \Big/ \left[4 + \frac{d_v(x_{Bj})}{u_v(x_{Bj})}\right]. \tag{2.37}$$

The results from both muon (BCDMS)[11] and neutrino (WA21 and WA25)[12] deep inelastic scattering experiments can be compared with each other by using the results from the neutrino scattering experiments and eq. 2.36. These neutrino results are then recalculated in the form:

$$\left[1+4\frac{d_v\left(x_{Bj}\right)}{u_v\left(x_{Bj}\right)}\right]\Big/\left[4+\frac{d_v\left(x_{Bj}\right)}{u_v\left(x_{Bj}\right)}\right], \tag{2.38}$$

and compared with the ratio F_2^n/F_2^p from muon experiments. In figure 2.3 these results are shown. The results of neutrino and muon scattering experiments are consistent for x_{Bj}>0.3 but diverge at lower values of x_{Bj} due to the influence of the quark-antiquark sea.

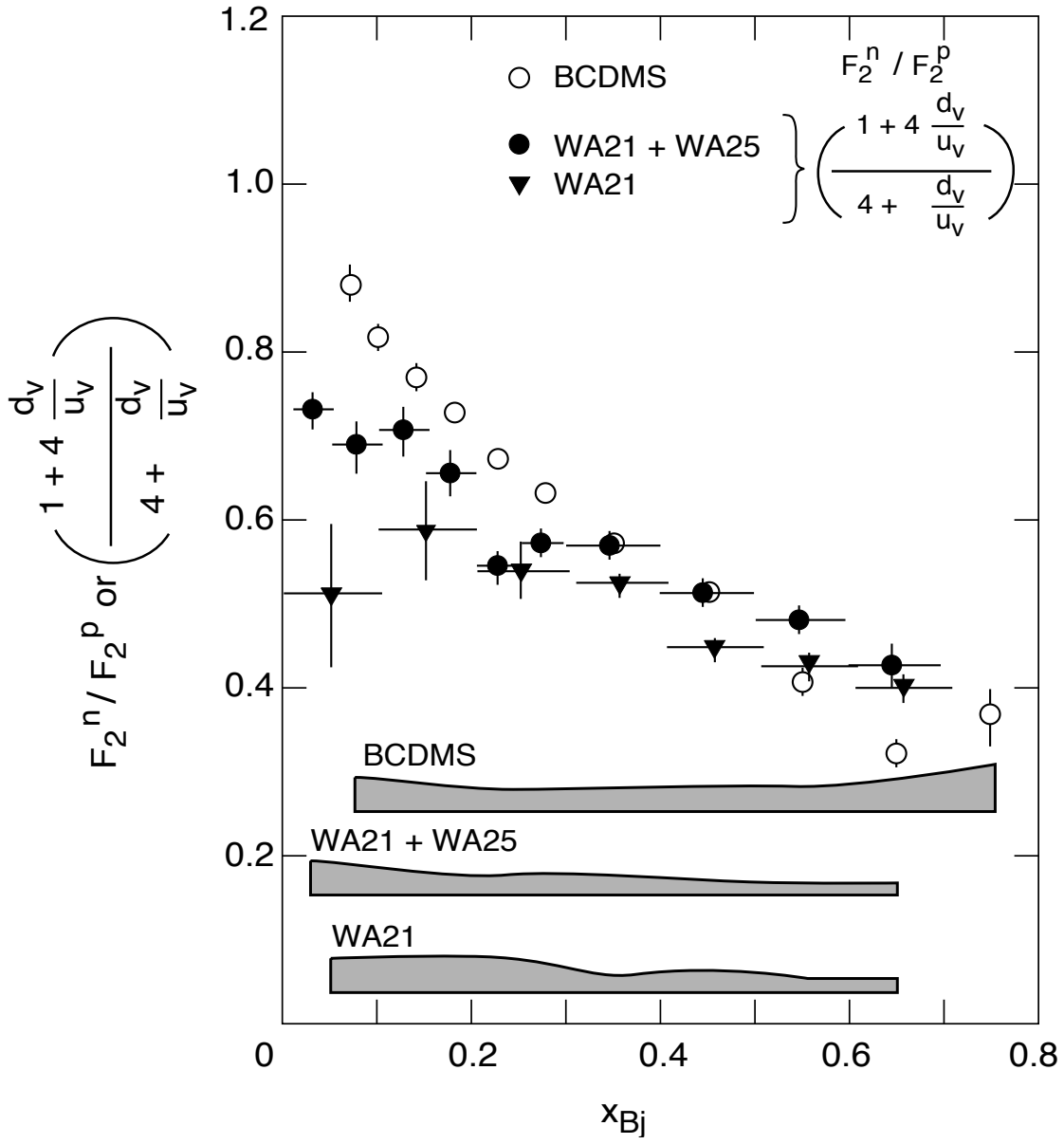

Figure 2.3:
The comparison of the ratio F_2^n/F_2^p for the muon (BCDMS) and the neutrino (WA21 and WA25) experiments.
(Systematic errors are shown in the shaded error bands)

From these structure functions and equations 2.22 and 2.23 various sum rules can be derived. The Adler sum rule[13] deals with the difference in the proton F_2 structure functions for neutrino and antineutrino scattering. In the quark-parton model this is the difference between the valence "up" and "down" quarks. The Adler sum rule is therefore given as:

$$\frac{1}{2}\int_0^1 \frac{d\,x_{Bj}}{x_{Bj}}\left(F_2^{\bar{\nu}p}\left(x_{Bj}\right) - F_2^{\nu p}\left(x_{Bj}\right)\right) = \int_0^1 d\,x_{Bj}\left(u_v\left(x_{Bj}\right) - d_v\left(x_{Bj}\right)\right). \tag{2.39}$$

Since the number of valence quarks in a proton is two "up" and one "down", this implies that the sum is unity, the difference in the number of "up" and "down" quarks. The Gross-Llewllyn-Smith sum rule[14] is defined using the sum of the proton F_3 structure functions for neutrino and antineutrino scattering. This leads to an integral over the sum of the valence "up" and "down" quark distributions:

$$\frac{1}{2}\int_0^1 d\,x_{Bj}\left(F_3^{\bar{\nu}p}\left(x_{Bj}\right) + F_3^{\nu p}\left(x_{Bj}\right)\right) = \int_0^1 d\,x_{Bj}\left(u_v\left(x_{Bj}\right) + d_v\left(x_{Bj}\right)\right). \tag{2.40}$$

From the same arguments given above one finds that this sum should be equal to three, the number of valence quarks in the nucleon.

The last sum rule we discuss is that of Gottfried[15], which is a measure of the flavor asymmetry of the quark sea. The Gottfried sum is derived from the difference of proton and neutron structure functions F_2 for muon scattering, thus is:

$$\int_0^1 \frac{d\,x_{Bj}}{x_{Bj}}\left(F_2^{\mu p}\left(x_{Bj}\right) - F_2^{\mu n}\left(x_{Bj}\right)\right) = \begin{array}{l} \frac{1}{3}\int_0^1 d\,x_{Bj}\left(u_v\left(x_{Bj}\right) - d_v\left(x_{Bj}\right)\right) \\ + \frac{2}{3}\int_0^1 d\,x_{Bj}\left(\bar{u}\left(x_{Bj}\right) - \bar{d}\left(x_{Bj}\right)\right). \end{array} \tag{2.41}$$

For a flavor symmetric sea, $\bar{u}(x_{Bj}) = \bar{d}(x_{Bj})$. Thus the second integral is zero. Since the first integral of the "up and "down" quarks is unity by the Adler sum rule, the Gottfried sum rule has a value of one third. In the balance of this thesis the Gottfried sum is discussed in some detail.

2.3. Quantum Chromodynamics

It is generally accepted that Quantum Chromodynamics (QCD) is the theory of the strong interaction. In this non-abelian gauge theory the strong interaction is described by the exchange of massless vector gluons. These gluons couple to the color charge of quarks. Since quarks appear in three different colors, one needs eight gluons (with different color combinations) to describe all possible interactions. Although QCD is based on the analogy with Quantum electrodynamics (QED) and gluons play the role of photons, in QCD, unlike QED, also gluons can couple to each other. This leads to the four leading order coupling diagrams[16] given in figure 2.4:

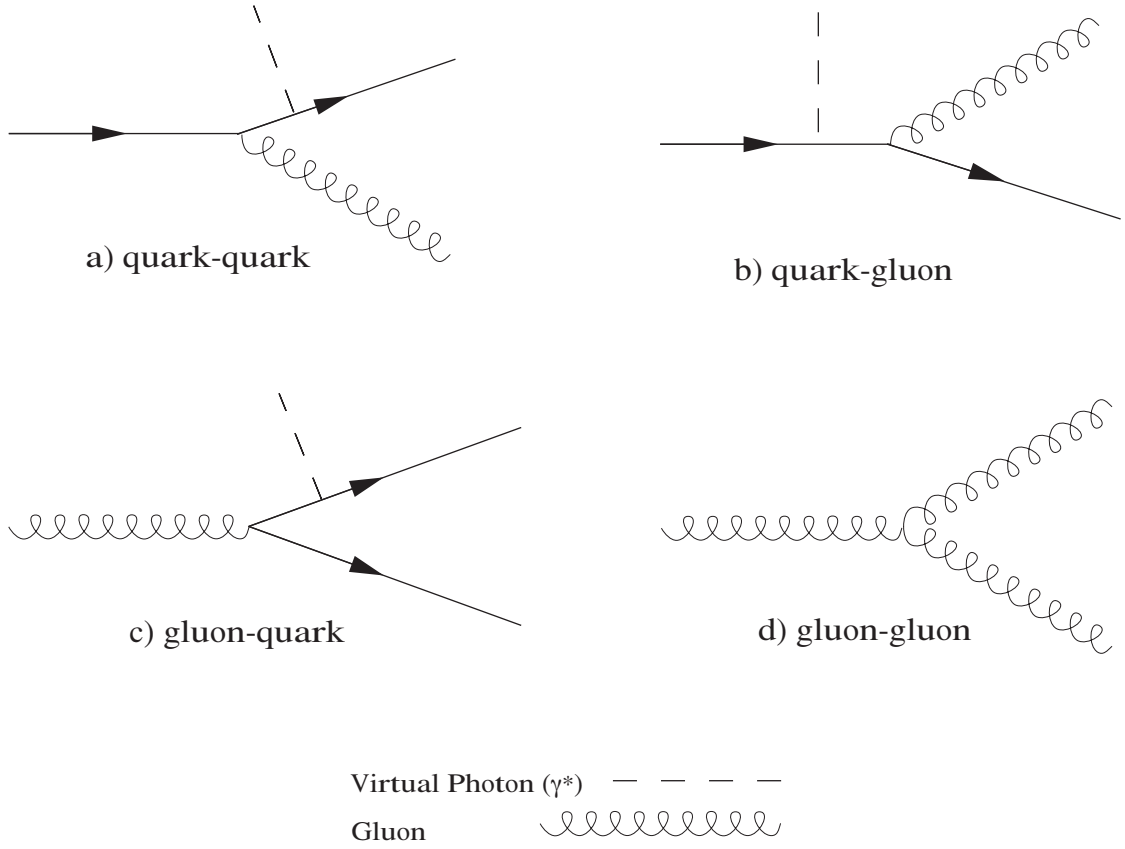

Figure 2.4:
The leading order QCD coupling diagrams.

The coupling at the quark-quark, quark-gluon, gluon-quark and gluon-gluon vertices, shown in figure 2.4, is given by the strong coupling constant α_s. Here α_s is used for the strong interaction vertices and is analogous to α from QED.

The value of α_s decreases for increasing Q^2, becoming small for short range interactions, which leads to "asymptotic freedom" at high Q^2. This is consistent with the assumption of quasi-free quarks made in the quark-parton model. In first order one can express the dependence or "running" of α_s with Q^2 by:

$$\alpha_s^0\left(Q^2\right) = \frac{4\pi}{\beta_0 \ln\left(Q^2/\Lambda^2\right)}, \tag{2.42}$$

that is, in first order a $\ln Q^2$ dependence. In next-to-leading, or second, order one has:

$$\alpha_s\left(Q^2\right) = \alpha_s^0\left(Q^2\right)\left[1 - \frac{\beta_1}{\beta_0{}^2}\frac{\ln\ln\left(Q^2/\Lambda^2\right)}{\ln\left(Q^2/\Lambda^2\right)}\right], \tag{2.43}$$

with $\beta_0 = 11 - \frac{2}{3}N_f, \beta_1 = 102 - \frac{38}{3}N_f$ and α_s^0 is the first order value of α_s. In these expressions the number of quark flavors N_f is taken to be four, as discussed above for the quark-parton model. Λ is a characteristic cutoff momentum, which must be determined experimentally. It defines the energy scale of the changes in α_s. It depends on the number of active quark flavors and on deeper physics. In various theories, the value of Λ depends also on which re-normalization scheme is used. We have taken the normally accepted $\overline{MS}$ (modified Minimal Subtraction)[17] scheme, in which $\Lambda \equiv \Lambda_{\overline{MS}}^{(4)}$, which typically has a value for Λ of about 200 MeV.

For sufficiently high values of Q^2 (typically above 1 GeV) the α_s has been reduced to a value at which the interaction is weak enough to use perturbation theory. This regime is called Perturbative QCD.

In leading order perturbative QCD the Q^2 dependence of the parton distributions and hence the F_2 structure functions) can be understood intuitively by using the diagrams

found in figure 2.4. In a) and b) a quark radiates a gluon, in c) a gluon turns into a quark-antiquark pair and in d) into a gluon pair. Since the distance probed by a virtual photon depends on Q^2 (the higher Q^2 the smaller the distance) one can now qualitatively understand the Q^2 dependence of the F_2 structure function by the following argument. For small values of Q^2 the probed quarks are "dressed" with gluons and quark-antiquark pairs (produced by the processes in figure 2.4). If one increases Q^2, and hence improves the resolution, the probed quark is "better distinguished" from its surrounding cloud, as seen in figure 2.5:

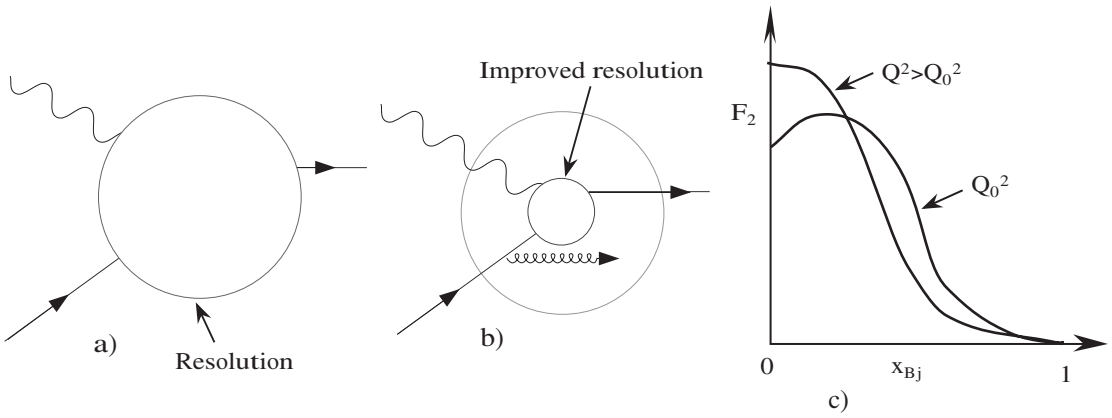

Figure 2.5:
The QCD "resolution" of the quark at (a) $Q^2 = Q_0{}^2$ and at (b) $Q^2 > Q_0{}^2$; and (c) the effect on the structure function F_2.

Because there is less interaction with the rest of the nucleon, the momentum fraction x (relative to the momentum of the nucleon) is therefore smaller than the momentum fraction at low Q^2. As is shown in section 2.2 one has x= x_{Bj}. Thus at high Q^2 the structure function peaks at a smaller value of x_{Bj}. (see figure 2.5)

This description was made quantitative by Altarelli and Parisi[18], among others. For this one has to introduce so-called splitting functions $P_{ij}\left(\frac{x}{z}\right)$ that are related to the

probability that the virtual photon is absorbed by parton (i) that has a fraction $\frac{x}{z}$ of the momentum of its parent parton (j). The four splitting functions reflect the four processes pictured in figure 2.4. Where P_{qq} is the quark-quark splitting function seen in part a) of figure 2.4, P_{qg} is the quark-gluon from part b), P_{gq} is the gluon-quark from part c) and the gluon-gluon splitting function P_{gg} is seen in part d) of figure 2.4. In leading order QCD one can start with a function of the quark and antiquark distributions with the form:

$$F = \sum_{i=1}^{N_f}\left[c_i q_i\left(x_{Bj},Q^2\right) + \overline{c}_i \overline{q}_i\left(x_{Bj},Q^2\right)\right], \tag{2.44}$$

decomposing the function F into flavor singlet and non-singlet parts $F = F^{NS} + F^{S}$, where the singlet and non-singlet terms are given by the formulae:

$$F^{S} = \langle c\rangle \sum_{i=1}^{N_f}\left[q_i\left(x_{Bj},Q^2\right) + \overline{q}_i\left(x_{Bj},Q^2\right)\right], \tag{2.45}$$

$$F^{NS} = \sum_{i=1}^{N_f}\left[\left(c_i - \langle c\rangle\right) q_i\left(x_{Bj},Q^2\right) + \left(\overline{c}_i - \langle c\rangle\right) \overline{q}_i\left(x_{Bj},Q^2\right)\right]. \tag{2.46}$$

The non-singlet term F^{NS} depends only on the quark distributions and implies that:

$$\sum_{i=1}^{N_f}\left[c_i - \langle c\rangle + \overline{c}_i - \langle c\rangle\right] = 0, \tag{2.47}$$

$$\langle c\rangle = \frac{1}{2N_f}\sum_{i=1}^{N_f}\left(c_i + \overline{c}_i\right). \tag{2.48}$$

The singlet term F^S is determined by both quark and gluon distributions. While the evolution in Q^2 of the non-singlet term can be given simply as:

$$\frac{d\ F^{NS}\left(x,Q^2\right)}{d\ \ln Q^2} = \frac{\alpha_s\left(Q^2\right)}{2\pi}\int_x^1 \frac{dz}{z} F^{NS}\left(z,Q^2\right) P_{qq}\left(\frac{x}{z}\right), \tag{2.49}$$

one can write the fundamental Altarelli-Parisi equation for the non-singlet term as follows:

$$\frac{d\ F^{NS}\left(x,Q^2\right)}{d\ \ln Q^2} \equiv \frac{\alpha_s\left(Q^2\right)}{2\pi} P_{qq} \otimes F^{NS}\left(x,Q^2\right). \tag{2.50}$$

For the singlet distributions the two equations are given schematically as:

$$\frac{d}{d\ \ln Q^2}\begin{bmatrix} F^S\left(x,Q^2\right) \\ g\left(x,Q^2\right) \end{bmatrix} = \frac{\alpha_s\left(Q^2\right)}{2\pi}\begin{bmatrix} P_{qq} & 2N_f P_{qg} \\ P_{gq} & P_{gg} \end{bmatrix} \otimes \begin{bmatrix} F^S\left(x,Q^2\right) \\ g\left(x,Q^2\right) \end{bmatrix}. \tag{2.51}$$

One can apply these evolution equations to the structure function F_2 by taking equation 2.44, making the assumption that $c_i = \bar{c}_i = e_i^2$ and writing F_2 in a similar form as equation 2.24:

$$F_2\left(x_{Bj},Q^2\right) = x_{Bj}\sum_{i=1}^{N_f} e_i^2\left[q_i\left(x_{Bj},Q^2\right) + \bar{q}_i\left(x_{Bj},Q^2\right)\right]. \tag{2.52}$$

The Q^2 evolution equations are used to describe the F_2 structure function data obtained experimentally. The Altarelli-Parisi equations only determine the Q^2 dependence not the x_{Bj} dependence of F_2. Once the x_{Bj} dependence at a fixed value of Q^2 (Q_0^2) is given, the theory predicts the x_{Bj} dependence at all other values of Q^2. By this procedure, having sufficiently accurate data, one can extract the value of the strong

coupling constant α_s (preferably through the non-singlet part) and the quark and gluon distributions of the nucleon from the singlet equations.

So far we have neglected the mass of the nucleon. At low Q^2, however, the nucleon mass must be corrected for. This is effectively done by replacing x_{Bj}, the momentum fraction of the nucleon carried by the struck quark, by the Nachtmann scaling variable[19] ξ given by:

$$\xi = \frac{2\,x_{Bj}}{1+\sqrt{1+4\,M^2\,x_{Bj}{}^2/Q^2}}. \tag{2.53}$$

This procedure[20] is called the target mass correction.

Finally, higher order (higher twist) corrections must be accounted for. This is commonly done by parametrizing the structure function as follows:

$$F_2\left(x_{Bj},Q^2\right) = F_2^{LT}\left(x_{Bj},Q^2\right)\left[1+\frac{C\left(x_{Bj}\right)}{Q^2}+\quad\right]. \tag{2.54}$$

These effects are due to interactions of the struck quark with the spectator quarks. The leading twist F_2^{LT} (i.e. without these quark-quark interactions) already include the target mass correction. Higher twist effects cannot be calculated explicitly and are usually determined by experiment.

2.4. Radiative corrections

The structure function F_2 is derived in terms of a pure one photon exchange cross section $\sigma_{1\gamma}$; however, the measured deep inelastic cross section contains other, higher order, electroweak processes. These higher order effects are customarily taken into account by making a theoretical correction to the experimentally observed cross section.

In this way the measured cross section, including radiative corrections, is converted into a single photon cross section.

The Feynman diagrams of the most important of the higher order radiative processes are shown in figure 2.6. The dominant process is internal bremsstrahlung, where a real photon is radiated by either the incoming or the scattered muon, shown in a) and b) of figure 2.6, respectively. This is called a radiative event. The process in which a virtual photon is emitted by the incoming and re-absorbed by the outgoing muon, or visa-versa, shown in figure 2.6 c) and is called a radiatively degraded vertex. In part d) of figure 2.6 the process of vacuum polarization of the virtual photon is shown. Here the loop may contain either charged lepton-antilepton (e^+e^-, $\mu^+\mu^-$ or $\tau^+\tau^-$) pairs or quark-antiquark pairs. Finally, instead of a virtual photon, a virtual Z^0 may be exchanged. However this diagram is suppressed due to the large Z^0 mass and is about a 1% effect at the energies considered by this experiment.

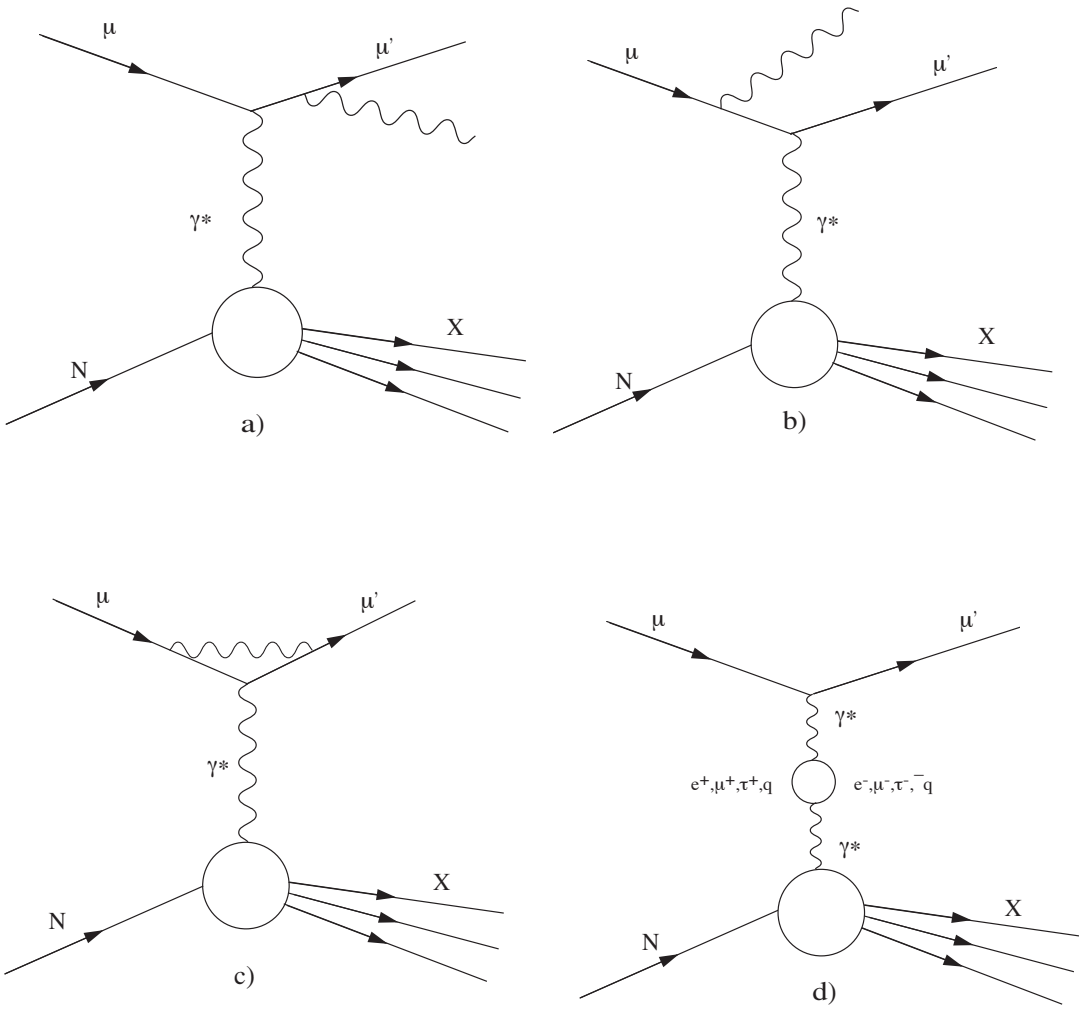

Figure 2.6:
The higher order radiative processes. Internal bremsstrahlung (a) and (b), a radiatively degraded vertex (c) and vacuum polarization (d).

These corrections to the total cross section are combined, and called for obvious reasons, radiative corrections. A radiative correction factor is applied as a weight for each measured event. This weighting factor is calculated as a function of the scaling variables x_{Bj} and y and is applied in the form:

$$\eta\left(x_{Bj},y\right)=\frac{\sigma_{1\gamma}\left(x_{Bj},y\right)}{\sigma_{measured}\left(x_{Bj},y\right)}, \tag{2.55}$$

where the contribution of higher order processes to $\sigma_{1\gamma}$ are given as a sum over their individual contributions δ_i by:

$$\sigma_{measured}\left(x_{Bj},y\right)=\sigma_{1\gamma}\left(x_{Bj},y\right)\left[1+\sum_i \delta_i\left(x_{Bj},y\right)\right]. \tag{2.56}$$

The radiative corrections used in this thesis were calculated by the method of Akhundov, Bardin and Shumeiko[21] using, as input, the most recent descriptions of available data.

References: Chapter 2

1 F. Halzen and A. D. Martin, *Quarks and Leptons*, J. Wiley & sons, New York (1984);
F. E. Close, *An Introduction to Quarks and Partons*, Academic Press, London (1979).

2 D. H. Perkins, *Introduction to High Energy Physics*, Addison-Wesley, Menlo Park (1987).

3 J. P. Bjorken, *Phys. Rev.* **179** (1969) 1547.

4 C. G. Callen and D. G. Gross, *Phys. Rev. Lett.* **22** (1969) 156.

5 SLAC-MIT, E. D. Bloom *et al.*, *Phys. Rev. Lett.* **23** (1969) 930;
SLAC-MIT, M. Briedenbach *et al.*, *Phys. Rev. Lett.* **23** (1969) 935.

6 M. Gell-Mann, *Phys. Lett.* **8** (1964) 214;
G. Zweig, CERN Reports 8182/TH 401, 8419/TH 412 (1964).

7 J. D. Bjorken and E. A. Paschos, *Phys. Rev.* **185** (1969) 1975;
J. D. Bjorken and E. A. Paschos, P*hys. Rev. D* **1** (1970) 3151;
J. Kuti and V. F. Weiskopf, *Phys. Rev. D* **4** (1971) 3418
R. P. Feynman, *Photon-hadron interactions*, Benjamin, New York (1972).

8 NMC, P. Amaudruz *et al.*, *Z. Physik* **C51** (1984) 387.

9 Compilation of cross sections IV, CERN Report, CERN-HERA 87-01.

10 D. O. Caldwell *et al.*, *Phys. Rev. D* **7** (1973) 1362.

11 BCDMS, A. C. Benvenuti *et al.*, *Phys. Lett.* **B223** (1989) 485;
BCDMS, A. C. Benvenuti *et al.*, *Phys. Lett.* **B237** (1990) 592.

12 G.T. Jones *et al.*, Oxford Univ. rep. OUNP-89-18 (1989);
G.T. Jones *et al.*, "Preliminary Results on the Ratio d/u(x).." paper submitted to the 1989 Int. Symp. on Lepton and Photon Interactions at High Energies, Stanford Univ. (1989).

13 S. L. Adler, *Phys. Rev.* **143** (1966) 1144.

14 D. J. Gross, C. H. Llewellyn-Smith, *Nucl. Phys.* **B14** (1969) 337.

15 K. Gottfried, Phys. *Rev. Lett.* **18** (1969) 1174.

16 G. Altarelli, "Partons in Quantum Chromodynamics.", *Phys. Rep.* **81C** (1982) 1.

17 W. A. Bardeen *et al.*, *Phys. Rev. D* **18** (1978) 3998.

18 G. Altarelli and G. Parisi, *Nucl. Phys.* **B126** (1977) 298.

19 O. Nachtmann, *Nucl. Phys.* **B63** (1973) 237.

20 H. Georgi, H. D. Politzer, *Phys. Rev. D* **14** (1976) 1829.

21 A. A. Akhundov *et al.*, *Sov. J. Nucl. Phys.* **26** (1977) 660; **44** (1986) 988;
JINR-Dubna preprints E2-10147 (1976), E2-10205 (1976), E2-86-104 (1986);
D. Bardin and N. Schumeiko, *Sov. J. Nucl. Phys.* **29** (1979) 499.

3. Experimental set up

The experiment described in this thesis measures the cross section for Deep Inelastic Scattering of high energy muons from neutrons and protons. The nucleon target is at rest in the Laboratory frame of reference, (what is known as a fixed target experiment). All the momentum is carried by the beam muons. The kinematics of muon-nucleon scattering, which are spherically symmetric in the Center of Momentum frame of reference, are Lorentz-transformed to the Lab-frame. This forces the geometry of the detector to be a cone with the axis along the incoming beam's original path, and the small opening angle in the direction of the incident muon. The coordinate system used by the experiment is a right handed Cartesian coordinate system with the positive **x**-axis pointing along the direction of the incoming beam, pointing downstream. The **y**-axis is chosen to be the horizontal axis, with positive **y** pointing to the left, when facing downstream. The **z**-axis is the vertical axis with positive **z** pointing up. This is shown in figure 3.1. The **y**-axis is also labeled “Jura” and “Saleve”, the two mountains near the laboratory that form visible landmarks, at least on a clear day.

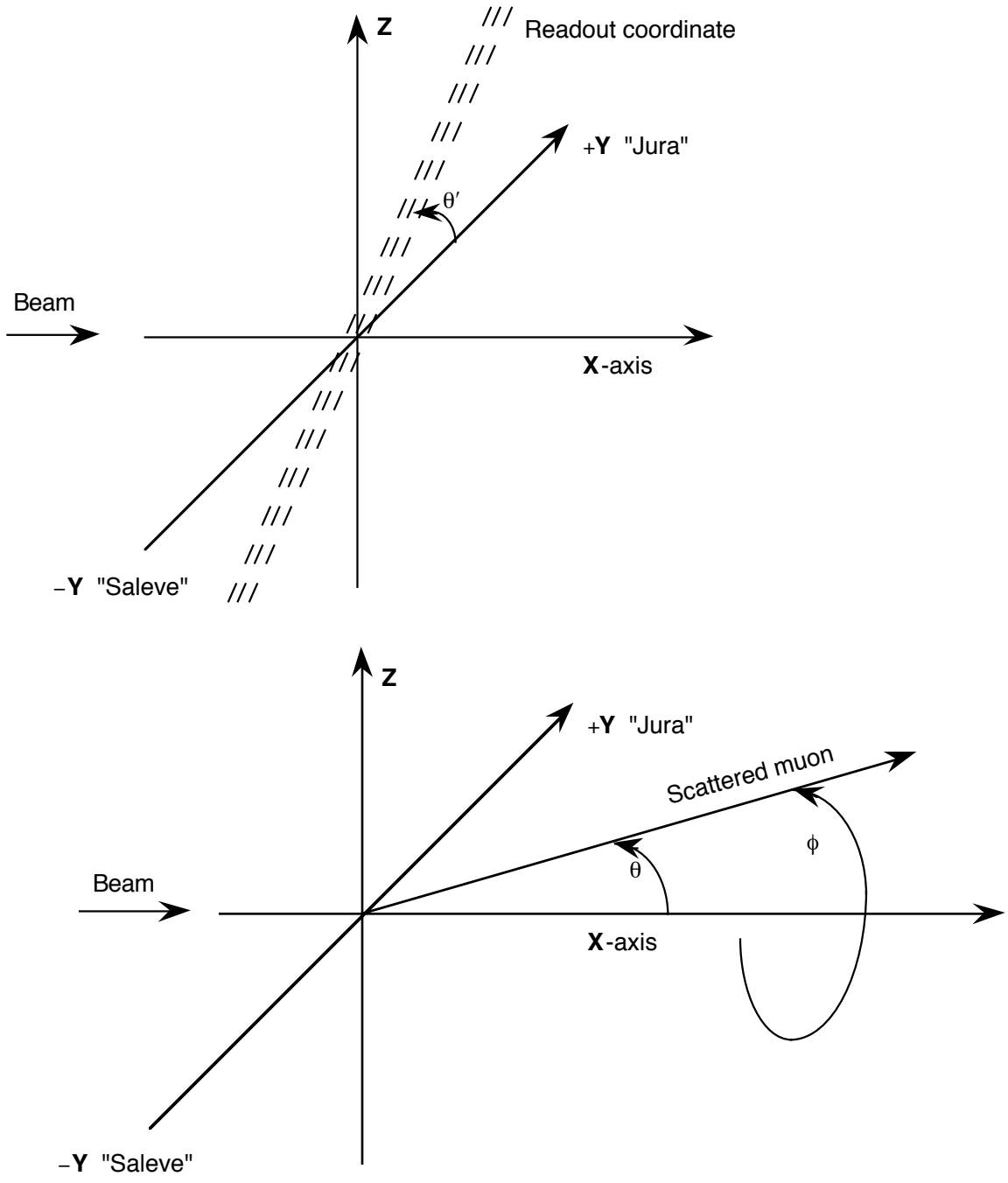

Figure 3.1:
The NMC coordinate system.

The general philosophy is to measure the incoming beam muon momentum and trajectory, collide the muon beam with the fixed target, and measure the trajectory and momentum of the scattered muon. The momentum of the incoming muons in the muon beam is measured by the Beam Momentum Station (BMS). See figure 3.2. The momentum of the scattered muon is measured with the Forward Spectrometer Magnet (FSM).

Muons undergo only electromagnetic and weak nuclear interactions. At the energies used in these experiments, the interaction of the muons with the air in the laboratory is negligible. Therefore an open spectrometer configuration was used. This is shown in the schematic and isometric views of the NMC spectrometer, shown in figure 3.2:

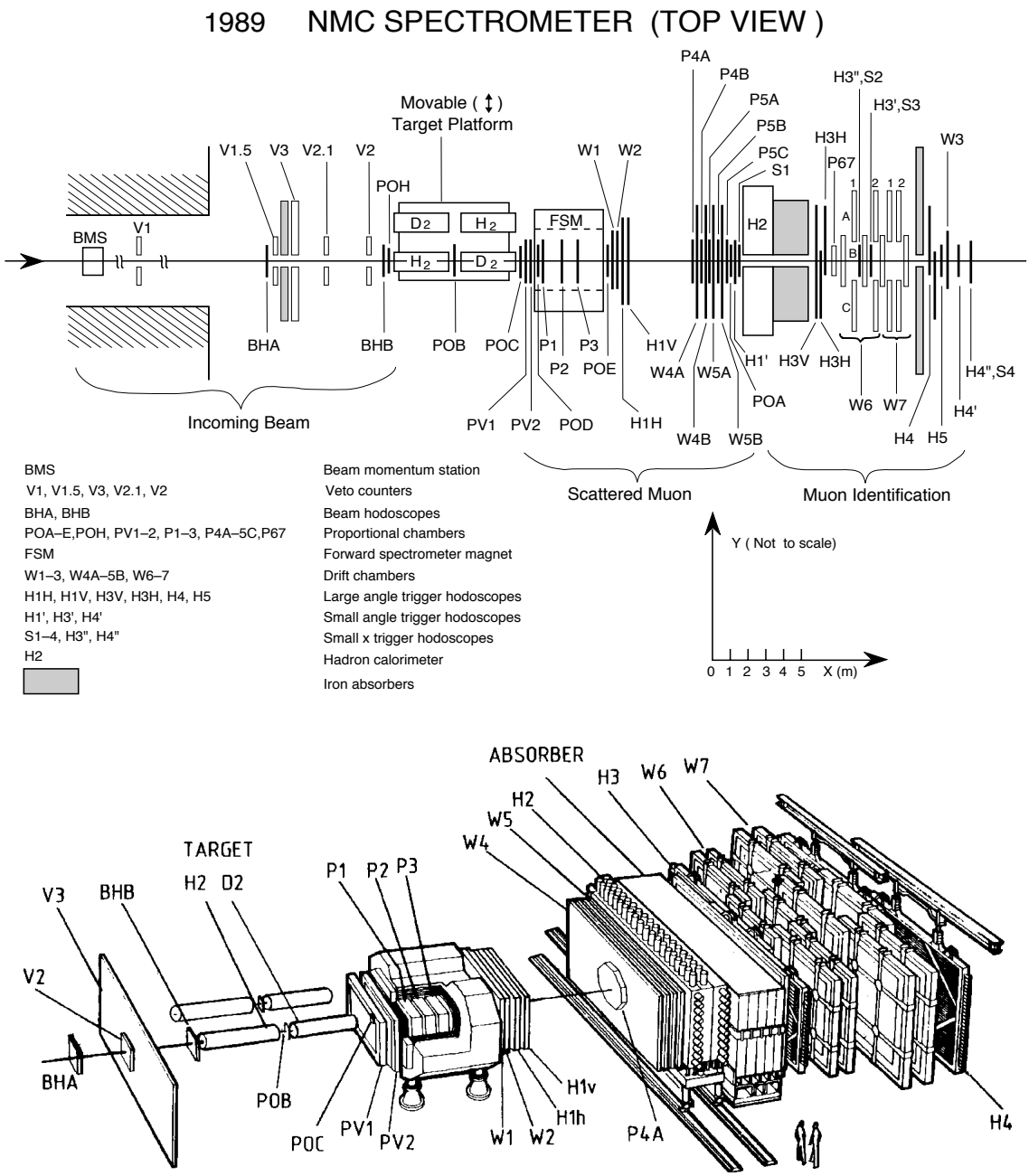

Figure 3.2:

The NMC Spectrometer.

(In the isometric view, figures are shown to provide scale.)

3.1. The Muon Beam

The experiment was conducted at CERN using the M2 muon beam line of the Super Proton Synchrotron (SPS) accelerator. The SPS is a 400 GeV accelerator. The muons are produced for the experiment in a 3 step process: (a) the acceleration of protons by the SPS; (b) the production of hadrons by collisions of energetic protons with a stationary target and (c) the decay of the hadrons into muons. (For example $\pi^+ \rightarrow \mu^+ + \nu_\mu$.)

3.1.1. SPS

The SPS accelerator at CERN provides a beam of protons with an energy of 400 GeV. This beam is extracted from the SPS and collided onto a Tungsten target (T6). The collisions produce hadrons, primarily pions and kaons. The hadron beam is momentum selected, with a spread of momentum, $\Delta\mathbf{p}/\mathbf{p}$, of 10 percent. The momentum selected hadrons are focused into the 600 meter long decay channel. The length of 600 meters allows about 4 percent of the hadrons to decay into muons. The remaining hadrons are then removed from the beam by a Beryllium target, leaving a hadron contamination of the beam of $\leq 10^{-5}$. The muons in the beam, which have a nuclear cross section of approximately zero pass through the Beryllium. The beam halo, (stray muons with a trajectory parallel to the beam) is about 7 percent of the momentum selected muon beam. The beam of muons, after being measured by the BMS, is the source of incident muons for the experiment. The incident muons have a final momentum spread of about 5 percent. A diagram of the SPS is shown in figure 3.3 and a schematic of the BMS is shown in figure 3.4.

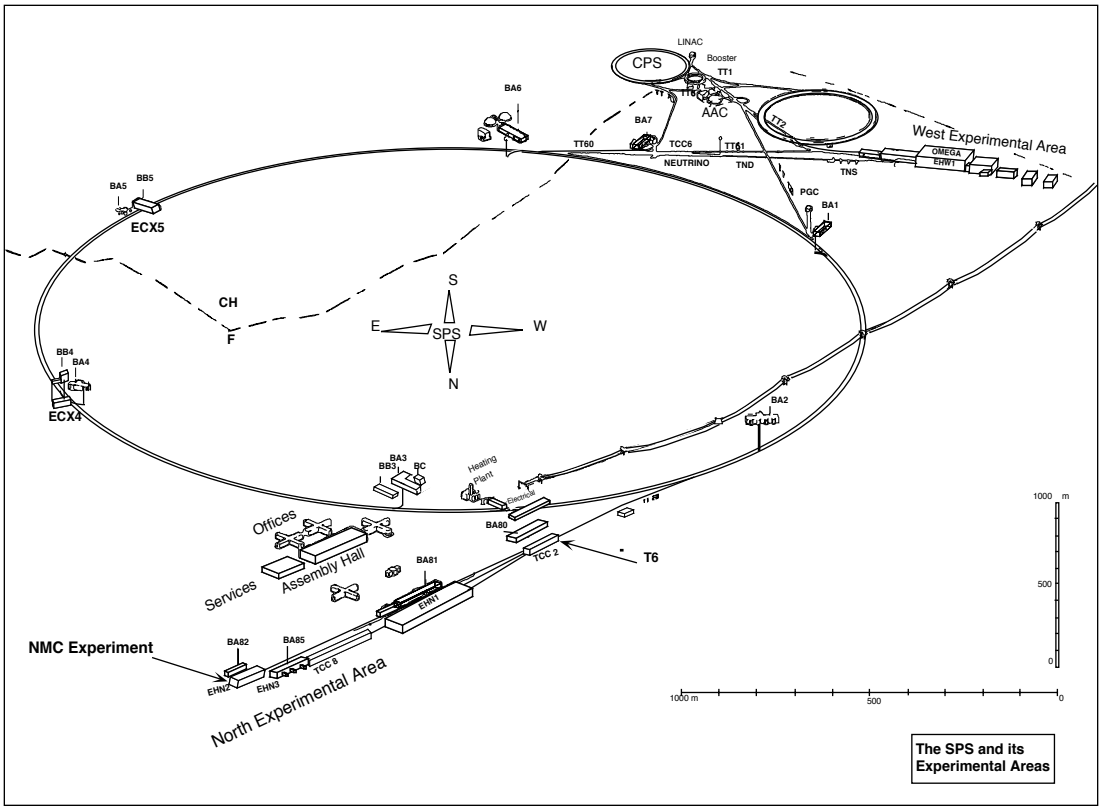

Figure 3.3:
The SPS accelerator at CERN.

3.1.2. Beam Momentum Station

The momenta of the incoming muons are measured by the BMS. The BMS consists of four sets of scintillating hodoscope planes and a bending magnet. Two sets of hodoscope planes are placed before the magnet and two after the magnet. The momentum can be calculated from the change in the beam's trajectory caused by the passage of the positively charged muons through the known magnetic field of the BMS. This is shown schematically in figure 3.4. The relative timing between the BMS and the experiment's trigger time is obtained by Time to Digital Converters (TDCs) connected to the scintillating hodoscopes. This associates the incoming beam muon with the scattered

muon and helps eliminate accidental tracks, caused by the beam halo or other background sources in the experiment, from the analysis. To improve the measurement of the beam momentum the BMS is calibrated by the Beam Calibration Station (BCS) as described below.

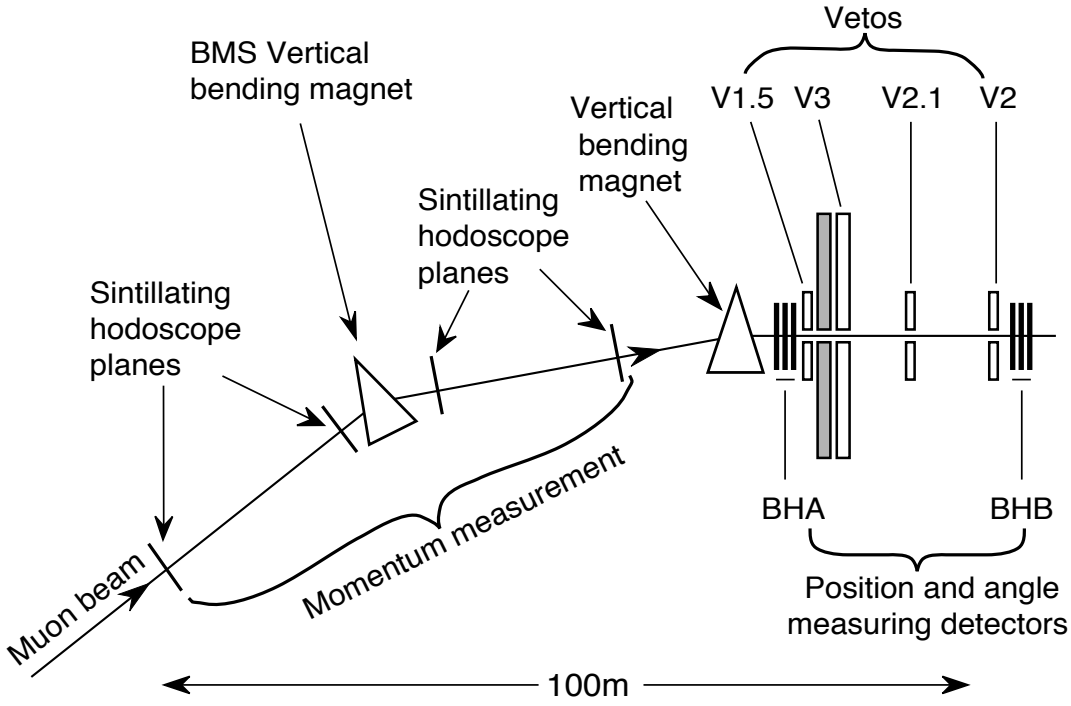

Figure 3.4:
A schematic representation of the Beam Momentum Station (BMS).

Special calibration data is taken with the FSM magnet turned off, using a second well calibrated bending magnet, located at the end of the main spectrometer (not seen in figure 3.2). There are sets of proportional chambers positioned in such a way as to give a long lever arm (36 meters) in the second magnet. This reduces error in the momentum calculation. Using this scheme, the momentum resolution for the muon beam is 0.2% at a nominal beam energy of 280 GeV.

3.1.3. Beam Hodoscopes and Proportional Chambers

The chambers that are used to determine the trajectory of the incoming beam muon's track are a combination of scintillating hodoscopes and proportional mode wire chambers. The hodoscopes consist of two groups of four readout planes each group spaced about 7 meters apart. Both hodoscopes are located upstream of the target (See figures 3.2 and 3.4). Beam Hodoscope A (BHA) is located upstream of Beam Hodoscope B (BHB). Each readout plane of BHA and BHB is made up of two sets of 4 mm wide scintillating hodoscope strips, staggered by 2 mm, hence giving a resolution of 1.2 millimeters. One proportional chamber consisting of four planes is located just downstream of BHB. This chamber, called P0H, aids in the beam track reconstruction and has a resolution of 0.6 millimeters. P0B, with eight planes of proportional chambers, is located between the two targets. (See figures 3.2 and 3.5) This chamber is used to help determine the trajectory of the incoming beam muon for those events that have a vertex in the downstream target. P0B is also used for the determination of the trajectory of the scattered muon, for those events in the upstream target. The type of readout planes, the number of elements, spacing, resolution and **x**-positions for these beam trajectory detectors are given in table 3.1 and in figure 3.2:

Table 3.1: Beam Chambers

Name	Plane Type	1/2-Width (mm)	1/2-Height (mm)	Resolution (mm)	**x**-position (m)
BHA	$+\theta,-\theta,Z,Y$	40	40	1.15	−17.0
BHB	$Y,Z,+\theta,-\theta$	40	40	1.15	−11.3
P0H	2Y, 2Z	80	80	0.58	−10.9
P0B	$2+\theta,2-\theta,2Y,2Z$	80	80	0.58	−6.6

3.2. Target

The targets that were used for the period P3A89 were liquid hydrogen, H_2 and liquid deuterium, D_2. The targets were arranged in two sets, having deuterium upstream and hydrogen downstream Target setup-1 and Target setup-2 having the reverse order, i.e., hydrogen upstream and deuterium downstream. The target sets were alternately positioned in the muon beam. In figure 3.5 the target arrangement is shown, including detector P0B located between the two targets. (Also seen in figure 3.2) An over-pressure of 100 mbar was applied to insure that the targets remained a liquid. The liquid hydrogen was pure H_2, but there was a small contamination of hydrogen-deuterium in the liquid deuterium (D_2). Thus 3.01 percent[1] of the D_2 was really HD. The description of the targets, using calculations of length and temperature from appendix 8.1, is given in table 3.2:

Table 3.2: Target Description

Target Material	Length (mm)	Radius (mm)	Mass (kg)	Temperature (K)
Hydrogen	2989±1	50.0	1.6547	20.52
Deuterium	2989±1	50.0	3.7916	23.84

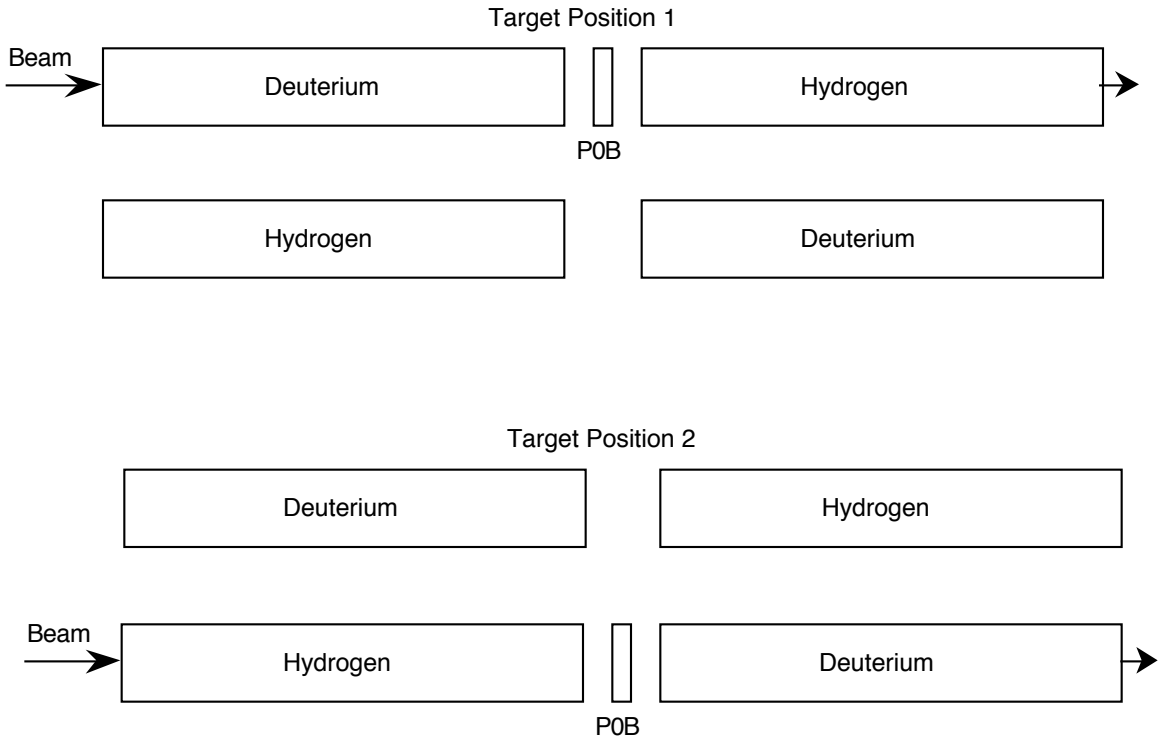

Figure 3.5
The alternating Target setup.

3.3. Forward Spectrometer Magnet

The momenta of the scattered muon was derived by the measured bending of their trajectories in the magnetic field of the FSM. The FSM is a large air-gap dipole magnet with a length of 4.3 m along the **x**-axis and an aperture of 2 m horizontally (along the **y**-axis) by 1 m vertically (along the **z**-axis). For operation with a nominal beam energy of 280 GeV a current of 5000 A was used, giving a magnetic field in the **z** direction with a field integral, $\int \mathbf{B} \cdot \mathbf{dl} = 5.182\ \mathrm{T} \cdot \mathrm{m}$. The magnetic field was mapped as a function of **x, y** and **z** to better then 0.2 percent[2] and in addition was calibrated by using the measurements of the masses of the J/ψ and K^0 mesons. The stability of the field was

monitored with a Hall probe and a NMR device. The nominal center of the NMC coordinate system is located near the center of the FSM. The **x** and **z** coordinate axes are centered in the magnet, while the **y** coordinate is shifted by 6 cm horizontally in the negative or "Saleve" direction.

The acceptance of scattered muons at the magnet aperture extends up to scattering angles of 140 mrad in the bending plane (**x**-**y**) and 85 mrad in the vertical (**y**-**z**) plane. A bending angle of 140 mrad, with the known $\oint \mathbf{B} \cdot \mathbf{dl}$, corresponds to a minimum momentum of 24 GeV/c.

3.3.1. Magnet Chambers

Inside the FSM there are two sets of proportional chambers; P1, P2, P3 (P123) and P0D. These chambers improve the measurement of the bending angle of the muon, due to the magnet, and help determine the initial trajectory of the scattered muon. The large proportional chambers; P1, P2 and P3, cover the full width and height of the FSM air gap. Each has a dead central region of 6.5 cm radius. The P1 is located close to the front opening of the FSM, whereas P2 and P3 are at **x**-positions of –0.3 and +0.3 meters with respect to the FSM's center. The small proportional chamber P0D covers the insensitive 6.5 cm radius central region of P123. (See Table 3.3, along with figure 3.2, for a better description.)

Table 3.3: Magnet Chambers					
Name	Plane Type	1/2-Width (mm)	1/2-Height (mm)	Resolution (mm)	**x**-position (m)
P1	$Z,Y,+\theta$	912	400	1.15	−1.6
P2	$-\theta,Y,Z$	912	400	1.15	−0.3
P3	$-\theta,Y,Z$	912	400	1.15	0.3
P0D	$2Z,-\theta,2Y,+\theta,2Z$	80	80	0.58	−1.9

3.4. Muon Chambers

The initial trajectory of the scattered muon and the final trajectory after the bending by the FSM are determined by two sets of chambers. The initial trajectory is determined by the large proportional chambers PV1 and PV2, located just in front of the entrance of the FSM. PV2 has a dead central area of 6.5 cm radius and PV1 is also insensitive in the center due to space-charge effects. The small proportional chamber P0C, located in front of PV1, covers the insensitive regions of PV1 and PV2. It should be noted that for events found in the upstream target, the small proportional chamber P0B is also used to improve the determination of the trajectory. In Table 3.4 the chamber's characteristics are given.

The final trajectory of the scattered muon (after the FSM) is determined by two sets of multi-wire Drift Chambers; W12 and W45. The two W12 drift chambers, W1 and W2, consist of 8 readout planes each and are located just behind the exit of the FSM. The W12 drift chambers cover an area 2.2 m wide and 1.2 m high with a dead area at the center 6 cm in radius. The small proportional chamber P0E, located in front of W1, covers the insensitive central region. (See Table 3.4, along with figure 3.2, for a better

description.) The W45 drift chambers are made up of four modules of 4 planes each and located downstream of W12. Each plane is 5.0 m wide and 2.5 meters high and has a dead region of 13×14 cm^2. The five modules of the proportional chamber P45 are placed between the W45 modules. P45 covers the deadened region of W45 and provides redundancy in the higher rate central region. (See Table 3.4 for a better description.) It should be noted that the small proportional chamber P0A is used in conjunction with P0E to measure J/ψ events for the calibration of the FSM.

Table 3.4: Muon Chambers

Name	Plane Type	1/2-Width (mm)	1/2-Height (mm)	Resolution (mm)	**x**-Position (m)
P0B	$2+\theta, 2-\theta, 2Y, 2Z$	80	80	0.58	−6.6
PV1	$+\theta', Y, -\theta', Y$	752	470	1.15	−2.5
PV2	$Y, +\theta, +\theta', -\theta, -\theta', Y$	768	500	1.15	−2.2
P0C	$2-\theta, 2Y, 2Z, 2+\theta$	80	80	0.58	−2.8
P0E	$2-\theta, 2Y, 2Z, 2+\theta$	80	80	0.58	2.3
W1	$-\theta, Y, Z, +\theta$; $Z, -\theta, Y, +\theta$	1120	620	0.25-0.30	2.6
W2	$Z, -\theta, Y, +\theta$; $-\theta, Y, +\theta, Z$	1120	620	0.25-0.30	2.9
W4A,B	$2Y, 2Z$; $2\theta, 2Y$	2620	1300	0.35	6.9-7.4
W5A,B	$2Z, 2\theta$; $2Y, 2Z$	2620	1300	0.35	7.6-8.0
P45	$Y, -\theta; Y, \theta; Y, -\theta; Y, \theta; Y, \theta$	452.5	452.5	1.15	6.8-8.1
P0A	$2-\theta, 2Y, 2Z, 2+\theta$	80	80	0.58	8.3

3.5. Muon Identification chambers

The muon identification determines which of the particles that are seen by the detector is the scattered muon. This is done by filtering out all the electrons, photons and hadrons with the hadron calorimeter and then, by process of elimination, one assumes

that the remaining tracks must be muons. These remaining tracks are seen by the muon identification chambers. A muon is identified by its passage through a calorimeter and a 2 meter thick passive iron absorber.

3.5.1. Hadron Calorimeter (H2) and Absorber

The H2 calorimeter is used to identify electrons, muons and hadrons and to measure the energy of electromagnetic showers. H2 consists of a left hand and right hand half. Each half is made up of three modules. There is a 10 cm radius beam hole in the center of the H2 calorimeter.

In the calorimeter, the first module is the electromagnetic shower detector, made of alternating lead plates and scintillator blades. This material corresponds to 22 radiation lengths for e^+, e^- and γ. This is enough to deposit essentially all of these particles in this region. The electromagnetic shower detectors represent only 0.95 nuclear interaction lengths for hadrons. The next two modules are made of iron plates and scintillator chambers. The Iron provides a further 5.5 nuclear interaction lengths.

Located just down stream of the H2 calorimeter is a 2 m thick passive steel hadron absorber, which provides an additional 10 interaction lengths of material. Thus the hadrons are stopped by a total of 16.5 nuclear interaction lengths of material. The hadron absorber can be magnetized. It was not magnetized for the NMC experiment but still had a residual field[3] that deflected charged particles vertically. The absorber also has a 20×20 cm^2 beam hole.

3.5.2. Muon Chambers

The muon trajectory after the hadron filter is measured by the W67 drift chambers. These cover an area of 10×4.4 m^2 and are located behind the hadron absorber. The W67 chambers consist of three sets; named A, B and C. Each of the sets are made up of 4 modules. The two sets, A and C, each has 11 readout planes and they cover the region furthest from the beam. The B set covers the central region with 16 planes and has a deadened area of 18 cm high and 24 cm wide.

The proportional chamber P67 and the drift chamber W3 cover the central deadened area and are used to identify muons close to the beam and to provide a Small Angle Interaction Trigger (SAIT) and a Small-x_{Bj} trigger (SX). The P67 chamber is located between the hadron absorber and the front of the upstream W67B module. The drift chamber W3 is located behind a 1/2 m thick Iron wall downstream of the last W67B module. (See table 3.5, plus figure 3.2, for a more detailed description.)

Table 3.5: Muon Identification Chambers

Name	Plane Type	1/2-Width (mm)	1/2-Height (mm)	Resolution (mm)	**x**-Position (m)
W6A	$Z,Y,\theta;\ Z,Y,\theta$	1450	1754	0.35	14.2-15.2
W7A	$Z,Y;\ Z,Y,\theta$	1755	2185	0.35	16.3-16.8
W6B	$Z,Y,\theta,Z,Y;\ Z,Y,\theta$	1450	1755	0.35	13.6-14.7
W7B	$Z,Y,\theta;\ Z,Y,\theta,Z,Y$	1755	2185	0.35	15.9-17.2
W6C	$Z,Y,\theta;\ Z,Y,\theta$	1450	1755	0.35	14.2-15.2
W7C	$Z,Y;\ Z,Y,\theta$	1755	2185	0.35	16.3-16.8
P67	$Y,+\theta;\ Y,+\theta'$	452.5	452.5	1.15	13.2
W3	$Z,-\theta,Y,+\theta;\ -\theta,Y,+\theta,Z$	1120	620	0.25-0.30	19.3

On the whole the W67 drift chambers gave good and stable results, the design of a graded cathode field gave them the most uniform drift, cell even with the large (6 cm) cell size. W67 drift chambers were severely aged, since they dated back to the beginning of the previous experiment (the EMC), but by the beginning of the final year of data taking of the NMC experiment W67 was showing signs of aging. The last two collaboration members in charge of W67, Ioannis Tzamouranis and the author of this thesis, started working on the chambers at the beginning of this final 1989 run. They succeeded in bringing the condition of W67 into excellent running condition for the 1989 run. This involved replacing broken preamplifiers, curing ground loop problems and repairing broken low-voltage circuitry. Also involved were maintaining the normal operating gas flow and high-voltage conditions. However, the dark current problems and the broken or problematic wires were beyond repair. In addition these chambers had lower efficiency within 20 cm of the beam. While this region had backup detectors in NMC, the W67 drift chambers were replaced for the next generation of the experiment (the Spin Muon Collaboration) by an array of Limited Streamer mode tubes[4], called ST67, by groups from Houston, Northeastern and Munich universities.

3.6. Triggers

In an experimental environment with high event counting rates fast on-line data filtering and preprocessing must be done to decide which events are to be recorded (i.e., to separate deep inelastic scattering events from the background of beam halo muons and other sources). This fast event selection is done by processing the signals from scintillator hodoscopes with fast electronics to form a trigger.

To remove events initiated by the beam halo background, some of the scintillating hodoscopes are used to form veto counters. A description and the positions of the Veto counters are given in table 3.6 and shown in figure 3.2:

Table 3.6: Veto Counters

Name	1/2-Width (mm)	1/2-Height (mm)	**x**-Position (m)	Notes:
V1.5	700	700	-16.0	Beam position Veto
V2	250	250	-12.0	Beam position Veto
V2.1	250	250	-14.5	Beam position Veto
V3	6000	2000	-15.0	Beam halo Veto

A description and the positions of the trigger hodoscopes are given in table 3.7 as well as being shown in figure 3.2:

Table 3.7: Trigger Hodoscopes				
Name	1/2-Width (mm)	1/2-Height (mm)	**x**-Position (m)	Notes:
H1H	1250	630	3.3	
H1V	1260	650	3.3	
H3V	3750	1700	12.5	Sets timing for Trigger 1
H3H	3900	1725	12.8	Left and Right halves
H4H	5000	2175	18.3	Left and Right halves
H5	95	100	18.7	
H1'	275	229.2	8.6	
H3'	275	310.7	15.0	
H4'	252.5	428.2	20.1	Sets timing for Trigger 2
S1	162.5	152.5	8.5	
S2	210	185	14.0	
S3	210	190	15.5	
S4	275	220	21.3	Sets timing for Trigger 14
H3"	210	184	14.1	
H4"	275	219	21.2	

When an interesting event occurs the data acquisition system is thus triggered to start reading out the data from the pertinent part of the detector. The selection criteria of the fast electronics, for the formation of a trigger, are checked by programmable coincidence matrices[5], defined in table 3.8. In that table the "×" represents an element by element logical AND forming the matrix pattern. This pattern is then combined to form a logically OR to give the matrix output signal.

Table 3.8: Matrix definitions		
Matrix Name	Inputs	Purpose
M0	$H1V \times H3V_{Left}$	"Horizontal target pointing"
M1	$H1V \times H3V_{Right}$	(Forms a crude horizontal trajectory)
M2	$H3H \times H1H$	"Vertical target pointing"
M3	$H3H \times H4H$	(Forms a crude vertical trajectory)
M4	$(H3H \times H4H)_{Left}$	Halo
M5	$(H3H \times H4H)_{Right}$	(Both M4 and M5 are combined as "M4")
M6	$H1V \times H3H$	Minimum angle cut
M7	$H3V \times H3H$	Scaling
M8	$H1' \times H4'$	Trigger 2 - Timing

There were three main classes of triggers: (i) physics triggers, (ii) normalization triggers, and (iii) alignment and calibration triggers. Definitions are given in table 3.9, where "+" stands for a logical OR, "·" for a logical AND, "¯" (i.e., $\overline{\sum V}$) is a logical NOT or an anti-coincidence.

Table 3.9:
Trigger Definitions

Trigger	Definition	Purpose
T1	$(M0+M1)\cdot M2\cdot M3\cdot M6\cdot M7\cdot \overline{\sum V}$	Large Angle events (Physics)
T2	$(H1'\cdot H3')_{PLU}\cdot(H4'\cdot H3')_{PLU}\cdot M8\cdot \overline{\sum V}$	Small Angle events (Physics)
T3	$\sum_{i=3}^{18}(BHA_{-\theta})_i$	Beam flux Normalization
T4	$\sum_{i=3}^{18}(BHB_Z)_i$	Beam flux Normalization
T5	$H5A\cdot H5B$	Beam monitor
T6	$\overline{(M0+M1)\cdot M2\cdot M3\cdot M6\cdot M7}\cdot$ $H2_{PH}\cdot\overline{\sum V}\cdot BHA\cdot BHB$	Lepton flavor change
T7	$\sum_{i=25}^{30}(H3V)_i\cdot\sum_{i=12}^{18}(M4)_i$	Near beam halo
T8	$\overline{T7}\cdot\sum M4\cdot H3V\cdot V3$	Far beam halo
T9	10 MHz Pulser	Background studies
T10	Random	Beam flux Normalization
T11	$(H3H+H4H)\cdot V3$	Hodoscope efficiencies
T12	$(H3'+H4')\cdot V1.5$	Hodoscope efficiencies
T13	Start-of -burst / End of burst	Scalar readout
T14	$(S1^u\cdot S2^u\cdot S4^u+S1^l\cdot S2^l\cdot S4^l)\cdot(N_{BHB_Y}=1)\cdot$ $\left(\sum_{i=8}^{12}BHB_Z\cdot\overline{\left(\sum_{i=1}^{7}BHB_Z+\sum_{i=13}^{20}BHB_Z\right)}\right)\cdot\overline{\sum V}$	Small x_{Bj} events (Physics)
T15	$(M0+M1)\cdot(N_{H3V}\geq 2)\cdot(N_{M4}\geq 2)\cdot\overline{\sum V}$	Multi-muon events (Physics)

3.6.1. The physics triggers

There are three physics triggers: (i) Trigger 1, called the Large Angle Trigger (LAT); (ii) Trigger 2, called the Small Angle Interaction Trigger (SAIT) and (iii) Trigger 14, called the Small-x_{Bj} trigger (SX).

Trigger 1 is the main physics trigger. It covers an angular range of $\theta \geq 10$ mrad and uses the large hodoscopes H1H, H1V, H3V, H3H, H4H. The matrices, M0 and M1 (Table 3.8), form one large matrix. They correlate the vertically oriented hodoscope elements to give horizontal target pointing (crude tracking). This removes low momentum particles by removing events with very large scattering angles. Matrices, M2 and M3, correlate the three arrays of horizontally oriented hodoscope elements to give a vertical target pointing. Matrix M6 rejects particles that pass through the center of the detector, this results in rejection of events whose scattering does not exceed a minimum angle. The minimum angle limit, called a cut, imposes a lower limit on Q^2 as seen in equation 2.1. The matrix M7 removes low energy scattered muons, thereby rejecting events with very high ν and thus high y ($y = \nu/E \geq 0.9$). The effect of M6 and M7 cuts, i.e., on low Q^2 and high y removal, is to remove events from a kinematic region dominated by real photon emission. This is the region of high radiative corrections. A schematic diagram of the Trigger 1 logic is shown in figure 3.6.

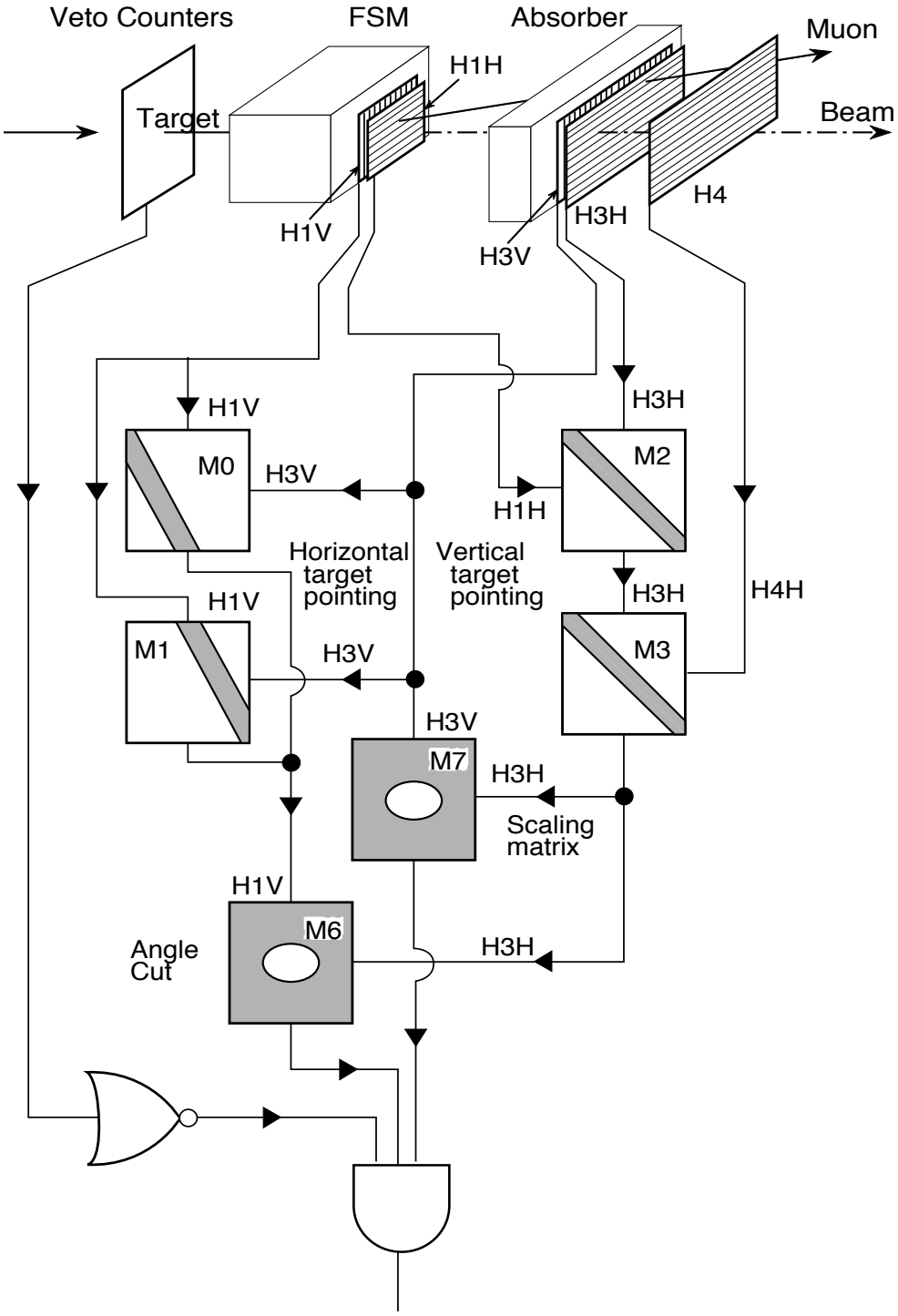

Figure 3.6: The Logic of the main physics trigger, T1.

Trigger 2 covers an angular range of $5 \text{ mrad} \leq \theta < 20 \text{ mrad}$ and partly overlaps with trigger 1. It uses the smaller hodoscopes; H1', H3' and H4', in conjunction with the Programmable Logic Units (PLU). The PLUs act as logical coincidence units but have poor time resolution. The timing is done by the matrix M8.

Trigger 14 covers an angular range of $2.5 \text{ mrad} \leq \theta < 10 \text{ mrad}$ and partly overlaps with trigger 2. It uses the small hodoscopes: S1, S2, S3 and S4; H3" and H4". The timing comes from hodoscope S4.

The physics triggers 6 and 15 are not discussed in this thesis.

3.6.2. The Normalization triggers

For the structure function analysis, the integrated beam flux is needed as input by the event simulation program, which is called a Monte Carlo simulation. The beam flux is then used to normalize the Monte Carlo simulation events to the number of data events. Therefore for each accepted event during data acquisition, a simultaneous count of the number of beam muons is made. There were two types of triggers used for the beam normalization: (i) Trigger 10 (the random[6] trigger) and (ii) Triggers 3 and 4, the two beam flux triggers.

Trigger 10 uses the random decay of an ^{241}Am, α source as a common start signal for the beam hodoscope TDC and a hit in the beam hodoscope element as the stopping signal. All the hardware veto information for these hits is also recorded. The beam tracks are then reconstructed with the same restrictions as with the normal physics events, if they occur within a ±10 ns time window of the start signal from the α source, from these hits in the beam hodoscopes. The beam flux is then given by:

$$\phi = \frac{N_{beam}}{w \cdot r}, \tag{3.1}$$

where N_{beam} is the number of reconstructed beam tracks, w the width of the time window and r the decay rate. The randomness of radioactive decay ensures a uniform sample of the beam, to an accuracy of about one percent.

Triggers 3 and 4 directly count the rate of beam muons on selected planes of the beam hodoscopes BHA and BHB, respectively. The number of hits in the central 16 elements of the beam hodoscopes are counted at a prescaled rate. The readout is triggered once for N actual events (commonly $N=2.56\times10^{6}$), and thus this reduced number of events is prescaled. The beam tracks from this sample of events are then reconstructed normally. This gives the flux with a statistical accuracy of better then 1% with only a few hours of data taking. The beam flux is given by:

$$\phi = \sum_{i=3}^{18} n_i w_i, \tag{3.2}$$

where n_i is the number of reconstructed tracks in element i and w_i is the weight assigned to that element number. It should be noted that the weight is usually the prescale factor N.

Trigger 13 is used to start the readout of the integrated flux scalars at the beginning and end of each burst of muons. Each burst lasted about 1.4 seconds and occurred with an interval of about 15 seconds.

3.6.3. The Alignment and Calibration triggers

The three triggers: (i) Trigger 5 (the beam trigger), (ii) Trigger 7 (the near halo trigger) and (iii) Trigger 8 (the far halo trigger), are used for software alignment, TDC calibrations and Multi-Wire Chamber drift time calibrations for the off-line data analysis. The software alignment is a method that determines the relative positions of the detectors using data taken under special circumstances. This method, along with the TDC and drift time calibrations, is discussed in section 4.1.

The two triggers: (i) Trigger 11 and (ii) Trigger 12 are used for the efficiency determination of the trigger 1 (LAT) and trigger 2 (SAIT) hodoscopes, respectively.

References: Chapter 3

1 C. Scholz, NMC Internal Report, NMC/90/21 (1990).

2 C. Best and A. M. Osborne, EMC Internal Report, EMC/78/26 (1978).

3 J. Gilles, EMC Internal Report, EMC/86/19:
M. Botje, NMC Internal Report, NMC/90/20:
M. Botje, NMC Internal Report, NMC/90/24.

4 D. Hungerford *et al., Nucl. Inst. & Meth.,* **A286** (1990) 155;
and references therein.

5 W. Flauger, CERN EP/79-25 (1979).

6 R. P. Mount, *Nucl. Inst. & Meth.,* **187** (1981) 401.

4. Data Processing

The data processing starts after the data has been collected by the spectrometer and written on magnetic tapes. A "run" was defined by collecting enough events to fill one tape and lasted approximately one hour. One tape contains about 50,000 raw events. After each run the target setup was changed (See section 3.2). Before data reconstruction and analysis can proceed, the various detectors must undergo "calibration", "alignment" and "fine tuning". This process is called Software Alignment. These terms are described in more detail in the following section.

4.1. Software alignment and calibration

The software alignment and calibration are done in four steps. The first three steps use special data that were taken at low beam intensity with the FSM magnet turned off and all targets removed from the beam. The remaining step uses normal data tapes. These four steps are:

(1) The time calibration of the Time to Digital Converters (TDCs) for all the hodoscopes is calculated.

(2) The offset time and velocity calibrations of the multi-wire drift chambers are performed.

(3) The spatial alignment of all the detectors is determined.

(4) The various input parameters for the data processing are fine tuned.

4.1.1. Time to Digital Converter calibrations

In a high data rate environment a method is needed to select desired tracks from a background of one or more coincident tracks. Therefore one needs to differentiate multiple tracks; by associating the beam tracks and the scattered muon tracks with the triggers. To do this the absolute and relative timing of the various hodoscopes must be determined.

The H3V trigger hodoscope is located behind the hadron absorber (see figure 3.2). Therefore one can deduce that it sees only scattered muons. The H3V trigger hodoscope sets the timing for the main physics trigger and thus for the whole experiment. H3V has two photo-multiplier tubes with TDCs per element, one at each end. By selecting tracks in which the hodoscopes H3H and H4H are also hit, the **z**-position along the vertical elements of H3V is measured. The base TDC offset time, T_0, is adjusted by taking the difference in times between the upper and lower TDC for each element to give a net time of zero at the position $z = 0$. The offset time is the time added to the measured time of one element to bring it into coincidence with all the other hodoscope elements. The other triggers are all calculated relative to this average time (approximately zero).

The other two physics trigger hodoscopes have only one TDC per element. Their T_0s are adjusted such that the times of all the TDCs are centered at zero for "good" reconstructed tracks. The TDCs for H4' for the SAIT trigger and the TDCs for S4 for the SX trigger are calibrated and checked with raw data tapes, filtered for their respective triggers, rather then with special "low intensity" tapes. The filtering accepts only those events with the selected triggers.

The TDCs of the Beam Momentum Station hodoscopes and the beam hodoscopes are each adjusted such that all the times of the individual elements are centered at zero and the individual planes are in time with each other. Then the BMS TDCs and the BH TDCs are adjusted to have a relative time between them of zero. Because both of these hodoscopes are used with the track reconstruction of trigger 10, times far from the nominal value of T_0 are measured. If the TDCs are not perfectly linear then there would be a slope in the distribution of measured times versus expected times, relative to the measured T_0. By using delayed and non-delayed pulses as input to these TDCs a measure of any non-linearity, thus a slope, has been determined and corrected for in the calculation of the TDC time of the BMS and beam hodoscopes. In this process the difference in times is divided by the known delay time to calculate the slope.

4.1.2. Drift time calibrations

For the multi-wire drift chambers one has to determine the TDC offset time, T_0, the drift velocity of the electrons, V_{drift}, and the parametrization of the non-linearity of the drift velocity in the electric field. The non-linearity of the drift velocity is seen by measuring the drift velocity as a function of position within the drift cell. The parameter T_0 is defined as the maximum drift time for an electron in that chamber and is taken relative to the trigger time. Maximum drift time occurs in the case for a track originating at the farthest point from the sense wire in a drift cell. In a multi-wire drift chamber this is a distance typically equal to half of the wire spacing of the chamber.

The calibration is an iterative process that starts with a reasonable set of values of T_0, V_{drift} and the assumption that one is in a region where the drift velocity is reasonably linear. Special low intensity data tapes are taken for calibration purposes with the FSM

field equal to zero. Because there is no deflection by magnetic force, tracks are parallel to the incoming beam. Such tracks are reconstructed and a best fit is found. A "residual" is the difference between the best fit and the measured track position. These are plotted versus the expected position in the drift cell. From these plots, by assuming that one is in a region where the position versus time of the drift cell is linear, approximate values of T_0 and V_{drift} are extracted. The value of V_{drift} is obtained from the slope of the position versus time plot and that of T_0 from the intercept. After a few iterations these values have converged. Finally, the correction to the non-linearity of the drift velocity must be parametrized.

This parametrization is obtained by fitting a polynomial function to the deviation from a straight line of the plot of residual versus time, in the drift cell. This is also an iterative process since this correction is then applied to the track reconstruction used in the calculation of the residuals. The degree of the polynomial depends on the uniformity of the electric field, seen in the plot of position versus time, and thus on the chamber construction and the gas that was used.

The W12 and W3 chambers had three field shaping wires and the W67 chambers had a "graded field". Therefore the W12 and W3 chambers are somewhat more linear than the W45 chambers. The W67 chambers are, by comparison to the other drift chambers, very linear. The W67 chambers use a polynomial fit of the forth order. The W12, W3 and W45 chambers use a polynomial fit of the sixth order. Examples of this are shown in figure 4.1, the plots of the non-linearity correction versus the drift time for the W12, W45, W67 and W45 drift chambers.

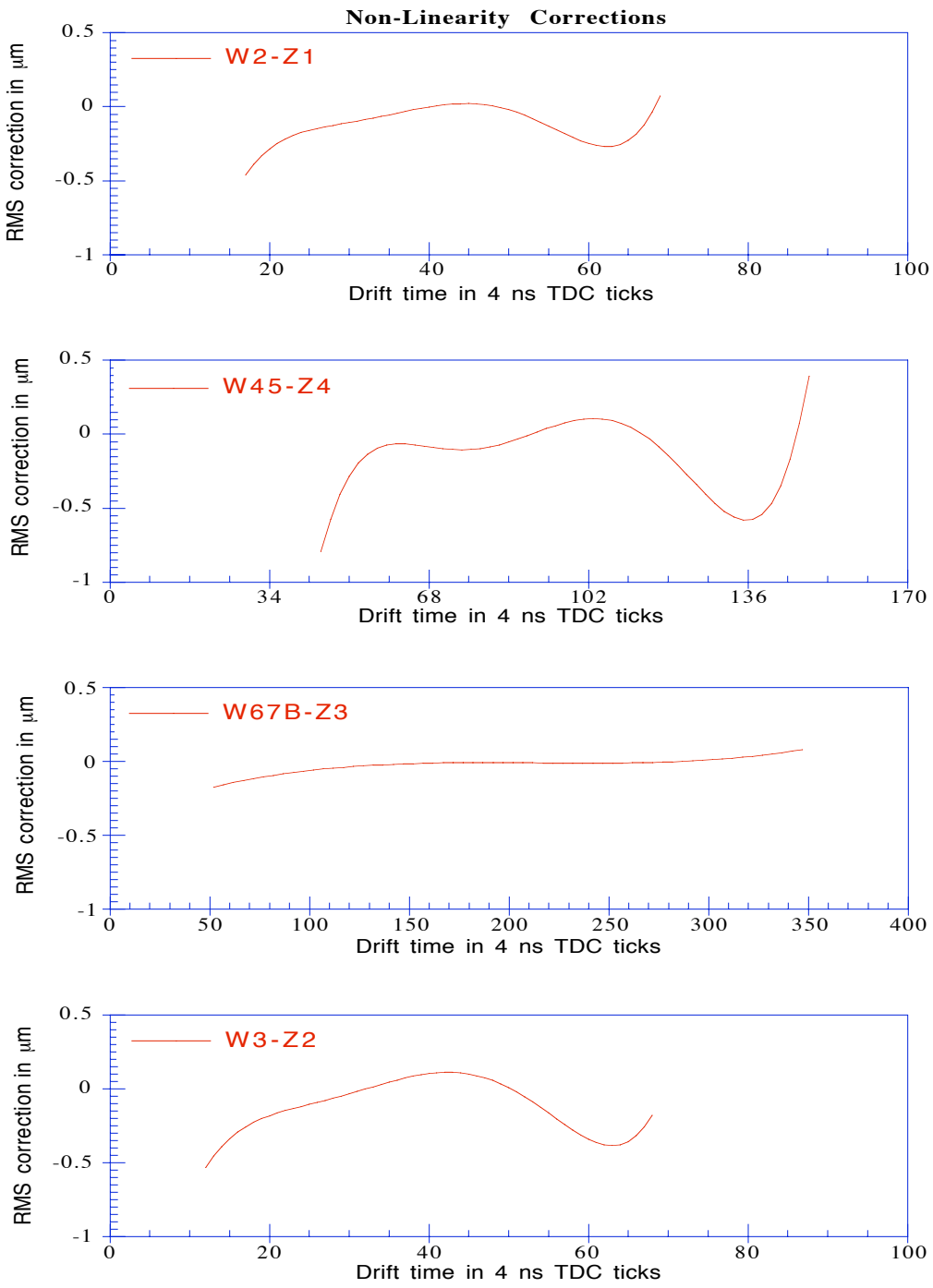

Figure 4.1:
The Non-Linearity Corrections versus Drift time.

4.1.3. Spatial alignment

To make high precision measurements the position of the various detectors must be accurately known. The procedure of determining the detector position is called the spatial alignment. This procedure has two phases; (i) all the detector positions are optically surveyed; (ii) software is used to reconstruct tracks, and to refine the measurement of chamber positions based upon the straight line character of the tracks.

The optical surveying of the detectors, from the positions of fixed reference points, is done at the beginning of a period of data taking and is repeated when any detector is moved. This procedure gives the **x**-position (along the beam) of a survey marker on a detector. The first wire (or element) position, relative to its survey point, is then deduced from a knowledge of the internal construction of the detectors. The first wire (element) position is then used as the starting point for the software alignment.

The general method of software alignment is fairly simple; for each readout plane in a given detector one reconstructs tracks and compares them with their expected position. The expected positions are determined by the best fit of a track, reconstructed from the rest of the detectors, and from the survey. The difference is applied as a correction to the position of the readout planes. The difference between the expected position and the reconstructed position is called the residual. The residuals of a number of tracks are then plotted and the average is applied as the correction to the position of the plane. This is an iterative process that continues until it converges. This is only possible when using tracks that are straight and unambiguous. For this reason the special data tapes, taken at low intensity with the FSM turned off, are used.

The method proceeds by separately aligning three groups of detectors; first each detector in each group is aligned to itself and then the sets of detectors within each group are aligned relative to each other. Finally the groups are aligned relative to each other. The three groups of detectors are: (i) the detectors located downstream of the hadron absorber (See figure 3.2); (ii) the large detectors located in front of the hadron absorber; and

(iii) the beam and small proportional chambers.

The alignment of the detectors located downstream of the hadron absorber uses low intensity halo triggers (T7 and T8). Here each set of the W67 chambers (The A, B and C sets are shown in figure 3.2) is first aligned independently and then, using the overlap between the W67A and W67B modules and the overlap between W67B and W67C modules, they are aligned relative to each other. At this time the P67 and W3 chambers are also aligned relative to W67B. Also the large trigger hodoscopes H3V, H3H and H4H; along with the SAIT trigger hodoscope H3' and H4' are aligned with respect to W67B.

The alignment of the detectors located in front of the hadron absorber uses a low intensity halo trigger (T7). Here each of the detectors; W45, P45 W12, P123 and PV12, first had their internal planes aligned independently with respect to themselves. They are then aligned relative to each other. At this point the large trigger hodoscopes H1V and H1H; along with the SAIT trigger hodoscope H1' are aligned with respect to this group of detectors. Finally the W67 system is aligned relative to this group of detectors.

The alignment of the beam and small proportional chambers uses a low intensity beam trigger (T5). Here each of the small proportional chambers, the P0s (P0B, P0C,

P0D, P0E and P0A), and the beam hodoscopes are aligned with respect to beam tracks found using the PV12 and P45 chambers. This procedure directly aligns the P0s and the beam hodoscopes relative to the other detectors.

The various detectors are aligned by the software process to within a one or two tenths of a millimeter. However, it should be noted that the alignment of the detectors is only made relative to each other. The absolute position still is taken from the optical survey, and this knowledge is used to assure good alignment between the detectors and the FSM and targets. The best check on the **x**-position of the detectors by the software alignment procedure is unfortunately accurate to only ±1 centimeter. Therefore, because of the small track angles involved (due to the small opening angles seen in the physics of a fixed target detector), the optical survey of the **x**-position is by far the best possible measurement.

4.1.4. Fine tuning

The fine tuning of the various parameters includes: (i) determining the "road widths" (to be defined below) for all groups of detectors (with different road widths set for each of the physics triggers); (ii) the fine tuning of the spatial alignments and the linking of the tracks through the hadron absorber; (iii) the timing of the veto counters and the determination of the cuts on the allowed slope and position of the beam trajectory. This fine tuning is all done with regular data tapes.

The track reconstruction program is called *Phoenix*[1]. The road widths and the plane requirements for each detector are determined in a procedure known as "Phoenix tuning", which fine tunes some of the input parameters for the program *Phoenix*. The road width is the maximum distance from a track that is allowed for a hit in a detector to

be considered as part of that track. Tracks are found using a least squares fit to a straight line. A hit in a detector outside the allowed road width is rejected from the fit. Therefore a balance between having too large a road width, thus distorting the track trajectory with spurious hits, and having too small a road width, thus loosing too many good events, is determined in this procedure. Separate road widths are determined for each of the physics triggers. The so called "plane requirement" is the minimum number of hits, within the road width, per coordinate needed to form an acceptable track.

The event reconstruction program is called *Geometry*[2]. The linking of tracks across the hadron absorber and the fine adjustments of the spatial alignment for each detector are determined in a procedure known as "Geometry tuning". Because there is a residual magnetic field[3] in the hadron absorber the muons that pass through the absorber are deflected. A parametrization of this deflection must be made to link the muons tracks, behind the absorber, to the detectors in front of the hadron absorber. The spatial alignment and acceptable error of the detectors are fine tuned using normal data.

In a procedure known as "Veto tuning", the relative timing of the veto hodoscope TDCs is set. This is to ensure, or at least reduce the chance, that a good track is not mistakenly vetoed by an out-of-time halo muon. The veto tuning uses output from the data reduction program called *Snomux*, i.e., partially processed data summary tapes called Mini-DSTs. The times are used as input to the final data processing program, *Snomin*.

The determination of cuts on the position, slope and radius of allowable beam tracks is done in a procedure called "Beam tuning". This ensures that all acceptable beam tracks pass through the full length of both of the targets. Also the range of acceptable

beam momentum is set by the beam tuning. The beam tuning also uses as input the Mini-DSTs and has its results used as input by the program *Snomin*.

4.2. Data reconstruction

The data reconstruction is done in three steps:

- Track reconstruction.
- Momentum calculation of both the beam and scattered muon and the vertex fitting.
- Beam processing, normalization trigger processing and data reduction.

The data reconstruction procedure has been given in far more detail elsewhere[4]. However, the basic method is shown in figure 4.2, which is a block diagram of the flow of data through the NMC data processing chain.

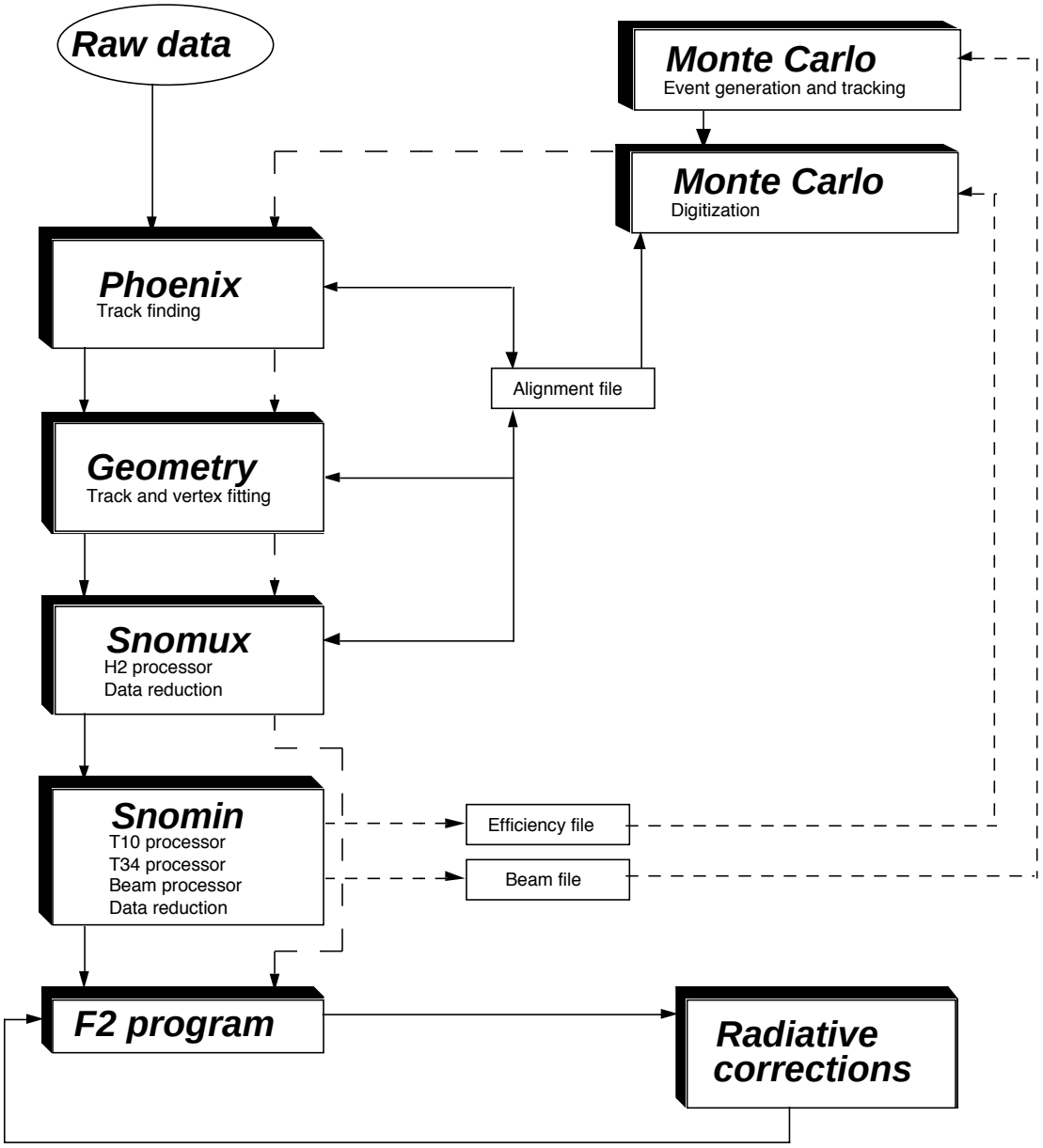

Figure 4.2: A flow chart of the NMC data processing chain.
(The details of the data reconstruction are given in the following sections.)

4.2.1. Track reconstruction

Track finding and reconstruction is done using the program *Phoenix*[1]. The program first looks for a beam track in both the beam hodoscopes and the beam momentum station. If a beam track is found then a search is made for tracks that are found behind the hadron absorber that are identified as muons because of their penetrating ability. If and only if one or more muons are found, the track finding process continues by looking for hadrons. Hadrons are identified as tracks that are found only in front of the hadron absorber. The resulting numbers of events for a typical data "run" analyzed by *Phoenix* is given in table 4.1:

Table 4.1: Event reduction in *Phoenix*

	Trigger 1	Trigger 2	Trigger 14
Input event triggers	5364	21524	11891
Output of accepted events	2515	5632	2632
Percentage of accepted events	46.9%	26.1%	22.1%

After this filtering process the tracks are reconstructed and used as input in the event reconstruction program called *Geometry*.

The numbers shown in table 4.1 tend to be very stable from run to run as shown in figure 4.3. This figure shows the fraction of accepted events per input event versus the number of runs processed for each physics trigger. The step seen in the beginning runs of T14 was caused by the adjustment of the high voltage in one module of W3. The small drop at the end of both T2 and T14 has no simple explanation and these runs were later removed from the data analysis.

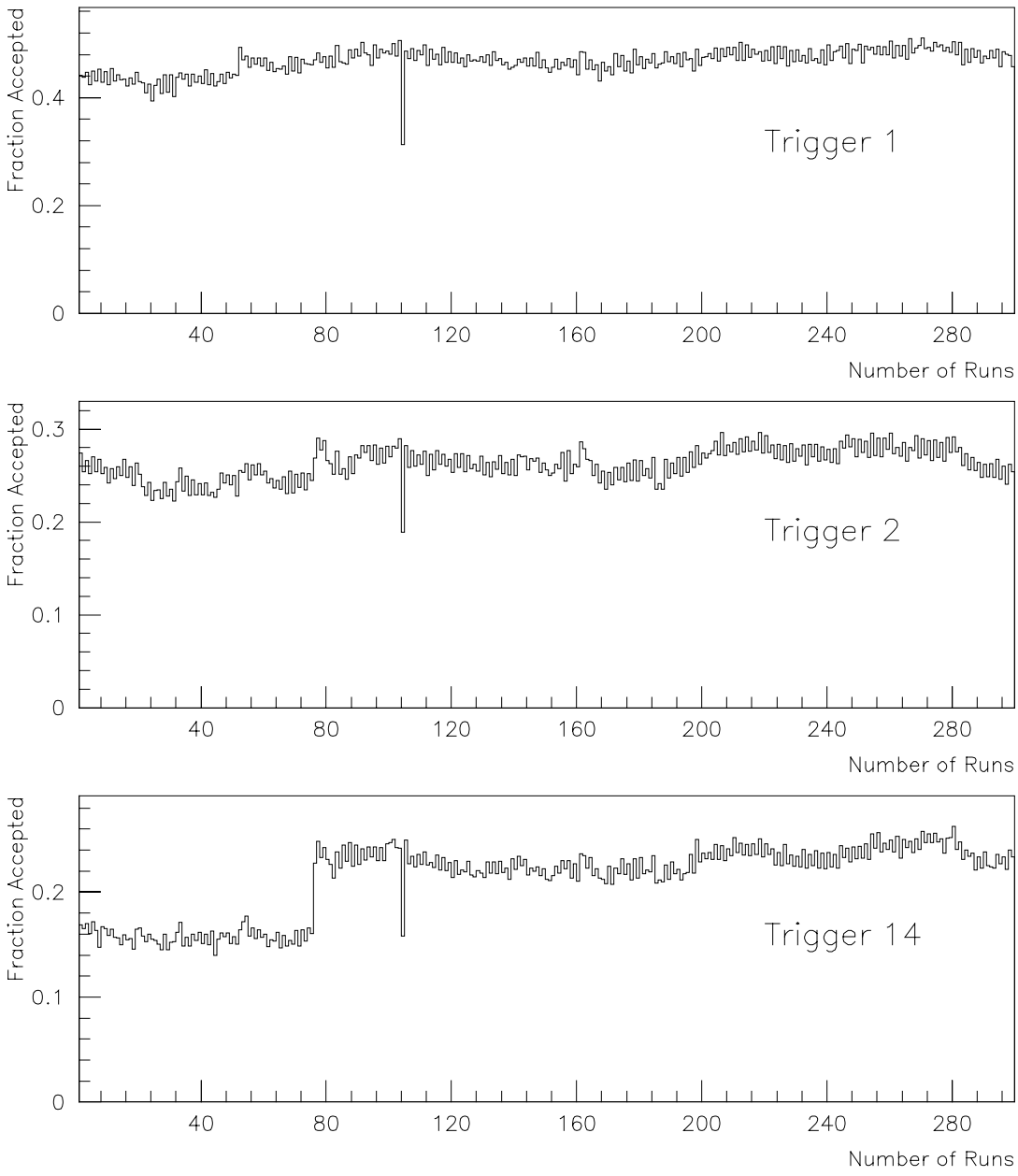

Figure 4.3:
Track reconstruction by *Phoenix* versus the number of runs processed.

4.2.2. Event reconstruction

The track and vertex fitting are done using the program *Geometry*[2]. This program determines the momenta and trajectories of both the incoming beam track and the scattered muon or hadron tracks. Then, by connecting the beam track and the scattered muon track, the program determined the interaction vertex.

The beam tracks are fit using the beam hodoscopes, the proportional chamber P0H and possibly the proportional chamber P0B. The scattered muon tracks are fit by taking the best fit of the detector hits to the tracks behind the hadron absorber. The hadron tracks and the scattered muon track are fit by taking the best fit to the tracks between the absorber and the FSM (See figure 3.2). The portion of the scattered muon track in front of the hadron absorber is then determined by linking these tracks through the absorber. A track that continues past the hadron absorber is identified as a muon while those that do not continue beyond the absorber are identified as "hadrons". While this definition is poor nomenclature, since it includes hadrons, electrons and photons, the differences are determined in a separate analysis not covered by this thesis. These tracks are then fit, using a spline[5] fit, through the bending magnet and connected to the tracks from the region between the FSM and the target. A spline fit is a technique for interpolating a function between a series of fixed values, in this case the positions of hits in the magnet chambers. The projection of the track in the vertical **x**-**z** plane should be a straight line while the projection in the **x**-**y** plane should be a segment of a circle whose radius is:

$$r = \frac{|\mathbf{P}|}{q|\mathbf{B}|}. \tag{4.1}$$

P is the particle momentum, **B** the field of the FSM and q the charge of the particle. The momentum of the particle is thus calculated from the connected tracks. This is done using the difference in the angle between the track entering and leaving the magnet and the radius calculated from the spline fit.

The intersection of the beam track and the scattered muon track (allowing for multiple scattering in the target material) is then used to find the vertex. If the vertex is found to be downstream of P0B then the beam track is recalculated using P0B hits to improve the fit; if the vertex is found to be upstream of P0B then the hits in P0B are used to improve the scattered muon track. (See figures 3.2 and 3.5)

The hits from the scattered muon track in the trigger hodoscopes are checked to ensure that no false hardware trigger was used and to determine which software triggers accompany a track. While no actual data reduction is done in *Geometry*, all events are flagged with information that indicates whether or not it has good tracks. A measure of whether a track is good is that it has both a software trigger and a vertex. The stability of the data processing in *Geometry* is shown in figure 4.4. Here the fraction of events with both a vertex and a trigger, versus the number of runs processed, is plotted for each software trigger.

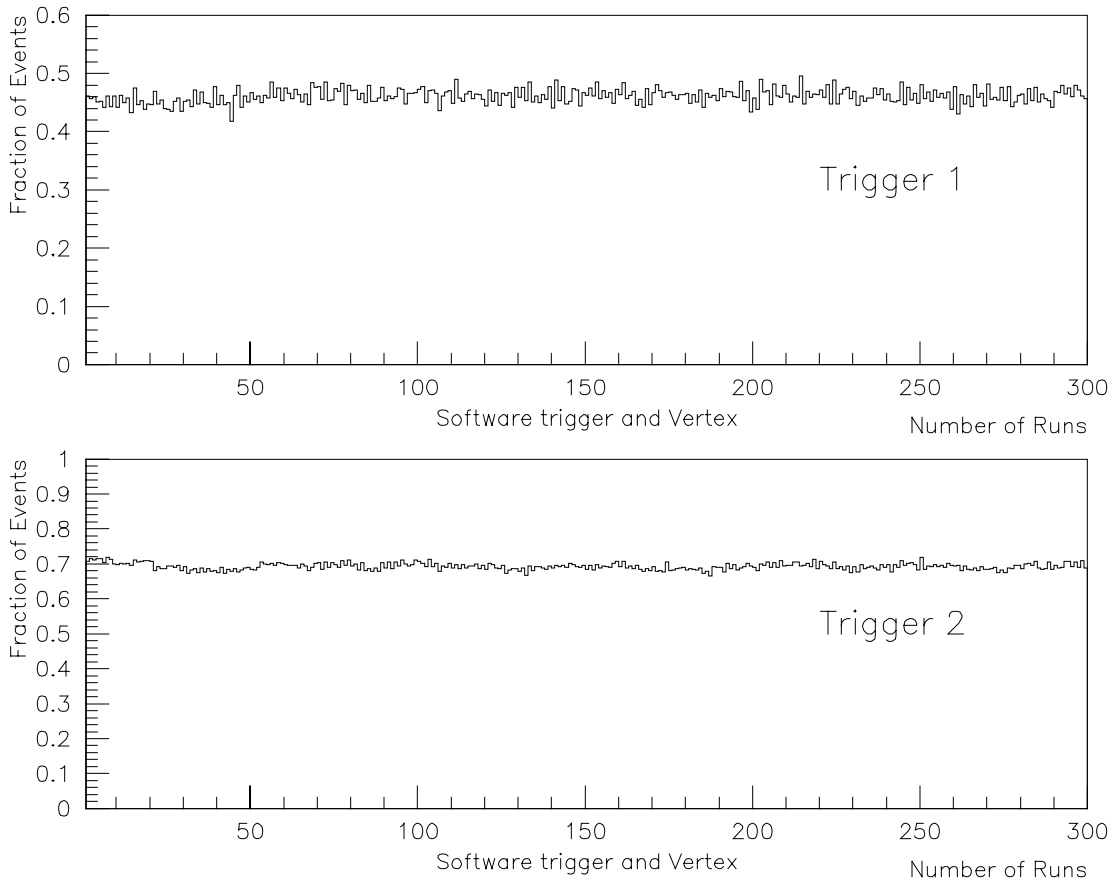

Figure 4.4:
The fraction of events yielding acceptable tracks in the program *Geometry*.
(The stability of the track and vertex fitting in *Geometry* is evidenced by the constant fraction versus the number of runs processed.)

4.2.3. Data reduction

The data reduction and final processing are done by two programs *Snomux* and *Snomin*. The hadron processing (H2) along with the preliminary data reduction is done in *Snomux*. Only the events flagged in *Geometry* as having both a vertex and a software

trigger are used. From these events only minimal information is extracted. Then the data of the event are packed into as few "computer" words as are possible and written on tape. This tape is called a Mini-DST.

In the program *Snomin*, the processing of the normalization triggers, the "beam processing" and the final data reduction is done. During the T3/4 and T10 processing the event weights are calculated for these normalization triggers. The beam processing produces a file with the T10 beam track parameters and beam hodoscope hits for use as input to the event simulation program. The event reduction is done by making final cuts on the data and compressing the remaining data onto a Micro-DST. These cuts require that the beam track is within the target at the upstream and downstream limits, that the beam is within the hole in the veto chamber V2, that the incident muon momentum is measured and that restrictions are put on the track momentum, **y**-slope and **z**-slope parameters. The reduction in data for a typical run is shown in table 4.2:

Table 4.2:
Event reduction

	Trigger 1	Trigger 2	Trigger 14
Input events: *Snomux*	2515	5632	2632
Events output by *Snomux* (and input to *Snomin*):	1389	3968	1850
Output events: *Snomin*	984	2783	1603
Percentage remaining	30.1%	49.4%	60.9%

The number of raw input and final number of output events is given in table 4.3:

Table 4.3:
The summary of data processing

	Trigger 1	Trigger 2	Trigger 14
Raw data events	1.6×10^6	6.4×10^6	3.4×10^6
Output events on Micro-DST	288782	799192	354273
Percentage remaining	18.0%	12.5%	10.4%

4.3. Monte Carlo event simulation

A simulation of the behavior of the experimental apparatus is used to determine the acceptance of the detectors in terms of both geometrical acceptance and the efficiency. A program that simulates the behavior of the experimental apparatus using randomly generated physics events, as this program does, is called a Monte Carlo program. For this analysis the Monte Carlo program is used to generate only the beam and scattered muon tracks. This program has two stages, the event generation stage and the digitization stage. The resulting simulated digitized data is fed through the normal data processing chain.

The event generation stage uses the programs *GEANT*[6] and *Gmuon*[7] to simulate the detector positions and to generate tracks in the spectrometer. The beam file discussed in section 4.2.3 is used as input to properly reconstruct the beam phase space and the changes of the target setups. The interaction vertex is randomly generated along the beam direction in the target, depending on the densities of the target materials, in the upstream and downstream targets. The kinematics of the scattered muon are generated in the

independent kinematical variables ν and Q^2. The variables are randomly generated, for a uniform distribution of ν and $1/Q^2$, in the range from ν_{min} to ν_{max} and from Q^2_{min} to Q^2_{max}.

In the digitization stage, the program *Digimc*[6] uses the tracks generated in the first stage and then applies the efficiencies of all the detector planes to each track and generates the simulated hits in the detectors. These detector hits, which are a simulation of the raw data, are then fed into the normal data reconstruction chain of programs. This was done to ensure reconstruction of these Monte Carlo events under the same conditions as for the data reconstruction, including any reconstruction losses due to software algorithms. In the structure function analysis only trigger 1 events were generated. To produce this data five passes through the beam file were used; each pass using a different set of random numbers for event generation. The *GEANT* Monte Carlo program originally generated 1,129,150 events and, after passing through the normal data processing chain, a total of 263,619 Monte Carlo events was produced on the Micro-DST.

References: Chapter 4

1 I. G. Bird, NMC, “Phoenix”, NMC Internal Report, NMC/90/8 (1990).

2 I. G. Bird, NMC, “Geometry”, NMC Internal Report, NMC/90/9 (1990).

3 J. Gilles, EMC Internal Report, EMC/86/19:
M. Botje, NMC Internal Report, NMC/90/20:
M. Botje, NMC Internal Report, NMC/90/24.

4 I. G. Bird, Ph. D. thesis, Vrije Universiteit, Amsterdam (1992);
I. G. Bird, NMC, “Phoenix”, NMC Internal Report, NMC/90/8 (1990);
I. G. Bird, NMC, “Geometry”, NMC Internal Report, NMC/90/9 (1990).

5 LINTRA write-up CERN Program Library, and references therein.

6 R. Brun *et al.,* GEANT version 3.14/16 user guide, CERN Program Library (1990).

7 I. G. Bird, Gmuon write-up, NMC Internal Report NMC/91/1 (1991).

5. Analysis of the ratio F_2^n/F_2^p

5.1. Introduction

The F_2^n/F_2^p ratio is related, in the quark-parton model, to the ratio of the down and up quark momentum distributions (See section 2.2). An accurate measurement of the F_2^n/F_2^p ratio puts strong constraints on the parton distributions. For a reliable calculation of hard scattering cross sections in proton-proton, electron-proton and antiproton-proton collisions, the precise knowledge of parton momentum distributions is important, especially in the low x_{Bj} region. The F_2^n/F_2^p ratio can also be used to test the Gottfried sum rule (see section 2.2) and to set a constraint on shadowing in deuterium. This chapter includes a description of the method to measure this ratio, a discussion of systematic errors and a presentation of the physics results.

To measure the total scattering cross section, σ_{Total}, one would have to determine the measured number of interactions, then integrate the beam flux, ϕ, (the number of incident particles per unit area of the incident beam, integrated over the measuring time) and determine the number of scattering centers per unit area, ρ, in the target. The number of observed interactions is equal to the product of the actual number of interactions and the acceptance, A. The acceptance is determined by the total solid angle covered by the experiment, the trigger efficiency, and the track reconstruction efficiency.

One therefore has:

$$N_{Measured} = \phi \rho A \sigma_{Total}. \tag{5.1}$$

In the ratio measurements two target setups were alternately exposed to the beam (See figure 3.5). The target setup was exchanged in the beam every run during P3A89. A run was defined by the amount of data used to fill one round-tape. This was typically about 50,000 events of raw data, and represented about an hour of beam time. P3A89 contained approximately 300 runs of useful data.

5.2. The Method

The method of determining the ratio F_2^n/F_2^p with the complimentary target set up, which is described in section 3.2, has the advantage that systematic errors due to spectrometer acceptance and beam flux are greatly reduced. This allows a very precise measurement because the accuracys with which the acceptance and flux can be determined does not contribute to the systematic errors.

The cross sections are calculated from measured variables via eq. (5.1). In determining the ratio of F_2^n/F_2^p one starts with the calculation of the ratio of deuteron and proton cross sections, σ_d/σ_p. The cross section ratio σ_d/σ_p, using the data from all targets, can be written as:

$$\frac{\sigma_d}{\sigma_p} = \sqrt{\frac{\sigma_d^{up}\,\sigma_d^{dn}}{\sigma_p^{up}\,\sigma_p^{dn}}}, \tag{5.2}$$

where up and down indicate upstream and downstream targets, respectively. Using for each target, e.g.,

$$\sigma_d^{up} = \frac{N_d^{up}}{A_d^{up}\,\phi_1^{up}\,\rho_d}, \tag{5.3}$$

one can rewrite eq. (5.2) as follows:

$$\frac{\sigma_d}{\sigma_p} = \sqrt{\frac{N_d^{up} N_d^{dn}}{N_p^{up} N_p^{dn}} \frac{\phi_2^{up} \rho_p A_p^{up} \phi_1^{dn} \rho_p A_p^{dn}}{\phi_1^{up} \rho_d A_d^{up} \phi_2^{dn} \rho_d A_d^{dn}}}. \tag{5.4}$$

The integrated fluxes for the two target settings (See section 3.2) are indicated by ϕ_1 and ϕ_2. A cut is made on the slope and position of the incoming beam muon to ensure that the beam tracks are contained within both the upstream and downstream targets. The interaction probability is sufficiently small that the change in the flux along the length of the target can be ignored. This implies that the flux is the same in the upstream and downstream targets for the same target setup, thus $\phi_1^{up} = \phi_1^{dn} = \phi_1$ and $\phi_2^{up} = \phi_2^{dn} = \phi_2$. The acceptance of the spectrometer primarily depends on the **x**-position of the interaction vertex and not on the target material. If the track reconstruction probability does not change between the runs with target setup-1 and target setup-2, the assumption can be made that the acceptance in both target setups is the same for each of the upstream and downstream targets, thus $A_d^{up} = A_p^{up} = A^{up}$ and $A_p^{dn} = A_d^{dn} = A^{dn}$. For such cases the expression for σ_d/σ_p reduces to the simple formula:

$$\frac{\sigma_d}{\sigma_p} = \kappa \sqrt{\frac{N_d^{up} N_d^{dn}}{N_p^{up} N_p^{dn}}}, \tag{5.5}$$

where κ is the ratio of the number of nucleons per unit area in the respective targets. The formula for κ is given by:

$$\kappa = \frac{\rho_p}{\rho_d} = \frac{V_{D_2}^{mol}}{V_{H_2}^{mol}} \frac{L_{H_2}}{L_{D_2}}, \tag{5.6}$$

in which V^{mol} and L are the molar volume and the length of the target, respectively. The value for κ, as determined in appendix 8.1, is κ=0.8664±0.0002.

The measured cross section is the <u>total</u> cross section. It contains on top of the dominant one-photon absorption parts the higher order, primarily radiative, contributions to the cross-section. (See, e.g., (a-d) in figure 2.6) The ratio F_2^n/F_2^p is related to the cross section given in eq. (2.20). The radiative corrections, as discussed in chapter 2.4, are then applied as a weight to each event. This weight η is the ratio of the one photon cross section to the total cross section, which contains the higher order corrections: $\eta = \sigma^{1\gamma}/\sigma_{Total}$. The number of events, for each target, in eq. (5.5) is then to be replaced by the accumulated weights, for obtaining the one photon cross section ratio $\sigma_d^{1\gamma}/\sigma_p^{1\gamma}$. Neglecting effects from nuclear binding, σ_d is simply given by $\sigma_d = \sigma_n + \sigma_p$. By using eq. (2.20), where the structure function F_2 is defined per nucleon, and by making the assumption that $R_d = R_p$, the expression for the ratio $\sigma_d^{1\gamma}/\sigma_p^{1\gamma}$ reduces to:

$$\frac{\sigma_d^{1\gamma}}{\sigma_p^{1\gamma}} = 2\frac{F_2^d}{F_2^p}. \tag{5.7}$$

Therefore, we can now express the desired quantity F_2^n/F_2^p in numbers of weighted events:

$$\frac{F_2^n}{F_2^p} = 2\frac{F_2^d}{F_2^p} - 1 = \kappa\sqrt{\frac{N_d^{up}N_d^{dn}}{N_p^{up}N_p^{dn}}} - 1, \tag{5.8}$$

where the numbers $N = \sum_{i=1}^{N}\eta$ are the accumulated weights for each target position.

5.3. Systematic studies

Systematic studies were performed to find and remove from the data those parts for which the assumption about the flux and acceptance cancellation are not valid, or in doubt. The parts of the data where time dependent effects were observed in either: the ratio of the number of accepted events with respect to the beam flux, the average number of reconstructed events per detector or, the average values of the kinematic variables, were found and excluded from further analysis.

5.3.1. Time Dependent Studies

A simple method for examining long term variations in the operating condition of the spectrometer, and thus the acceptance, is to plot variables versus run number. The typical duration of one run was one hour. An example of a run dependent plot is shown in figure 5.1, where the acceptance ratio A^{up}/A^{dn} (defined below) is given versus run number. The gaps at various run numbers correspond to special alignment and calibration runs, which are excluded from the final data analysis.

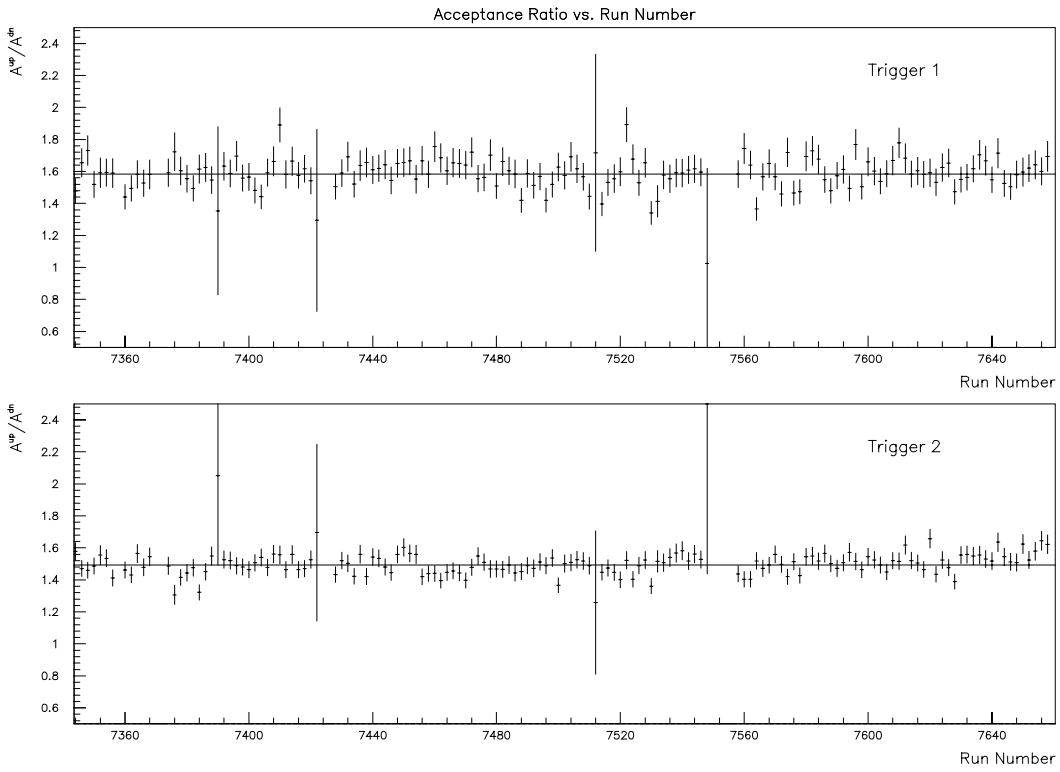

Figure 5.1:
The acceptance ratios A^{up}/A^{dn} versus run number for both trigger 1 and trigger 2.

Here the acceptance ratio is defined as the ratio of the number of events from the upstream and downstream targets, by combining the numbers of events for the two target positions. Using eq. (5.4) and making the assumptions that the cross sections for each material are independent of the target position ($\sigma_p^{up} = \sigma_p^{dn}$ and $\sigma_d^{up} = \sigma_d^{dn}$) and that the beam flux is the same in both the upstream and downstream targets, thus $\phi_1^{up} = \phi_1^{dn} = \phi_1$ and $\phi_2^{up} = \phi_2^{dn} = \phi_2$, the acceptance ratio is given by:

$$\frac{A^{up}}{A^{dn}} = \sqrt{\frac{N_d^{up} N_p^{up}}{N_p^{dn} N_d^{dn}}} . \tag{5.9}$$

The acceptance ratio is seen to be constant over time for both trigger 1 and trigger 2. Therefore it was concluded that there were no time dependent changes that affected the whole spectrometer.

Another method to check the stability of the spectrometer's performance is to examine the ratio of the number of accepted events to the beam flux, as measured by the dedicated normalization triggers. Those ratios are plotted versus run number for the two different normalization triggers, Trigger 3/4 and Trigger 10. Using these plots, any runs that significantly deviate from the average were removed after it had been checked that they corresponded to problematic runs according to the logbook. Figure 5.2 shows plots of the ratios of accepted normalization triggers 10 and 3/4 to both triggers 1 and 2 accepted events versus run number. In these plots, run number 7455 was significantly different from the other runs. Since this ratio is higher than average, this means that there was a deficit of T1 and T2 data processed which indicates a problem with the spectrometer. Indeed during that run the readout electronics for one detector (W12) failed therefore this run was removed from further data analysis.

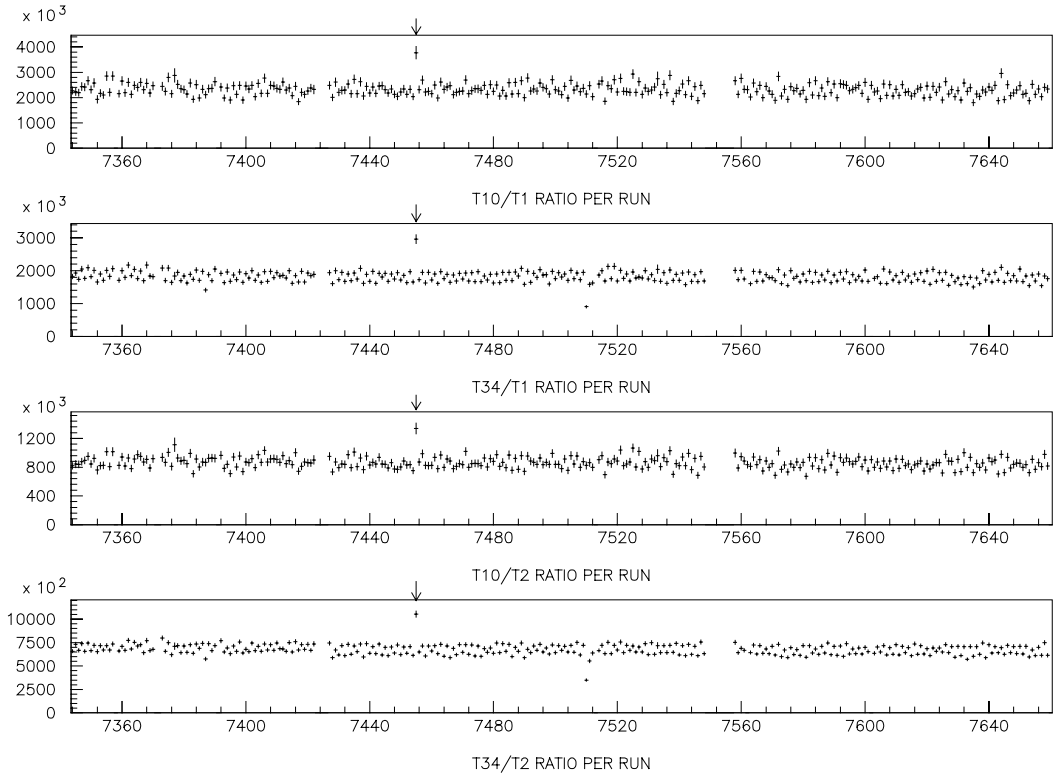

Figure 5.2:
The ratio of the beam normalization triggers (T3/4 and T10) to the physics triggers 1 and 2 versus run number.

The fraction of reconstructed events used in the muon reconstruction for the detector (or the average time), versus run number, are also plotted to check for any time dependent change. Examples are seen in figure 5.3 for trigger 1 and in figure 5.4 for trigger 2. The plots that show an alternating value (the top ones) reflect the difference in the acceptance between the upstream and downstream targets, magnified by the different number of events produced in hydrogen or deuterium. A problem with the detector is seen by the jump in the average time from the Beam Momentum Station's TDCs in both

figures 5.3 and 5.4, along with a jump in the average time from the trigger time of trigger 2 in figure 5.4, near run number 7640.

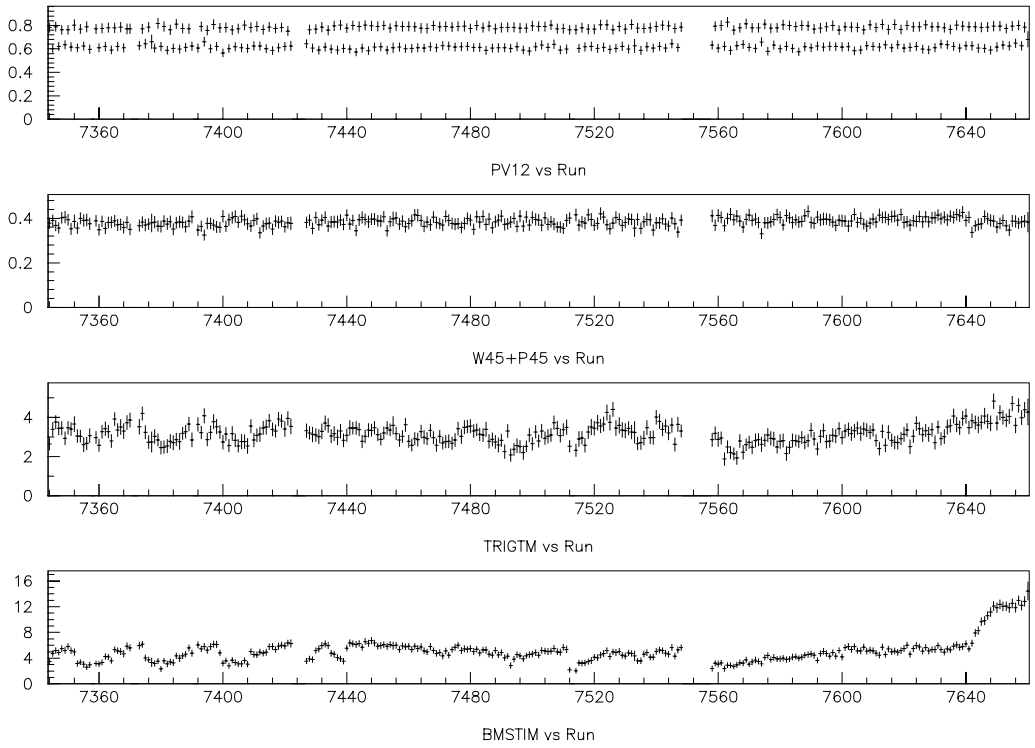

Figure 5.3:
The fraction of reconstructed trigger 1 events for the detectors PV12 and W45 and the average trigger and BMS TDC times (in units of 0.1 ns) versus run number.

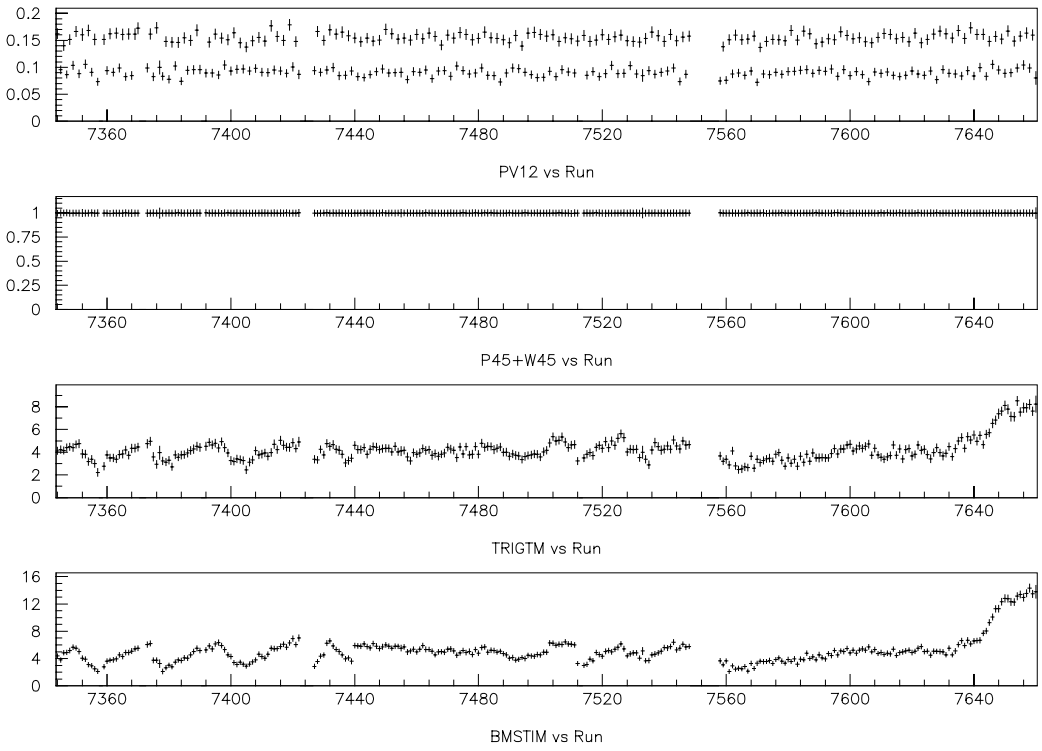

Figure 5.4:
The fraction of reconstructed trigger 2 events for the detectors PV12 and P45 and the average trigger and BMS TDC times (in units of 0.1 ns) versus run number.

As a further check on the time independence, the kinematical variables x_{Bj}, Q^2, the probability of finding a vertex and the probability of fitting the scattered muon's track are plotted versus run number. This is seen in figure 5.5 for trigger 1 and in figure 5.6 for trigger 2. Examples of problems are seen by the drop in the scattered muon fit probability for both triggers (near run number 7640) and by the slight drop in the vertex fit probabilities for trigger 2 in figure 5.6 (again near run number 7640).

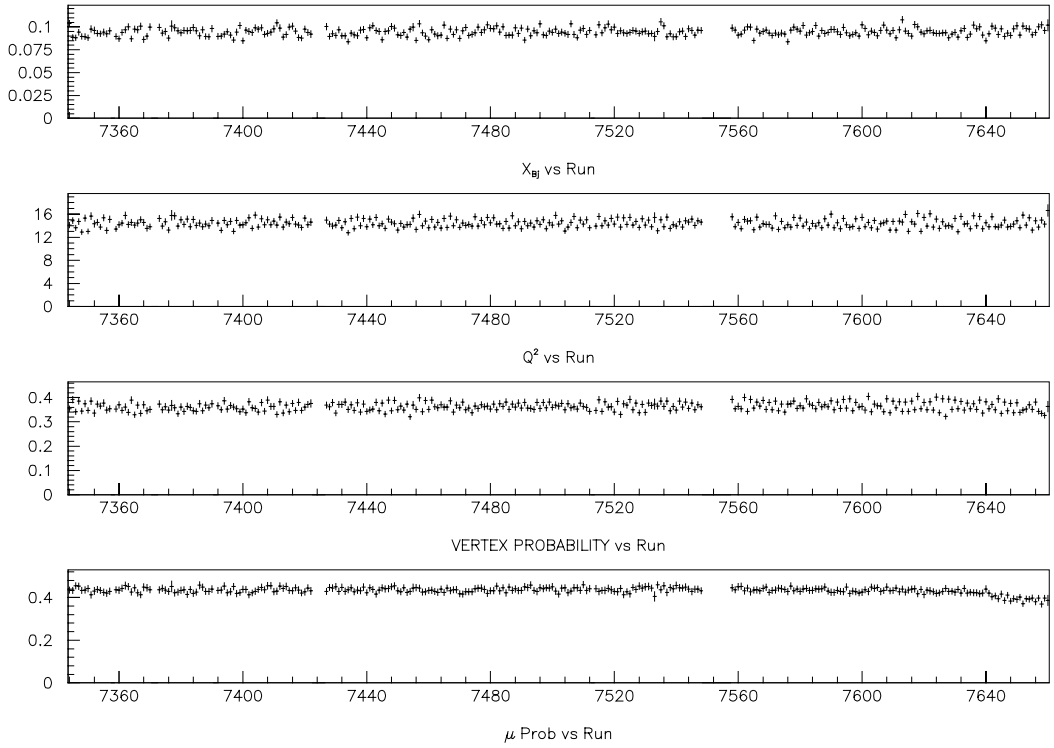

Figure 5.5:
The average value of x_{Bj}, Q^2, the vertex probability and the muon probability versus run number for trigger 1.

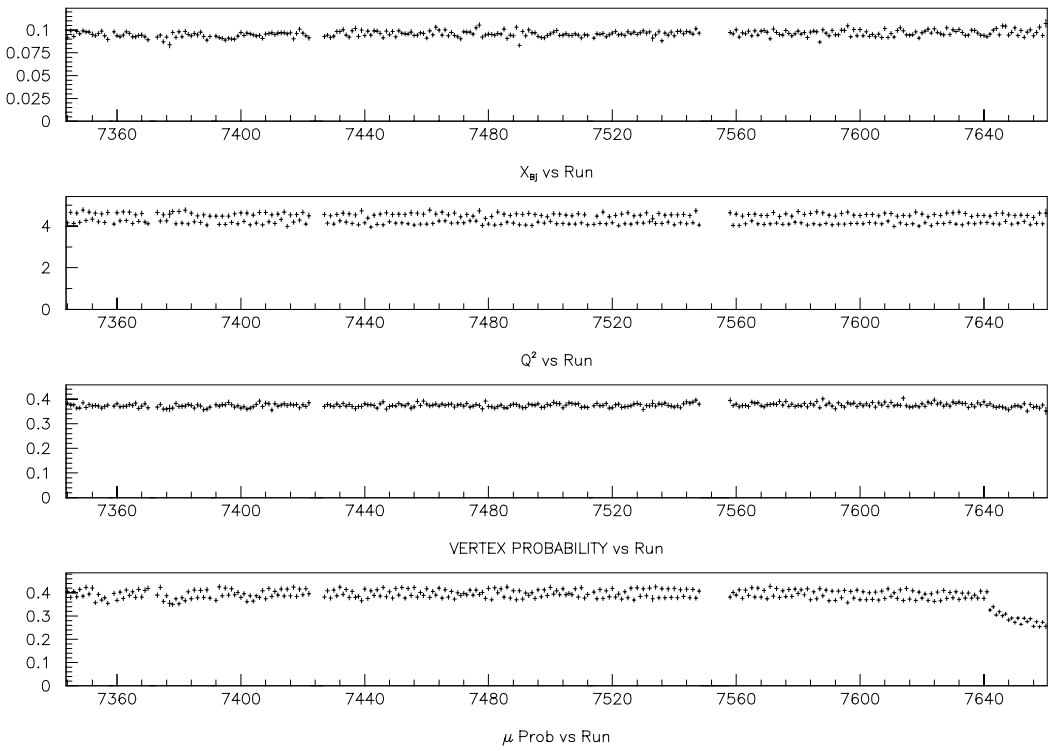

Figure 5.6:
The average value of x_{Bj}, Q^2, the vertex probability and the muon probability versus run number for trigger 2.

As in figures 5.3 and 5.4, the difference between the acceptance of the upstream and downstream targets is reflected by the alternating value of Q^2. However the drop in the scattered muon fit and vertex fit probabilities, along with a jump in the average time from the trigger time and the BMS TDC's indicates trouble. While these changes are not fully understood the causes include a change in the intensity of the beam and a sudden change in the temperature of the experimental hall. Since the significant deviations that are observed in these plots may effect the validity of the assumptions that were made in

calculation the cross section ratio, these runs must be considered unreliable. Therefore the last 20 runs were not used in the data analysis.

5.3.2. Determination of the Cuts

The first selection of the data that must be made is the vertex cut. This allows a given event to be ascribed to the target where the interaction took place. The next sets of cuts are on the kinematical variables.

5.3.2.1. Vertex Cuts

To determine the numbers of interactions occurring in each part of the target set vertex cuts are needed because there is some smearing of the **x**-position of the vertex. Given the spectrometer's good resolution of the vertices for the hydrogen and deuterium targets and the separation of the targets, the effect of the smearing is small. These cuts were defined in a way that minimized the number of events that could be mistakenly assigned to a target and at the same time maximized the number of events that are correctly assigned to a target. In figure 5.7 the number of events of the fitted vertex for trigger 1 is plotted versus the **x**-position along the beam path for the two target setups. The events of both target setups are added. The figure shows the almost linear dependence of the acceptance on the **x**-position. A similar plot for trigger 2 is shown in figure 5.8. The positions of the target vessels, the mylar windows, the beam hodoscopes, BHB, and of the proportional chambers, P0H and P0C are shown. While P0B is not labeled (for clarity), it is clearly seen between the upstream and downstream targets. The position of the final cuts is also indicated on these plots. The cuts were placed in the minima of the distributions on either side of the target vessels' end caps positions and between the targets and 'obstacles' in the beam (where the interactions from outside the

targets occurred), specifically the proportional chambers and the beam hodoscopes marked in the figures. The correction applied to the σ_d/σ_p ratio for the erroneous assignment of the vertex is detailed below.

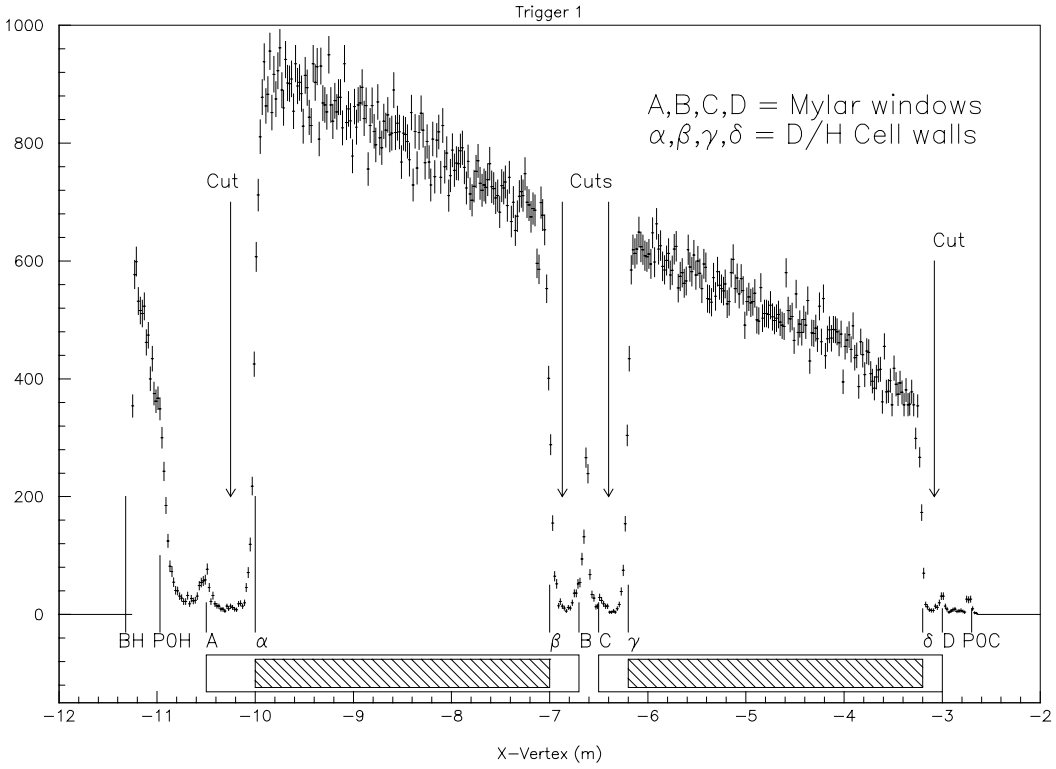

Figure 5.7:
The Vertex Distribution for trigger 1.
The number of events versus the **x**-position.

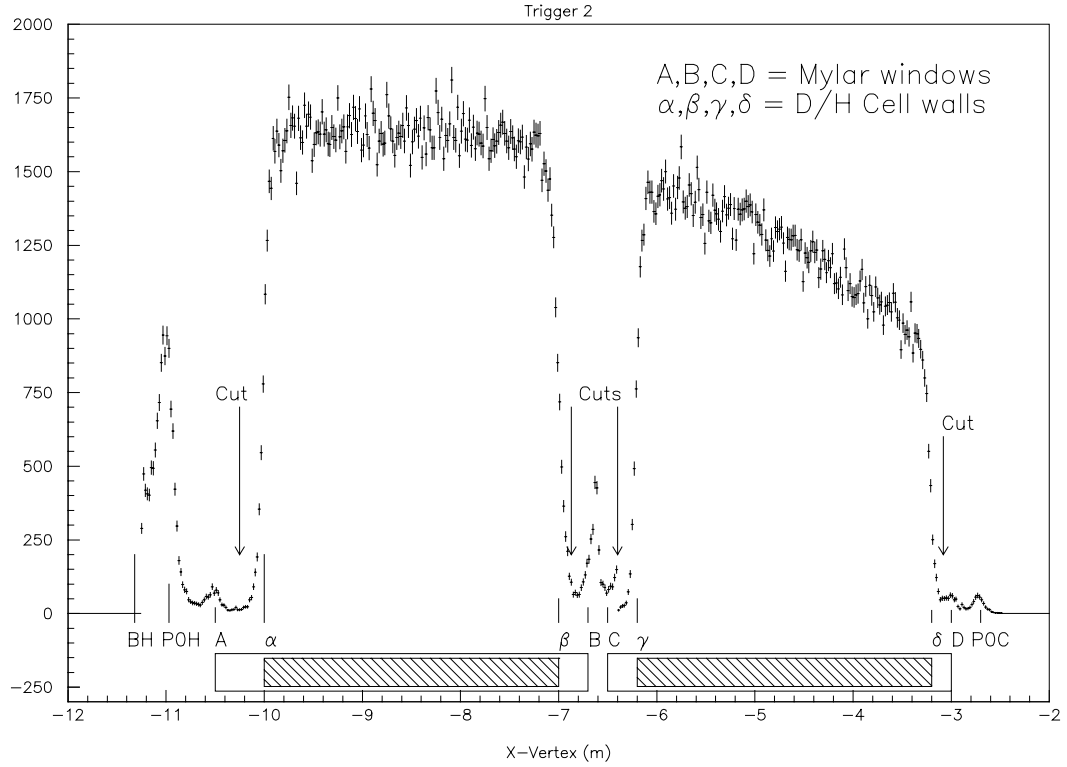

Figure 5.8:
The Vertex Distribution for trigger 2.
The number of events versus the **x**-position.

5.3.2.2. Kinematical cuts

The formulae in eqs. (5.1) and (5.4) can be manipulated to give the acceptance and flux ratios. The acceptance ratio is discussed above with the derivation of eq. (5.9), while now the flux ratio is defined as:

$$\frac{\phi_1}{\phi_2} = \sqrt{\frac{N_d^{up} N_p^{dn}}{N_p^{up} N_d^{dn}}}. \qquad (5.10)$$

Here ϕ_1 is the beam flux in target setup-1, ϕ_2 is the beam flux in target setup-2. Eq. (5.10) is based on the assumptions that the cross section for each material is independent of target position, and that the acceptance is independent of target material and thus is the same for each of the upstream and downstream targets, (thus $A_d^{up} = A_p^{up} = A^{up}$ and $A_p^{dn} = A_d^{dn} = A^{dn}$).

The flux ratio should be constant over the entire range of any kinematical variable. The acceptance ratio may vary due to the different acceptance between the upstream and downstream targets; however, regions where this ratio is rapidly varying should be cut out. The cuts are made such that any smearing of a kinematic variable does not cause sudden changes in the F_2^n/F_2^p ratio due to either flux or acceptance. After making these cuts, the correction from the "kinematic smearing" is small enough to be neglected entirely. Examples of the flux and acceptance ratios, before and after cuts, are given in figures 5.9 and 5.10 for trigger 1 and in figures 5.11 and 5.12 for trigger 2. Because the variables y and ν are correlated the cuts on low ν and high y are seen in both of the plots of ν and y. The cuts on θ and $\mathbf{p}'_\mu$ are determined from other arguments, but the necessity of the cuts is also seen in the flux and acceptance ratios.

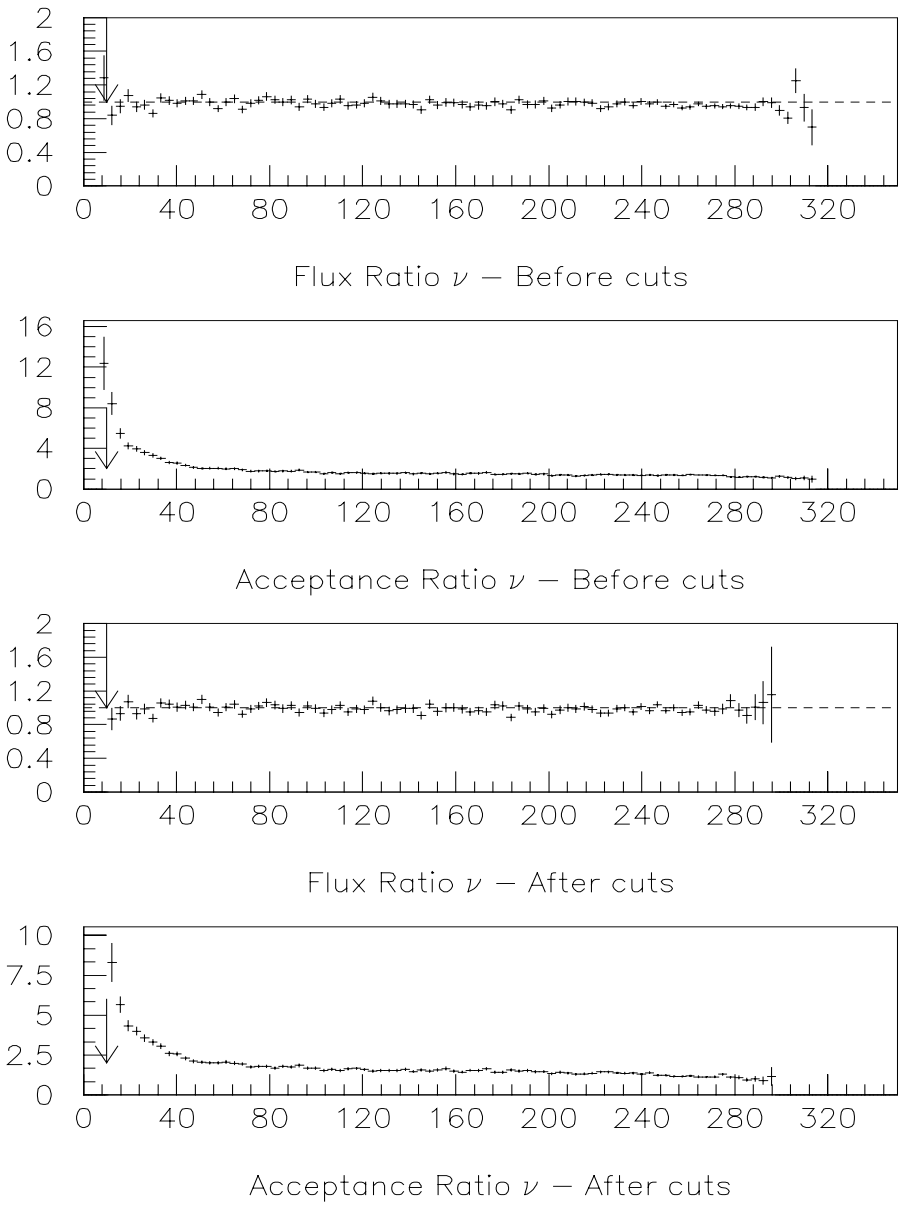

Figure 5.9:
The trigger 1 flux and acceptance ratios for ν, both before and after cuts, with the cuts shown by the arrows.

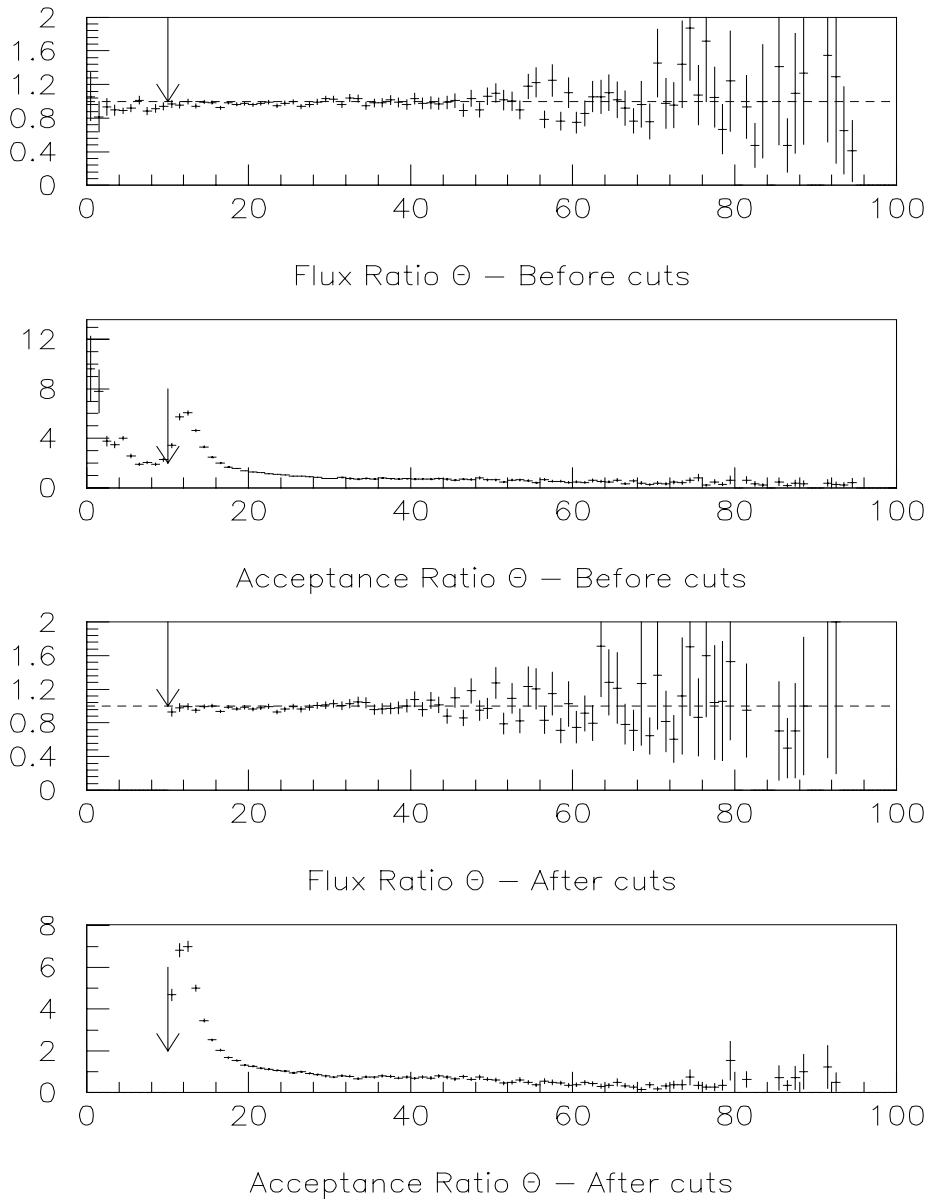

Figure 5.10:
The trigger 1 flux and acceptance ratios for θ, both before and after cuts, with the cuts shown by the arrows.

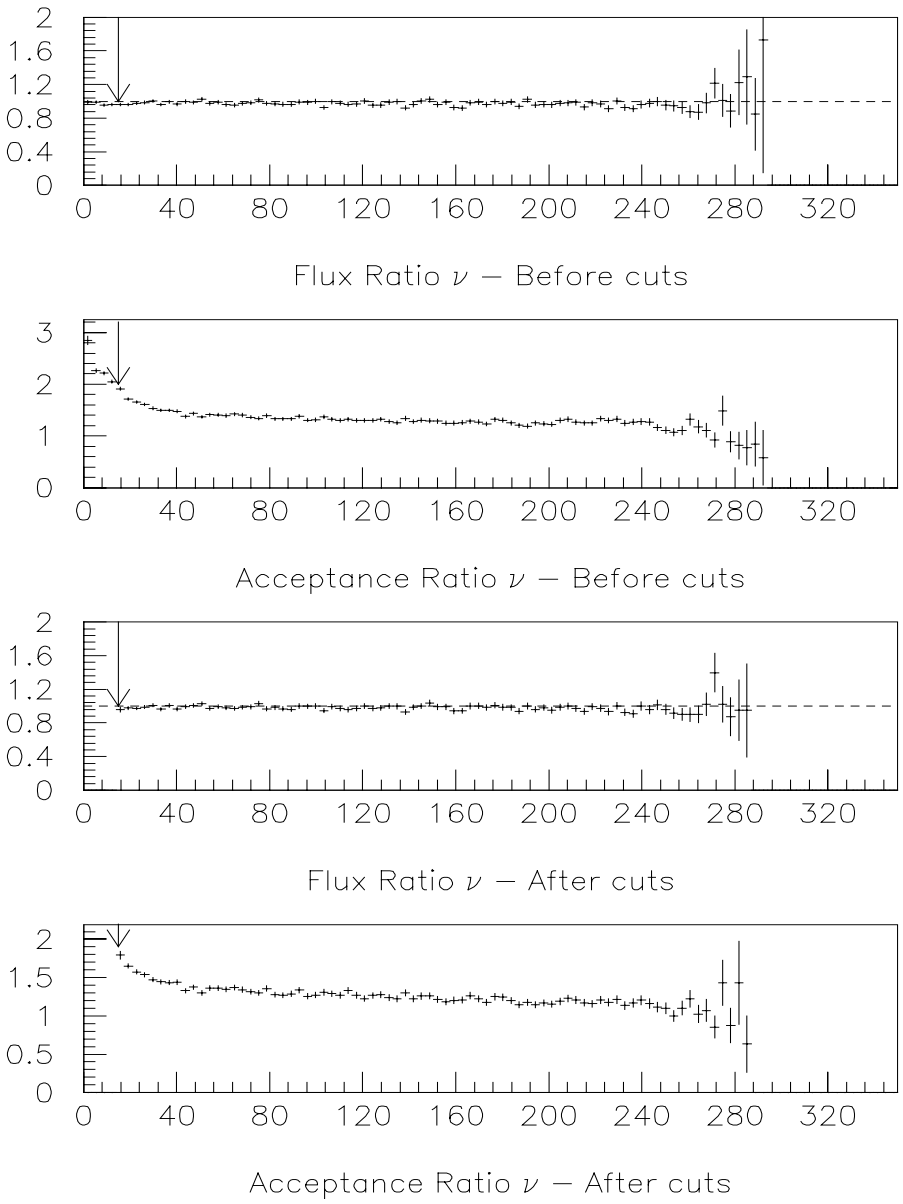

Figure 5.11:
The trigger 2 flux and acceptance ratios for ν, both before and after cuts, with the cuts shown by the arrows.

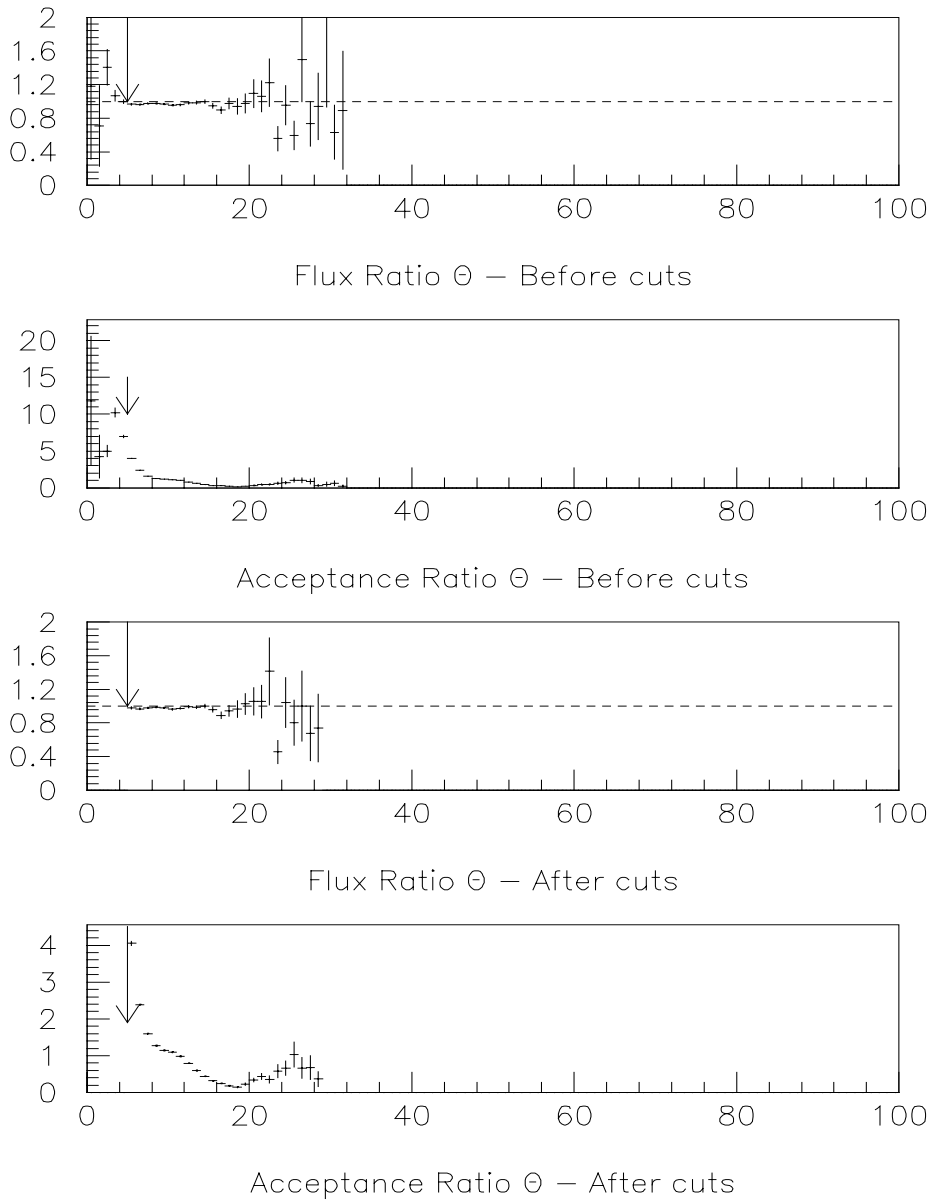

Figure 5.12:
The trigger 2 flux and acceptance ratios for θ, both before and after cuts, with the cuts shown by the arrows.

The final kinematical cuts are determined not only from the flux and acceptance ratio plots. There are also other arguments that are taken into consideration to remove problematic regions, i.e., those with large radiative corrections (the cut on high y), with poor x_{Bj} determination (the cut on low ν), and where there is contamination from hadronic decays (the cut on small values of the scattered muon momentum, $\mathbf{p}'_{\mu}$). Also cuts were made on the minimum scattering angle, θ, due to the limit of the trigger acceptance. The final cuts for the kinematic range $0.002 < x_{Bj} < 1,\ Q^2 > 1.0\ (\mathrm{GeV/c})^2$ for trigger 1 and $0.002 < x_{Bj} < 1,\ Q^2 > 0.5\ (\mathrm{GeV/c})^2$ for trigger 2 are shown in Table 5.1:

Table 5.1:
Cuts on the Kinematical Variables

Variable	Trigger 1	Trigger 2	Reason
y	< 0.9	< 0.9	Radiative Corrections
ν	> 10 GeV	> 15 GeV	Flux Ratio
$\mathbf{p}'_{\mu}$	> 30 GeV/c	> 30 GeV/c	Hadronic Contamination
θ	> 10 mrad	> 5 mrad	Trigger Acceptance

The assumptions that were made to allow eq. (5.8) to be used, i.e., on the flux and the acceptance, are thus shown to be valid in the region covered by the F_2^n/F_2^p ratio after making these cuts in the kinematic variables: x_{Bj}, Q^2, ν, y, $\mathbf{p}'_{\mu}$ and θ.

5.4. Corrections to the Ratio

The further corrections to be made before the ratio F_2^n/F_2^p can be extracted are the HD contamination of the liquid deuterium target and for the vertex resolution.

5.4.1. Effect of the HD contamination of the target.

The correction for the hydrogen-deuterium (HD) contamination of the liquid deuterium is done in two parts: first with a correction to the molar volume, $V_{D_2}^{mol}$, and second with a correction to the number of events, N_d. This calculation is done in full in appendix 8.2. The formula for the final correction is given by:

$$\left[\frac{\sigma_d}{\sigma_p}\right]_{corr} = \kappa\sqrt{\frac{N_d^{up}N_d^{down}}{N_p^{up}N_p^{down}}}\frac{\left(1+2\alpha\left(\delta-1\right)\right)}{\left(1+\alpha\left(\frac{\sigma_p}{\sigma_d}-1\right)\right)}. \tag{5.11}$$

With κ=0.8664, α=0.0151 and δ=1.1009 and by assuming that σ_p/σ_d is given by:

$$\frac{\sigma_p}{\sigma_d} = \left(\kappa\sqrt{\frac{N_d^{up}N_d^{down}}{N_p^{up}N_p^{down}}}\right)^{-1}. \tag{5.12}$$

A Taylor's expansion of the corrected ratio σ_d/σ_p is made; this gives to a good approximation:

$$\left[\frac{\sigma_d}{\sigma_p}\right]_{corr} \approx 0.8822\sqrt{\frac{N_d^{up}N_d^{down}}{N_p^{up}N_p^{down}}} - 0.0151. \tag{5.13}$$

5.4.2. Vertex resolution corrections

Because the cuts that are made on the **x**-vertex position in order to resolve the two targets do, due to smearing, cut out some good events and accept some bad events a correction to the ratio σ_d/σ_p must be made. After making a fit[1] to the number of events versus the **x**-position of the vertex, as seen in the examples given in figure 5.13 for trigger 1 and figure 5.14 for trigger 2, a correction is made. From the figures the contributions

from: the targets themselves, the beam hodoscope BHB, and the proportional chambers P0H and P0B, are visible. Since the vertex resolution depends on the scattering angle, θ, the fits were done for different θ bins.

The fits are made to each of the two target sets using a combination of a fit to trapezoidal shape, for the relatively straight parts, a convolution of a Gaussian function and Breit-Wigner function, for the edges of the targets and a Gaussian function for the proportional chambers, Mylar windows and the beam hodoscope.

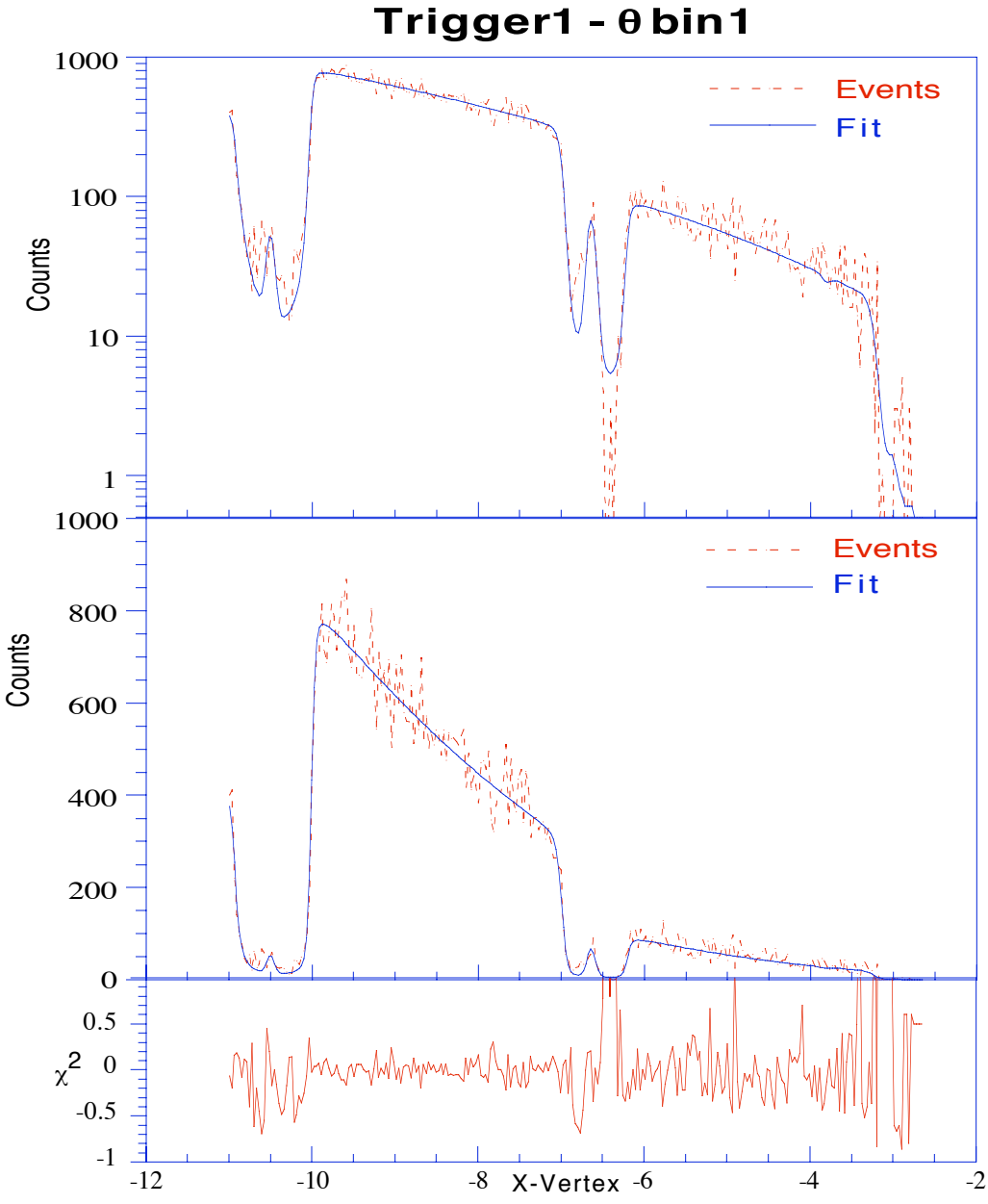

Figure 5.13:
The fit of the vertex smearing correction versus **x**-position for the first θ bin of trigger 1.

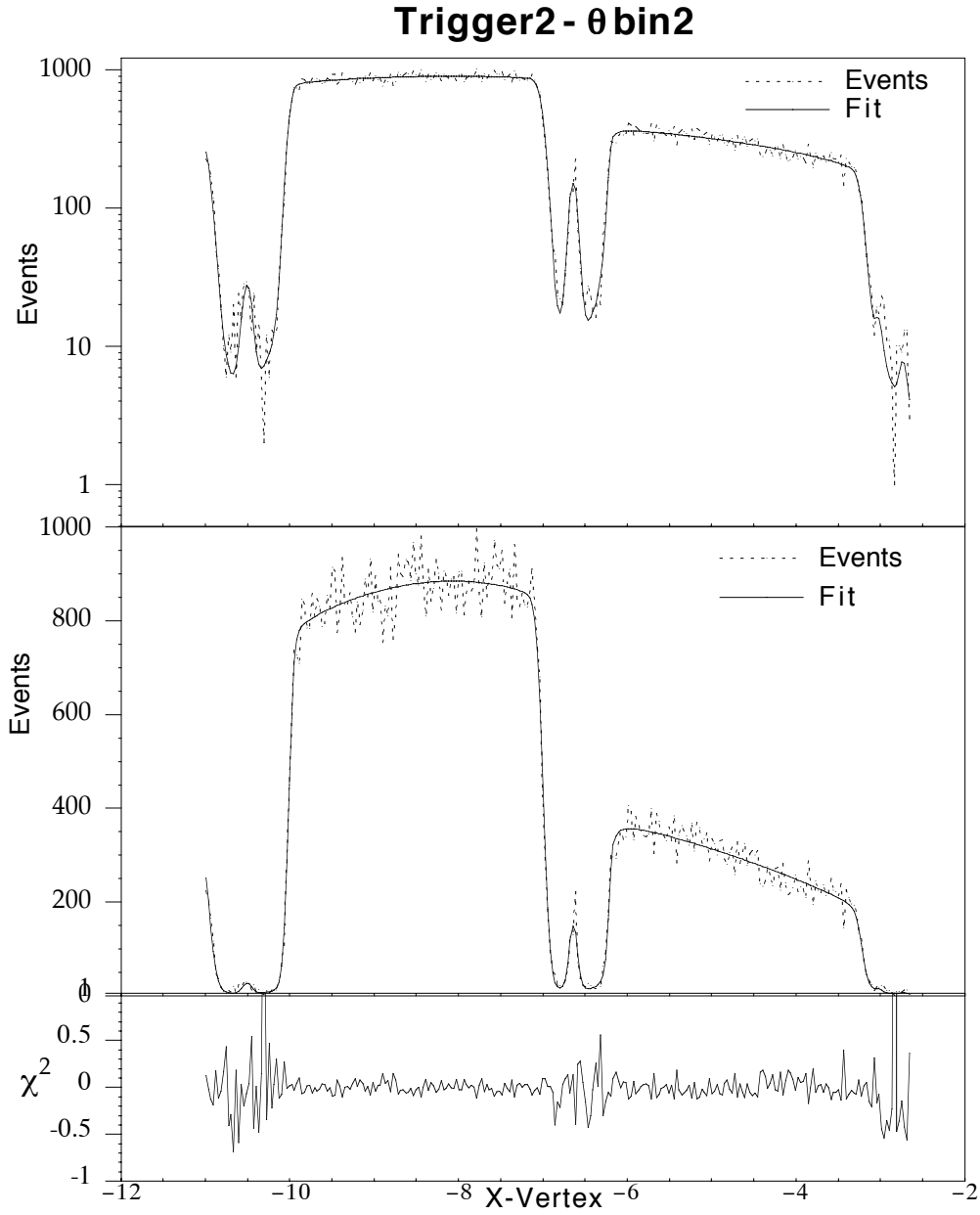

Figure 5.14:
The fit of the vertex smearing correction versus **x**-position for the second θ bin of trigger 2.

The corrections for the vertex smearing are determined by making a correction, γ, for each target position. This correction γ is the ratio of all events within the vertex cuts to all events that belong to that target, hence $\gamma = S/I$, where S is the sum of *all* fitted contributions within the vertex cuts and I is the fitted integral from -∞ to +∞ of the target contribution alone. The ratio, σ_d/σ_p, assumes the true number of events and $N_{measured} = \gamma\, N_{true}$, and since σ_d/σ_p is of the form:

$$\frac{\sigma_d}{\sigma_p} = \kappa \sqrt{\frac{N_d^{up} N_d^{dn}}{N_p^{up} N_p^{dn}}}, \tag{5.14}$$

the corrected σ_d/σ_p ratio is equal to α times the measured ratio, where α is defined from the ratio of $N_{measured} / N_{true}$ for each target position as:

$$\alpha = \sqrt{\frac{\gamma_p^{up} \gamma_p^{dn}}{\gamma_d^{up} \gamma_d^{dn}}}. \tag{5.15}$$

In the worst case this correction is less then 1 percent and is typically two or three parts per mil, the same order as the systematic error. The accuracy of this correction is less then one part per mil and typically a few parts per ten thousand. The correction factor α, with errors, for the appropriate θ bins, is given in table 5.2.

Table 5.2: Correction factor α, for the given θ bins:

Trigger 1	0.010<θ<0.015	0.015<θ<0.019	0.019<θ<0.025	0.025<θ<0.100
	1.0073±0.0009	1.0039±0.0001	1.0036±0.0004	1.0023±0.0001
Trigger 2	0.005<θ<0.007	0.007<θ<0.009	0.009<θ<0.011	0.011<θ<0.100
	1.0042±0.0004	1.0035±0.0001	1.0019±0.0001	1.0015±0.0001

5.5. Results of the ratio analysis

The results of the ratio analysis are presented in three parts: the x_{Bj} dependence of the ratio, the Q^2 dependence of the ratio and the test of the Gottfried sum rule.

5.5.1. The x_{Bj} dependence of the ratio F_2^n/F_2^p

At low x_{Bj} shadowing may be observed in the F_2^n/F_2^p ratio for deep inelastic scattering. The ratio F_2^n/F_2^p has been used to put constraints on the parton distribution parametrizations by extending the range in x_{Bj} to the region $0.01 < x_{Bj} < 0.10$, where the valence and sea quarks contribute equally. In the region x_{Bj}>0.3 the valence quarks dominate because they are now carrying a significant fraction of the nucleon momentum.

The ratio F_2^n/F_2^p has also been used to constrain the standard model prediction to the $W^{\pm}$ and Z^0 production cross section ratio σ_W/σ_Z and to deduce the number of neutrino families[2]. The ratio σ_W/σ_Z is related to the up to down quark ratio d/u. As discussed in section 2.2, the ratio d/u can be expressed in terms of the ratio F_2^n/F_2^p; therefore, the ratio σ_W/σ_Z is related (in the quark-parton model) to the ratio F_2^n/F_2^p. By comparing the $W^{\pm}/Z^0$ decay, which depends on N_ν, the number of neutrino families, as calculated from the quark-parton model, in which F_2^n/F_2^p was input, with the measured value in $\bar{p}p$ collisions, one finds N_ν=3±1 prior to the much more precise value now known from Large Electron-Positron collider (LEP). At $\sqrt{s} = 630$ GeV, which corresponds to $x_{Bj} = 0.14$, the ratio σ_W/σ_Z was calculated to be 3.35±0.04.

In figure 5.15 the ratio of the number of $W^{\pm}$s to the number of Z^0s versus the number of possible neutrino families from data prior to the start of LEP.

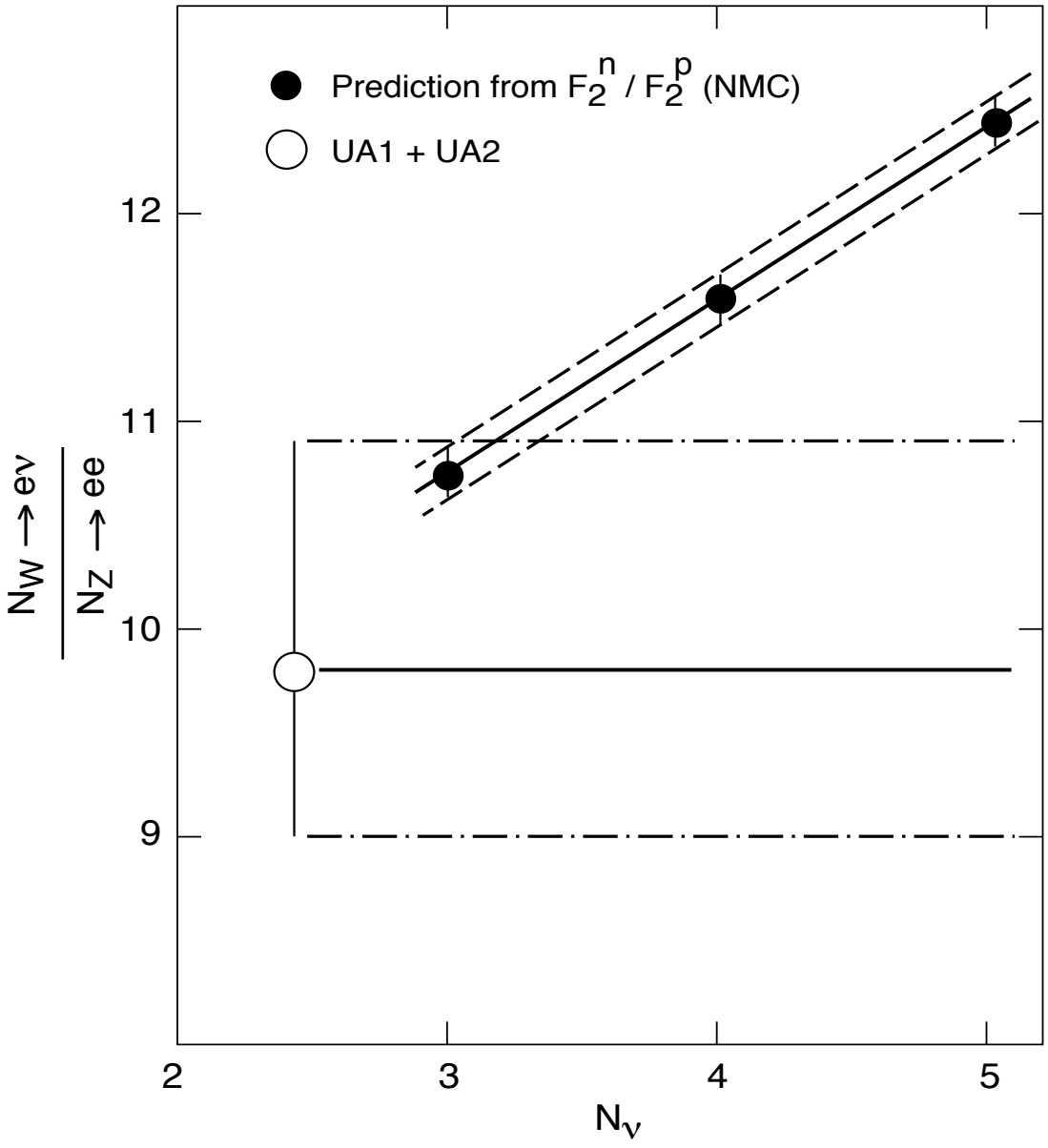

Figure 5.15:
The ratio of the number of $W^{\pm}$s to the number of Z^0s versus the number of possible neutrino flavors.

The x_{Bj} dependence of the ratio F_2^n/F_2^p was obtained by averaging the results over Q^2 for each x_{Bj} bin. The results from period P3A89 at 280 GeV for both trigger 1

and trigger 2 are given in table 5.3 and plotted in figure 5.16. Since there is generally good agreement between the results for trigger 1 and 2 the data could be combined.

Table 5.3: The ratio F_2^n/F_2^p averaged over Q^2 for P3A89

x_{Bj}	Trigger 1			Trigger 2		
	$\langle Q^2 \rangle$ $(\mathrm{GeV/c})^2$	$\frac{F_2^n}{F_2^p}(x_{Bj})$	Error (statistical)	$\langle Q^2 \rangle$ $(\mathrm{GeV/c})^2$	$\frac{F_2^n}{F_2^p}(x_{Bj})$	Error (statistical)
0.003	1.4	1.124	0.072	1.1	0.956	0.030
0.007	2.9	0.962	0.031	2.1	0.944	0.016
0.015	5.8	0.974	0.028	3.2	0.938	0.015
0.030	10.0	0.942	0.025	4.2	0.945	0.015
0.050	14.4	0.950	0.030	5.1	0.903	0.019
0.080	18.7	0.831	0.024	5.8	0.862	0.017
0.125	23.2	0.862	0.028	7.1	0.842	0.021
0.175	26.4	0.826	0.033	8.7	0.748	0.028
0.250	29.0	0.711	0.028	10.7	0.744	0.032
0.350	31.0	0.586	0.035	13.4	0.739	0.062
0.450	31.5	0.466	0.044	16.1	0.522	0.104
0.550	31.5	0.412	0.060			
0.700	30.6	0.512	0.077			
0.900	27.7	0.643	0.194			

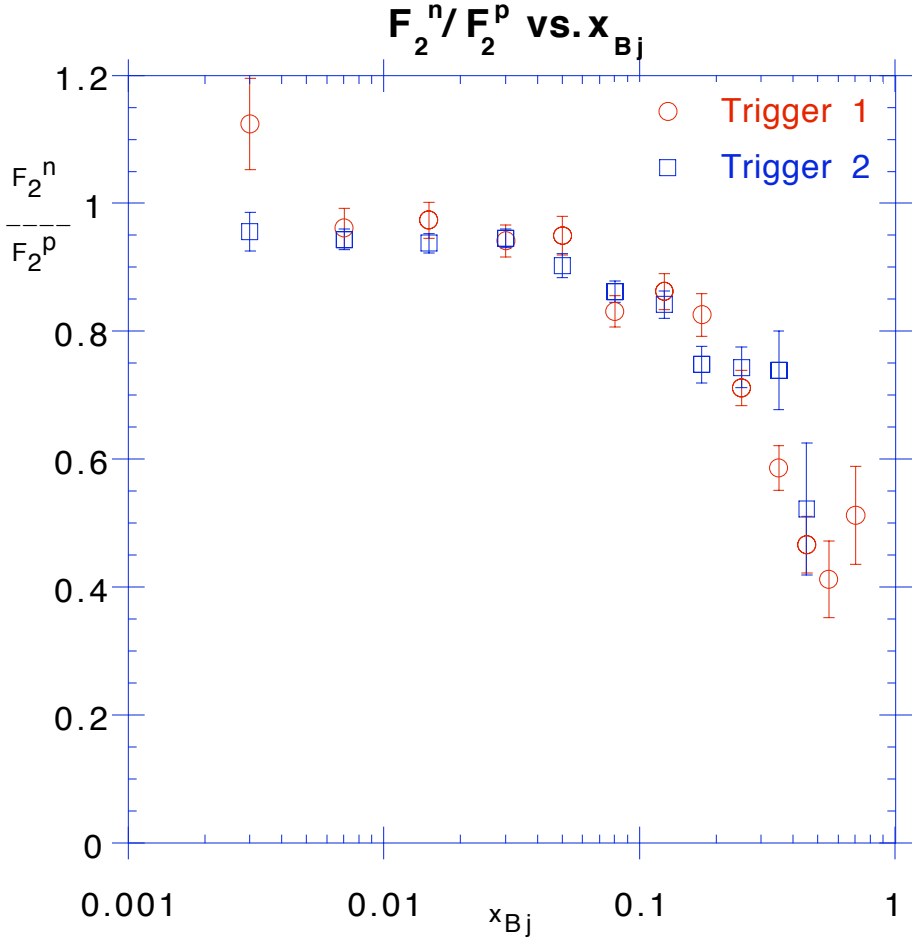

Figure 5.16:
The ratio F_2^n/F_2^p for trigger 1 and trigger 2 versus x_{Bj}.

The combined trigger 1 and trigger 2 results, along with the total systematic errors from the latest NMC ratio paper[3] are given in table 5.4. The systematic errors are from primarily three sources: the radiative corrections, the uncertainty in the momentum of the incoming and of the scattered muon and the vertex resolution. Because one of the sources of error in the radiative corrections is the uncertainty in F_2^d, the error on the radiative corrections for the 1989 data should be less then the error quoted in the NMC paper[3], due

to the present better knowledge of F_2^d. The error in the momentum uncertainty is the same in 1989 as previously[3]. Also the vertex resolution corrections are of the same size as before. The total systematic errors were obtained by adding each individual source in quadrature.

These results are also shown in figure 5.17 with statistical errors only together with the latest combined NMC ratio results[4].

Table 5.4:
The ratio F_2^n/F_2^p averaged over Q^2 for trigger 1 and trigger 2 combined

x_{Bj}	$\langle Q^2 \rangle$ in $(\mathrm{GeV/c})^2$	$\frac{F_2^n}{F_2^p}(x_{Bj})$	Error (statistical)	Error (systematic)
0.003	1.16	0.981	0.028	0.022
0.007	2.24	0.948	0.014	0.012
0.015	3.78	0.946	0.014	0.007
0.030	5.71	0.944	0.013	0.005
0.050	7.61	0.916	0.016	0.004
0.080	9.93	0.852	0.014	0.003
0.125	12.92	0.849	0.017	0.003
0.175	16.24	0.781	0.022	0.004
0.250	21.19	0.725	0.021	0.004
0.350	26.74	0.623	0.030	0.006
0.450	29.13	0.475	0.041	0.008
0.550	30.03	0.380	0.056	0.012
0.700	29.68	0.441	0.073	0.017

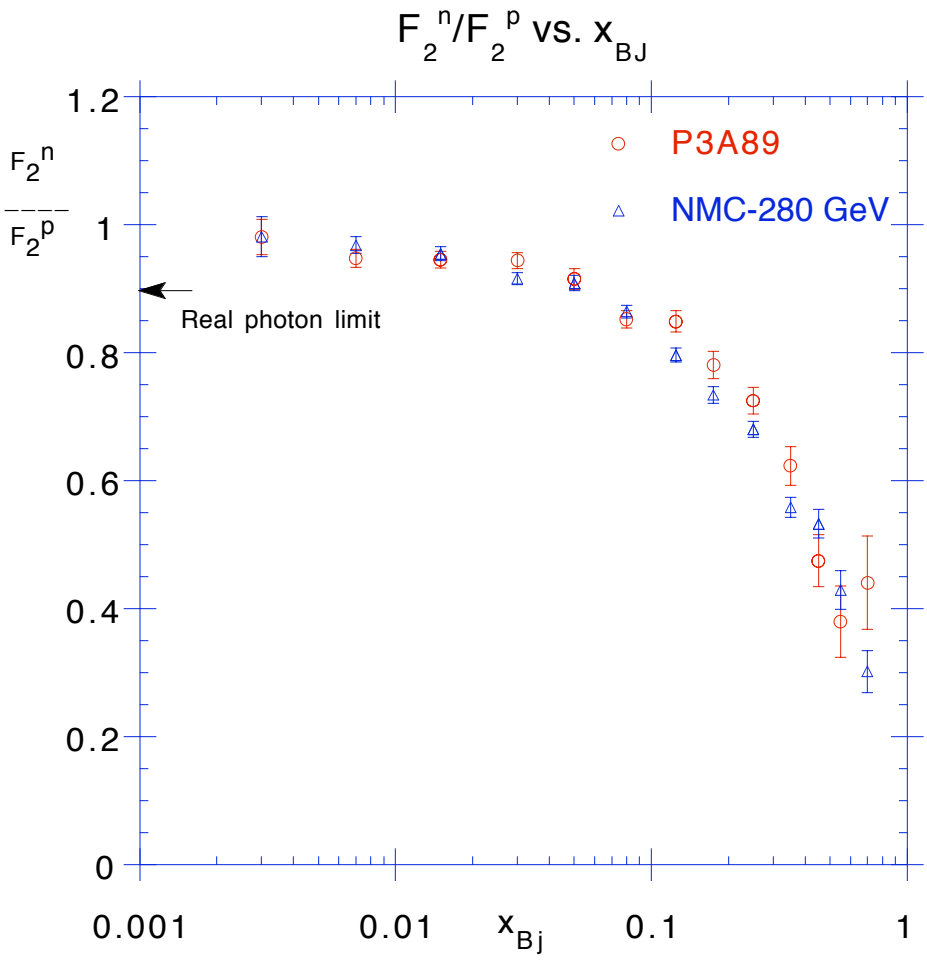

Figure 5.17:
The ratio F_2^n/F_2^p for the combination of both trigger 1 and 2 data, along with the NMC results for 280 GeV[4], versus x_{Bj}.

Since the ratio F_2^n/F_2^p, as seen in the plot is consistent with unity at low x_{Bj}, (0.981±0.028) there is no evidence of any sizable shadowing in deuterium, at least for $x_{Bj} \geq 0.003$, which would be seen in a suppression of the ratio to low x_{Bj}.

In the region x_{Bj}>0.3, the valence quarks dominate, therefore the structure function ratios should, as discussed in section 2.2, reduce to:

$$\frac{F_2^n}{F_2^p}(x_{Bj}) = \left[1 + 4\frac{d_v(x_{Bj})}{u_v(x_{Bj})}\right] \Big/ \left[4 + \frac{d_v(x_{Bj})}{u_v(x_{Bj})}\right]. \tag{5.16}$$

In this region there is good agreement between the neutrino data and the NMC muon data. In figure 5.18 the ratio F_2^n/F_2^p for muons and the ratio as expressed by equation 5.16 for neutrinos is plotted versus x_{Bj}.

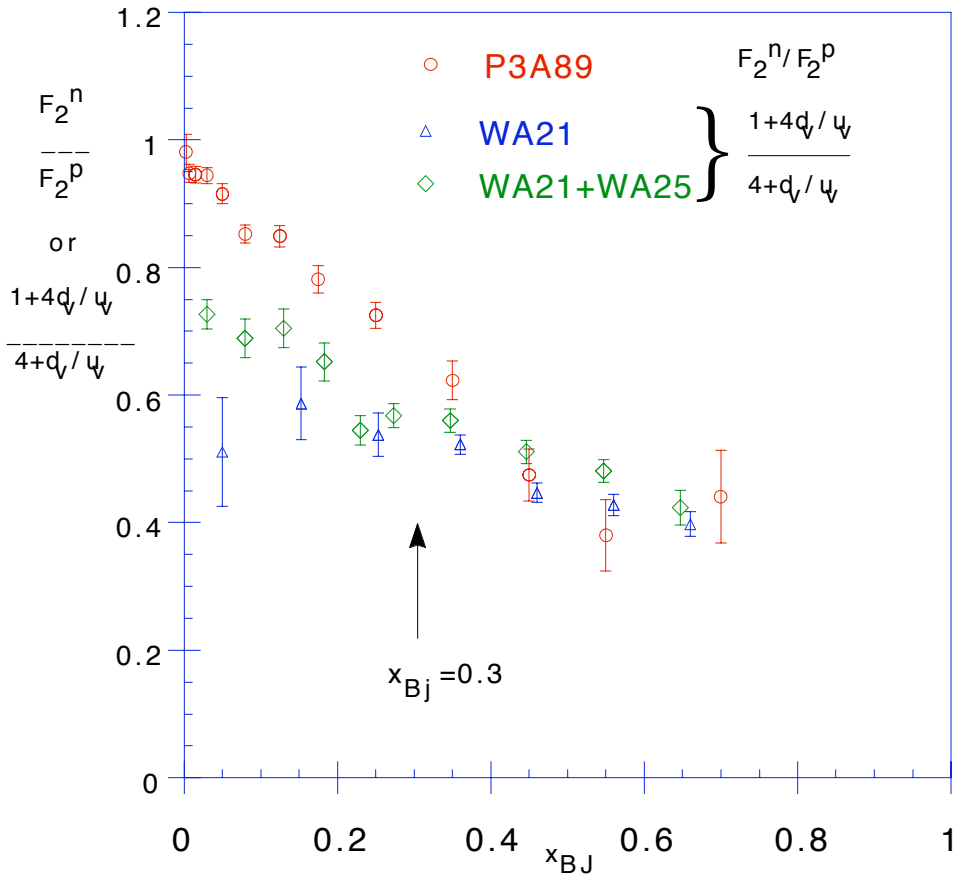

Figure 5.18:
A comparison of the ratio F_2^n/F_2^p for muons with neutrinos from the CERN WA21 and WA25 experiments[5] versus x_{Bj}.

5.5.2. The Q^2 dependence of the ratio F_2^n/F_2^p

It has been observed in previous NMC results[6] that there is a slight difference between the results of the ratio F_2^n/F_2^p measured for two different energies, 90 GeV and 280 GeV, in the medium x_{Bj} range. This implies that there is a slight Q^2 dependence. The Q^2 dependence of the present data was therefore also studied.

The results of the 280 GeV period, P3A89, are presented in table 5.5, where the systematic errors are again taken from the latest NMC ratio paper[3], as discussed in chapter 5.6.1. These results are plotted in figure 5.19, with statistical errors only, along with a fit to the previous NMC data of both 90 GeV and 280 GeV versus Q^2 for each x_{Bj}-bin. The results of P3A89 are consistent with the fit.

The fit was obtained in the following manner, for each x_{Bj}-bin, the assumption of a linear function in $\ln\left(Q^2\right)$ was made and is given as:

$$\frac{F_2^n}{F_2^p}\left(x_{Bj}^i, Q^2\right) = a\left(x_{Bj}^i\right) + b\left(x_{Bj}^i\right)\ln\left(Q^2\right). \tag{5.17}$$

The full analysis of the Q^2 dependence of the ratio F_2^n/F_2^p, along with higher order QCD effects, has been presented elsewhere[6]. The results presented in this thesis are in good agreement with previous NMC results[6]. Therefore the conclusions drawn from those results regarding the Q^2 dependence and higher order QCD effects should hold true for the data in this thesis.

Table 5.5: The ratio $\frac{F_2^n}{F_2^p}(x_{Bj},Q^2)$ for P3A89. (Q^2 in $(\text{Gev/c})^2$)

Q^2	$\frac{F_2^n}{F_2^p}(x_{Bj},Q^2)$	Stat. error	Syst. error
At x_{Bj}=0.003			
0.75	1.0230	0.05596	0.025
1.5	0.9630	0.03202	0.020
At x_{Bj}=0.007			
1.5	0.9666	0.02296	0.010
2.5	0.9273	0.02235	0.013
3.5	0.9299	0.03726	0.014
4.5	1.1280	0.10730	0.015
At x_{Bj}=0.015			
1.5	0.9485	0.05459	0.004
2.5	0.9729	0.02659	0.004
3.5	0.9390	0.02750	0.005
4.5	0.9152	0.03117	0.009
5.5	0.9041	0.04081	0.010
7.0	0.9526	0.04514	0.010
9.0	1.0640	0.13800	0.010
At x_{Bj}=0.030			
1.5	0.8709	0.08534	0.020
2.5	0.9117	0.03334	0.012
3.5	0.9368	0.02990	0.012
4.5	0.9748	0.03383	0.002
5.5	0.9330	0.03819	0.024
7.0	1.0150	0.03606	0.025
9.0	0.9515	0.04098	0.005
11.5	0.8970	0.04250	0.023
15.0	0.9164	0.06941	0.016
At x_{Bj}=0.050			
1.5	0.9385	0.15950	0.006
2.5	0.9201	0.05191	0.004
3.5	0.9062	0.04298	0.003
4.5	0.9105	0.04534	0.003
5.5	0.9411	0.05129	0.003
7.0	0.9216	0.04359	0.003
9.0	0.7423	0.05112	0.006
11.5	0.9553	0.05607	0.003
15.0	0.9526	0.05167	0.003
20.0	1.0190	0.06493	0.004
27.0	0.8478	0.16810	0.005
At x_{Bj}=0.080			
2.5	0.9462	0.05877	0.010
3.5	0.8938	0.04126	0.008
4.5	0.8329	0.04107	0.027
5.5	0.8381	0.04496	0.035
7.0	0.8276	0.03711	0.029
9.0	0.8012	0.04650	0.013
11.5	0.8196	0.04842	0.018
15.0	0.8825	0.04895	0.011
20.0	0.8261	0.04394	0.021
27.0	0.8422	0.05720	0.017
36.0	0.7593	0.10090	0.174

Table 5.5:(Continued) The ratio $\frac{F_2^n}{F_2^p}(x_{Bj},Q^2)$ for P3A89. (Q^2 in $(\text{Gev/c})^2$)

Q^2	$\frac{F_2^n}{F_2^p}(x_{Bj},Q^2)$	Stat. error	Syst. error
At x_{Bj}=0.125			
3.5	0.8500	0.06542	0.016
4.5	0.9195	0.05260	0.037
5.5	0.8413	0.05322	0.007
7.0	0.7914	0.04288	0.039
9.0	0.8380	0.05540	0.018
11.5	0.8252	0.05611	0.022
15.0	0.8790	0.05920	0.004
20.0	0.8305	0.05275	0.012
27.0	0.7966	0.05611	0.024
36.0	1.0170	0.08566	0.041
48.0	0.7050	0.10190	0.072
At x_{Bj}=0.175			
4.5	0.8863	0.13170	0.021
5.5	0.8154	0.07128	0.026
7.0	0.7300	0.05186	0.002
9.0	0.7422	0.06425	0.017
11.5	0.7247	0.06570	0.009
15.0	0.8664	0.07352	0.026
20.0	0.8072	0.06497	0.024
27.0	0.7135	0.06415	0.036
36.0	0.8880	0.08709	0.022
48.0	0.8799	0.11340	0.021
65.0	0.9333	0.17780	0.117

Q^2	$\frac{F_2^n}{F_2^p}(x_{Bj},Q^2)$	Stat. error	Syst. error
At x_{Bj}=0.250			
7.0	0.8062	0.07031	0.005
9.0	0.7475	0.06020	0.004
11.5	0.7043	0.05847	0.003
15.0	0.7624	0.06428	0.004
20.0	0.6798	0.05495	0.003
27.0	0.6410	0.05546	0.002
36.0	0.6625	0.06735	0.002
48.0	0.9070	0.09962	0.002
65.0	0.7342	0.11770	0.001
100.0	0.9024	0.20250	0.001
At x_{Bj}=0.350			
9.0	0.7397	0.17420	0.008
11.5	0.7518	0.08828	0.006
15.0	0.6773	0.08625	0.005
20.0	0.6832	0.08106	0.003
27.0	0.6073	0.07583	0.003
36.0	0.6499	0.08892	0.002
48.0	0.6618	0.11020	0.002
65.0	0.4658	0.11780	0.001
100.0	0.4865	0.15490	0.001
At x_{Bj}=0.450			
15.0	0.5549	0.10890	0.007
20.0	0.6557	0.11070	0.004
27.0	0.5421	0.10050	0.003
36.0	0.3041	0.09601	0.003
At x_{Bj}=0.550			
20.0	0.4177	0.12250	0.006
27.0	0.5179	0.13700	0.004
36.0	0.4355	0.15860	0.003

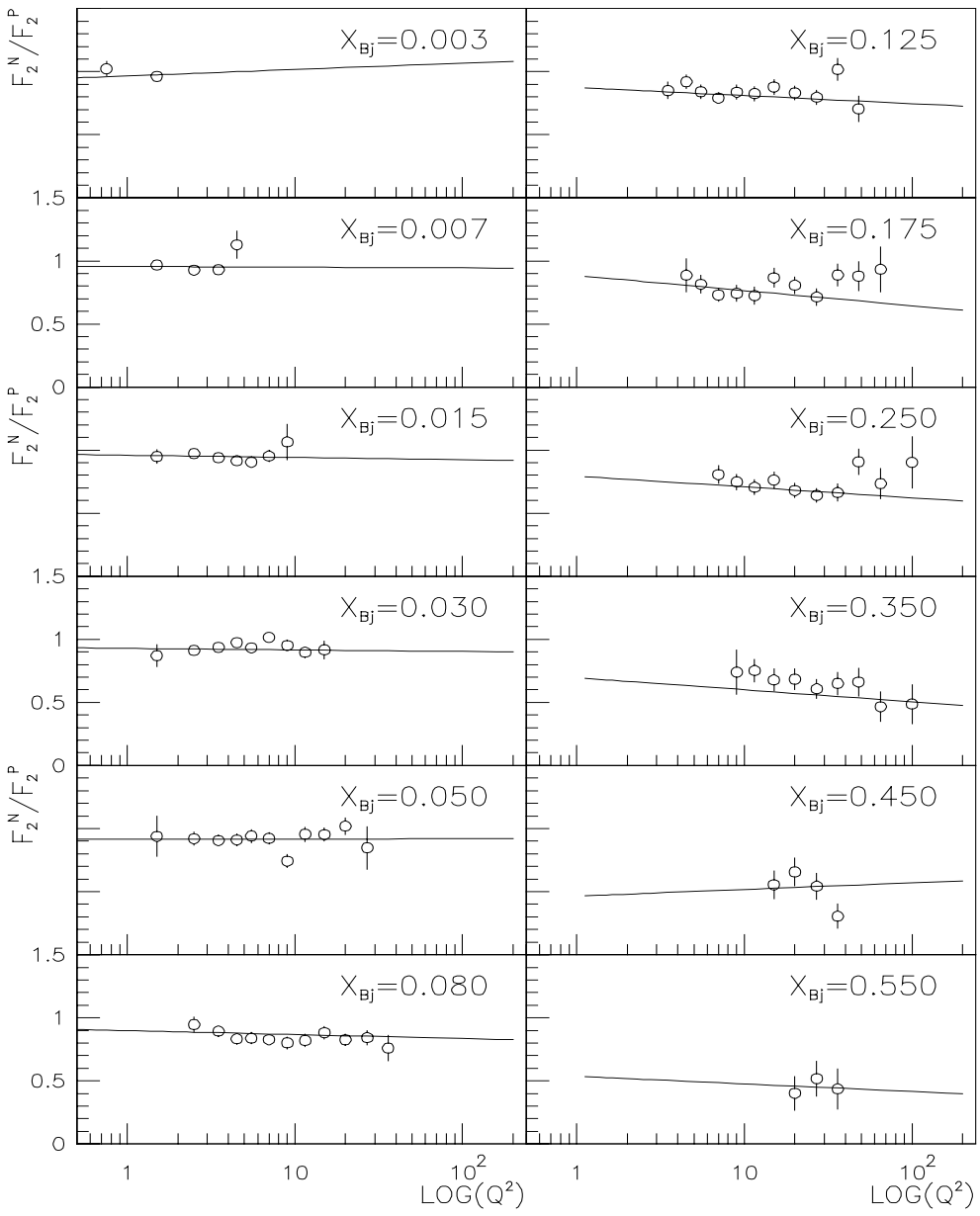

Figure 5.19:
The Q^2 dependence of the ratio F_2^n/F_2^p.

5.5.3. The measurement of $R^d - R^p$.

The structure function ratio F_2^n/F_2^p was derived, in section 5.3, from the cross section ratio $\sigma_d^{1\gamma}/\sigma_p^{1\gamma}$ by making the assumption that the ratio of the longitudinally to transversely polarized virtual photon absorption cross section R is the same for the deuteron as for the proton.

Experimental results on $\Delta R = R^d - R^p$ can be compared to perturbative QCD[7] computations predicting that the difference ΔR is much smaller then R if one assumes similar gluon distributions in the deuteron and proton. Inversely a large value of ΔR would indicate either a difference in the gluon distributions of the proton and deuteron or different higher-twist contributions to R^d and R^p.

Previously the values of $R^d - R^p$ were previously obtained from measurements by the BCDMS[8] collaboration and from a re-analysis of older SLAC data[9]. In the NMC experiment the cross section ratios were measured with minimal systematic errors. Because such ratios are much more sensitive to ΔR than to individual measurements of R^d and R^p, the data sets from this thesis and from earlier NMC results[3] are well suited to determine ΔR.

As detailed in a recent NMC paper[10], the calculation of ΔR involves using the cross section ratio $\sigma_d^{1\gamma}/\sigma_p^{1\gamma}$ measured at two or more different energies. The data presented in this thesis was measured only at one energy. Therefore one can only compare the results of the published calculation with the results of the calculation[11] that included both the data from 1989 and the previous NMC results[3]. The 1989 data include the data from two periods with a muon energy of 280 GeV (P2D89 and P3A89). The previous NMC results[3] include the data sets of 90 and 280 GeV beam energies.

The x_{Bj}-dependence of $R^d - R^p$, plotted with statistical errors only, for both of these sets of results is shown in figure 5.20.

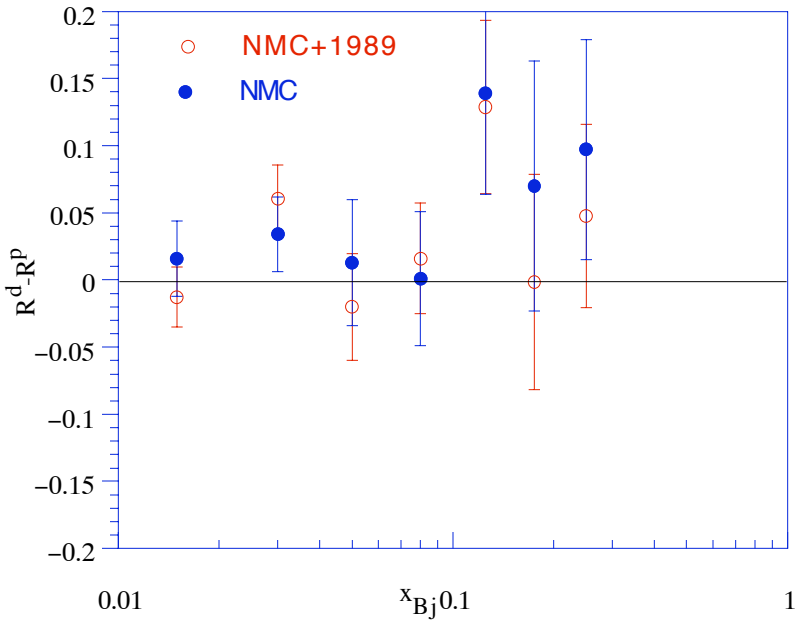

Figure 5.20:
The difference $R^d - R^p$ versus x_{Bj}.

The results presented in this thesis cover the kinematic range $0.01 < x_{Bj} < 0.3$. When averaged over x_{Bj}, the result for ΔR of the calculation that includes the 1989 data is: $0.022 \pm 0.011(\text{Stat.})$. This should be compared to the published result[10] of: $0.031 \pm 0.016(\text{Stat}) \pm 0.011(\text{Syst.})$ The previous SLAC[9] results in the range $0.1 < x_{Bj} < 0.9$ give a value for $R^d - R^p$ of: $-0.001 \pm 0.009(\text{Stat}) \pm 0.009(\text{Syst.})$. These results are consistent with zero and thus in good agreement with the QCD prediction[7].

5.5.4. Gottfried sum rule

The Gottfried Sum, as discussed in chapter 2.2 is the integral of the difference between the proton and neutron structure function in the form:

$$S_G = \int_0^1 \frac{d\,x_{Bj}}{x_{Bj}} \left(F_2^p\left(x_{Bj}\right) - F_2^n\left(x_{Bj}\right) \right). \tag{5.18}$$

Since the ratio F_2^n/F_2^p is measured, the difference $F_2^p - F_2^n$ can be determined from the ratio by using eq. (5.8). This difference, in terms of the ratio F_2^n/F_2^p and the structure function F_2^d is:

$$F_2^p\left(x_{Bj}\right) - F_2^n\left(x_{Bj}\right) = 2\,F_2^d\left(x_{Bj}\right) \frac{\left(1 - \dfrac{F_2^n}{F_2^p}\left(x_{Bj}\right)\right)}{\left(1 + \dfrac{F_2^n}{F_2^p}\left(x_{Bj}\right)\right)}. \tag{5.19}$$

The value of the structure function F_2^d is given by a parametrization in x_{Bj} and Q^2 from the latest published results[12]. The prediction for the Gottfried sum was made using the quark-parton model which has no scaling of the value of the structure function F_2. However there is scaling in the value of F_2, but the QCD corrections are small. To remove the small effect of these scaling violations the Gottfried sum is calculated at fixed values of Q^2. This means that the ratio F_2^n/F_2^p at $\langle Q^2 \rangle$ must be extrapolated. This was done using the Q^2 slopes as measured for the whole range of the previous NMC data[3]. The values for F_2^n/F_2^p, measured at an average Q^2 and given in table 5.4, are extrapolated to the fixed value of Q^2. The results in the measured range, $0.004 < x_{Bj} < 0.8$, for two different values of Q^2 are given in table 5.7.

Table 5.7:

F_2^d, F_2^n/F_2^p and the Gottfried Sum for different values of Q^2.

x_{Bj} bin	$Q^2 = 4.0\ (\text{Gev/c})^2$					$Q^2 = 7.0\ (\text{Gev/c})^2$				
	F_2^d	F_2^n/F_2^p	error	$\sum_G$	error	F_2^d	F_2^n/F_2^p	error	$\sum_G$	error
0.004 - 0.01	0.412	0.946	0.016	0.216	0.012	0.463	0.945	0.019	0.228	0.013
0.01 - 0.02	0.393	0.945	0.013	0.196	0.010	0.435	0.941	0.014	0.205	0.010
0.02 - 0.04	0.378	0.946	0.013	0.181	0.009	0.409	0.943	0.013	0.187	0.009
0.04 - 0.06	0.365	0.915	0.017	0.167	0.009	0.387	0.916	0.016	0.172	0.008
0.06 - 0.10	0.349	0.865	0.015	0.154	0.008	0.364	0.857	0.014	0.158	0.007
0.10 - 0.15	0.331	0.881	0.019	0.129	0.008	0.337	0.866	0.017	0.130	0.007
0.15 - 0.20	0.310	0.854	0.024	0.112	0.007	0.310	0.825	0.023	0.111	0.006
0.20 - 0.30	0.273	0.787	0.024	0.098	0.007	0.267	0.767	0.023	0.094	0.006
0.30 - 0.40	0.214	0.701	0.037	0.072	0.006	0.202	0.678	0.034	0.065	0.005
0.40 - 0.50	0.152	0.429	0.053	0.051	0.005	0.138	0.442	0.048	0.043	0.004
0.50 - 0.60	0.101	0.432	0.078	0.024	0.004	0.085	0.418	0.068	0.020	0.003
0.60 - 0.80	0.049	0.498	0.101	0.009	0.003	0.034	0.482	0.089	0.007	0.002

The plots of $F_2^p - F_2^n$ and the contributions to the integral for the Gottfried sum to the measured range $0.004 < x_{Bj} < 0.8$ are shown for two different values of Q^2 in figure 5.21.

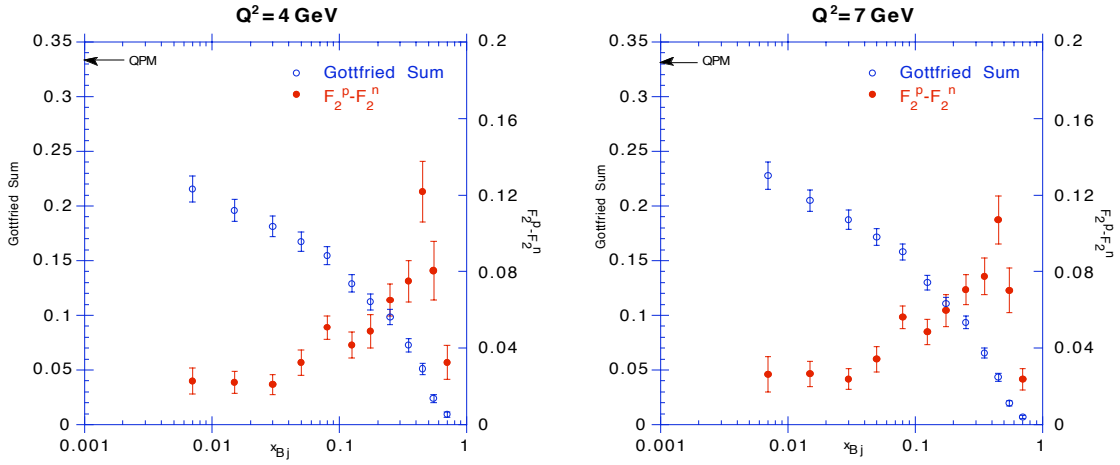

Figure 5.21:
The Gottfried Sum and $F_2^p - F_2^n$ for different values of Q^2.

However because the Gottfried sum covers the full range $0 < x_{Bj} < 1$ the integral must be extrapolated over the range $0 < x_{Bj} < 0.004$ and $0.8 < x_{Bj} < 1$. The contribution to the Gottfried sum for $0.8 < x_{Bj} < 1$, assuming a smooth extrapolation of the ratio F_2^n/F_2^p to 0.25 at $x_{Bj} = 1$, is estimated to be: 0.002 ± 0.001. For $0 < x_{Bj} < 0.004$ the extrapolation of $F_2^p - F_2^n$ is taken from a fit of the function $a\,x^b$. These results are given, along with the final calculations and the total errors, in table 5.8.

Table 5.8: The Gottfried Sum at two different values of Q^2.				
x_{Bj} range	$Q^2 = 4(\mathrm{GeV/c})^2$		$Q^2 = 7(\mathrm{GeV/c})^2$	
	$\sum_G$	Total error	$\sum_G$	Total error
$0.004 < x_{Bj} < 0.800$	0.216	0.012	0.228	0.013
$0.000 < x_{Bj} < 0.004$	0.037	0.030	0.039	0.032
$0.800 < x_{Bj} < 1.000$	0.002	0.001	0.002	0.001
Total:	0.254	0.035	0.269	0.037

Since there is good agreement, in the measured range, between the result at $Q^2 = 4\ (\mathrm{GeV/c})^2$ of 0.216±0.012 and the published result[13] of 0.227±0.007, the systematic error of ±0.014 from the published result is taken as a reasonable upper limit for the systematic error of the results. The sources of the systematic error include: radiative corrections, momentum measurement of the beam and scattered muons, vertex resolution and the uncertainty of the value of F_2^d. The momentum measurement was made with the same accuracy and the vertex resolution is the same as in the earlier publication[13]. However, because the knowledge of F_2^d and of the radiative corrections is now[12] better, the assumption that the published systematic error of ±0.014 is a good upper limit should be valid.

These results are consistent with the published results[13] of 0.240±0.016 and indicate a significant deviation from the value of 1/3 predicted by the quark parton model. While the most likely explanation for this discrepancy is a flavor asymmetric sea where $\bar{u} \neq \bar{d}$, other effects should also be considered.

References: Chapter 5

---

1 G. Mallot, NMC internal report, NMC/89/2 (1989).

2 J. Nassalski, NMC internal report, NMC/89/23 (1989);
A. D. Martin, R. G. Roberts and W.J. Stirling, *Phys. Lett.* **B207** (1988) 205.

3 NMC, P. Amaudruz *et al., Nucl. Phys.* **B371** (1992) 3.

4 NMC, P. Amaudruz *et al., Nucl. Phys.* **B371** (1992) 3;
E. Rondio, private communication.

5 G. T. Jones *et al.*, Oxford Univ. rep. OUNP-89-18 (1989);
G. T. Jones *et al.*, "Preliminary Results on the Ratio d/u(x).." paper submitted to the 1989 Int. Symp. on Lepton and Photon Interactions at High Energies, Stanford Univ. (1989).

6 M. van der Heijden, Ph. D. thesis (1991);
NMC, P. Amaudruz *et al., Nucl. Phys.* **B371** (1992) 3.

7 G. Altarelli and G. Martinelli, *Phys. Lett.* **B76** (1978) 89.

8 BCDMS, A. C. Benvenuti *et al., Phys. Lett.* **B223** (1989) 485;
BCDMS, A. C. Benvenuti *et al., Phys. Lett.* **B237** (1990) 592.

9 L. W. Whitlow *et al., Phys. Lett.* **B250** (1990) 193.

10 NMC, P. Amaudruz *et al., Phys. Lett.* **B294** (1992) 120.

11 A. Milsztajn, private communication.

12 NMC, P. Amaudruz *et al.*, *Phys. Lett.* **B295** (1992) 159.

13 NMC, P. Amaudruz *et al., Phys. Rev. Lett.* **66** (1991) 2712.

6. F_2 Structure Function Analysis

6.1 Introduction

The structure function $F_2\left(x_{Bj},Q^2\right)$, as determined from measurements of deep inelastic scattering, reflects the momentum distribution of quarks within the nucleon. The value of the structure function F_2 at low x_{Bj} determines the rates of reactions expected at the next generation of high energy colliders such as the LHC and the SSC. The Q^2 dependence of F_2 can be used to determine the scale parameter of QCD and the gluon momentum distribution of the nucleon. Previous knowledge of the proton and deuteron structure functions, F_2^p and F_2^d, stems from deep inelastic electron (SLAC[1]) and muon (BCDMS[2] and EMC[3]) scattering experiments.

For the precise determination of F_2 one needs cross sections on an absolute scale, in contrast to the relative cross sections that were used in the analysis of structure function ratios (Chapter 5). Therefore the spectrometer acceptance and the beam flux must be precisely determined.

The F_2 analysis starts with efficiency studies to determine the acceptance of the spectrometer. The comparison of the measured data to a Monte Carlo simulation of the experiment checks that the acceptance is well defined. For the normalization to the beam flux specially measured data (trigger 3/4 and trigger 10) are used.

Because the measured cross section also includes higher order radiative processes, as described in section 2.4, radiative corrections must be applied to obtain structure functions. These corrections are calculated from theory using the best known value of F_2 itself. Therefore, radiative corrections are obtained from an iterative procedure.

Corrections for the target contamination and the difference in the upstream and downstream acceptance were also applied. To determine the accuracy of the result systematic studies were performed.

6.2 Efficiency studies

To calculate the acceptance of the spectrometer one needs information on how efficiently tracks going through the apparatus are registered. Each detector plane has its efficiency calculated by determining, from the reconstructed tracks, the actual events found ("hits") and those that should have been found but were not ("fails") in the form:

$$\varepsilon = \frac{N_{Hits}}{N_{Hits} + N_{Fails}}. \tag{6.1}$$

Where ε is the efficiency, N_{Hits} the number of hits and N_{Fails} the number of fails. For the proportional and multi-wire drift chambers this calculation was further refined by requiring a minimum number of planes to be hit for a track to be considered a good track. For a plane requirement n_p the efficiency is now of the form:

$$\varepsilon = \frac{N_{Hits}\left(\geq n_p + 1\right)}{N_{Hits}\left(\geq n_p + 1\right) + N_{Fails}\left(\geq n_p\right)}. \tag{6.2}$$

6.2.1. Time dependent efficiency

A check that the average plane efficiency is reasonably constant over time is made. This is done by examining the average plane efficiency for each run. Changes in the average plane efficiency over time are seen in figure 6.1.

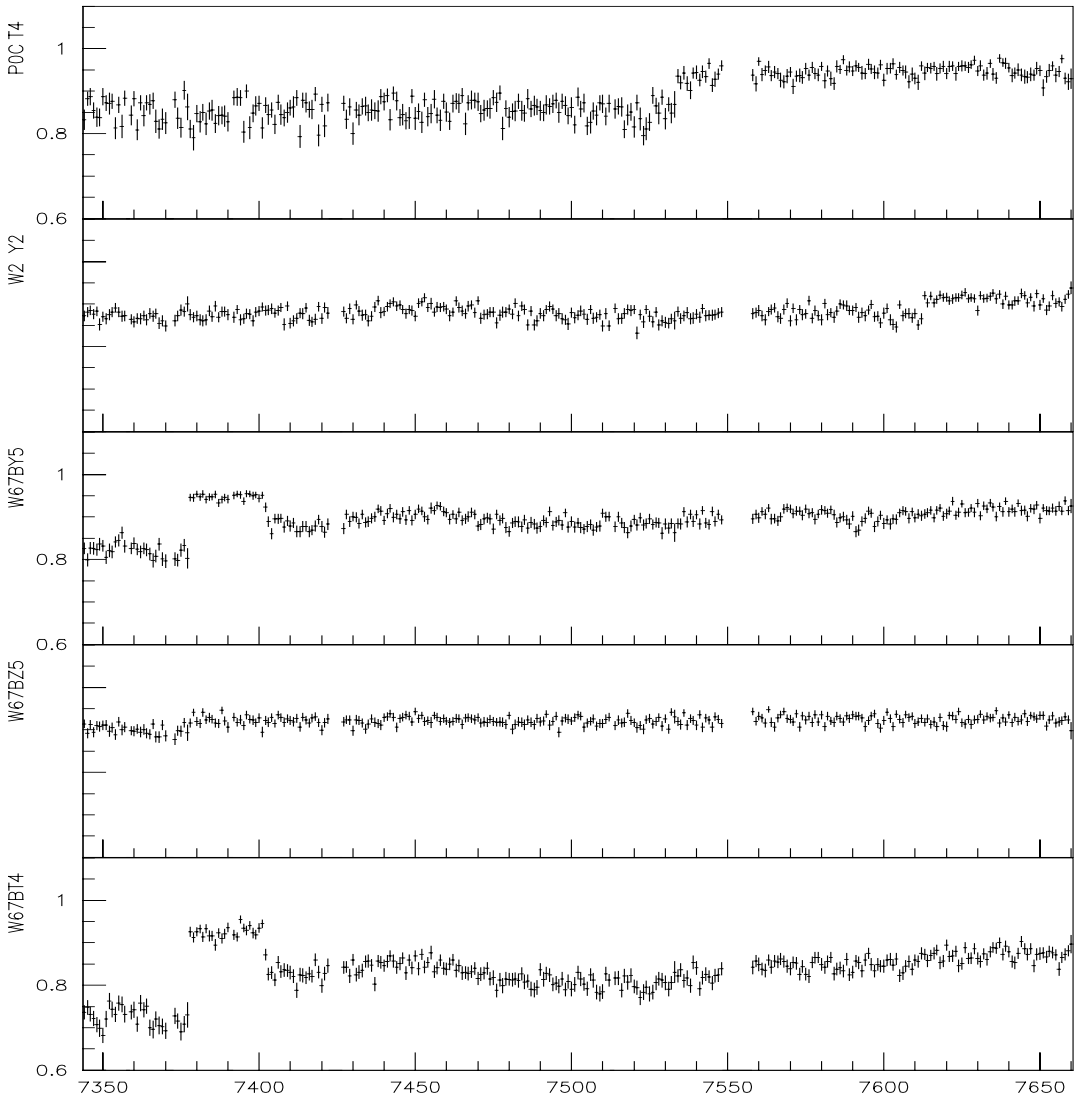

Figure 6.1: All the planes with a time dependent change in the efficiency.
These plots are of the efficiency versus the run number.
(The θ-planes are indicated by a T)

For the three planes: Y5, Z5 and θ4 of W67, the change in the efficiency was caused by a change in the high voltage of the sense wire. The change in the efficiency of the Y2 plane of W2 was probably also caused by a change in the high voltage. For the θ4

plane in P0C, the change in the efficiency was caused by the repair of a broken preamplifier.

In the case of P0C the region of the plane affected by the broken preamplifier was set to zero efficiency for the runs concerned in the efficiency parametrization. For the other planes, the period was broken up into separate groups of runs and the efficiency was calculated separately for each group for use in the efficiency parametrization.

6.2.2. Wire chamber support efficiency

In some planes, with long wires, an additional support is attached to the wires to keep them in their correct position. These supports locally degrade the efficiency; therefore, this must be included in the efficiency calculation. An example of such a degradation is seen in figure 6.2, in which the efficiency perpendicular to the support is given. The lower efficiency in the region of the supports is parametrized by a square well of depth equal to the minimum efficiency and having a width equal to the full width at half way between the minimum and the average plane efficiency.

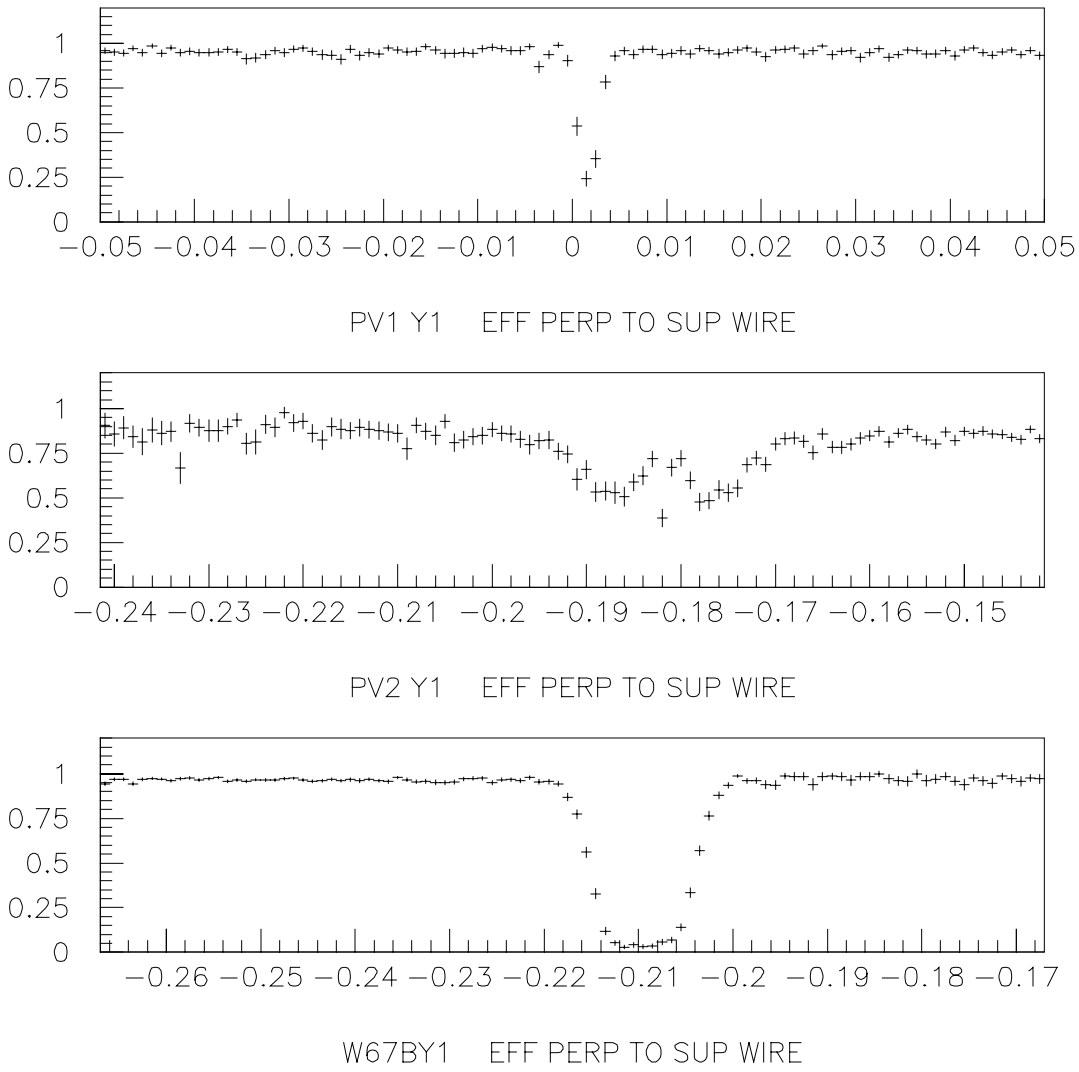

Figure 6.2:
The efficiency perpendicular to the support for the planes: PV1-Y1, PV2-Y1 and W67B-Y1.

6.2.3. Wire chamber and trigger hodoscope efficiencies

After examining the time dependent efficiencies and modeling the inefficiency perpendicular to the readout wires, due to the wire supports, the parametrization of the

efficiency of the wire readout and trigger hodoscope planes must be done. The usual three types of parametrizations are: (i) an efficiency averaged over the whole plane, (ii) a radial fit or (iii) a fit to groups of wires. These parametrizations assume that the efficiency along the wire (or hodoscope element) is uniform, or at least smoothly varying (for the radial efficiency fit).

6.2.3.1. General planes

The following efficiency plots were examined: (i) the efficiency versus wire(element) number, (ii) the projected radial efficiency, and for multi-wire drift chambers, (iii) the average efficiency versus the position within the drift cell.

To improve the accuracy of the efficiency parametrizations, wires(elements) that were either dead or had an abnormally low efficiency compared with the neighboring wires(elements) were removed from the plots and efficiency calculations. These few unusually inefficient wires(elements) were then parametrized as individual wires(elements), or groups of wires with a fixed efficiency, and were treated separately during track reconstruction.

The remaining wires(elements) were then re-plotted and parametrized as one of the three types of parametrizations, an efficiency averaged over the whole plane, a radial fit, a fit to groups of wires or sometimes a drift cell efficiency. An example of planes that were either fit with a radial fit or where groups of wires were fit is seen in figure 6.3.

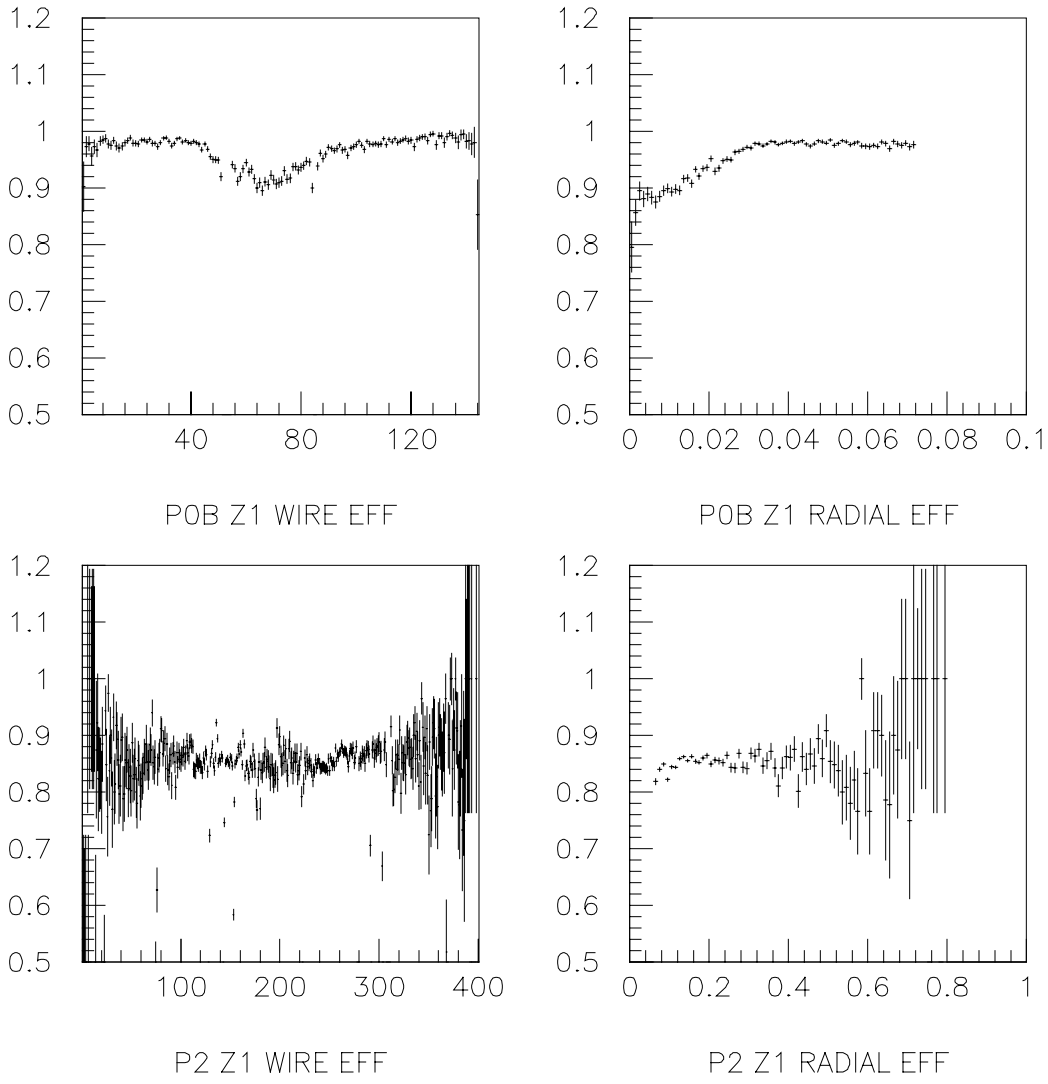

Figure 6.3:
The plots of efficiency versus wire number and radial efficiency for the planes P0B-Z1 and P2-Z.

Planes, like P0B, with a smooth efficiency in both the wire and radial projections were parametrized with a radial fit; while planes, like P2, with jumps in their efficiency are fit by grouping wires together, typically 5 or 10 wires, and setting them to the average efficiency of the group.

An example of the efficiency of one plane of a multi-wire drift chamber is given in figure 6.4.

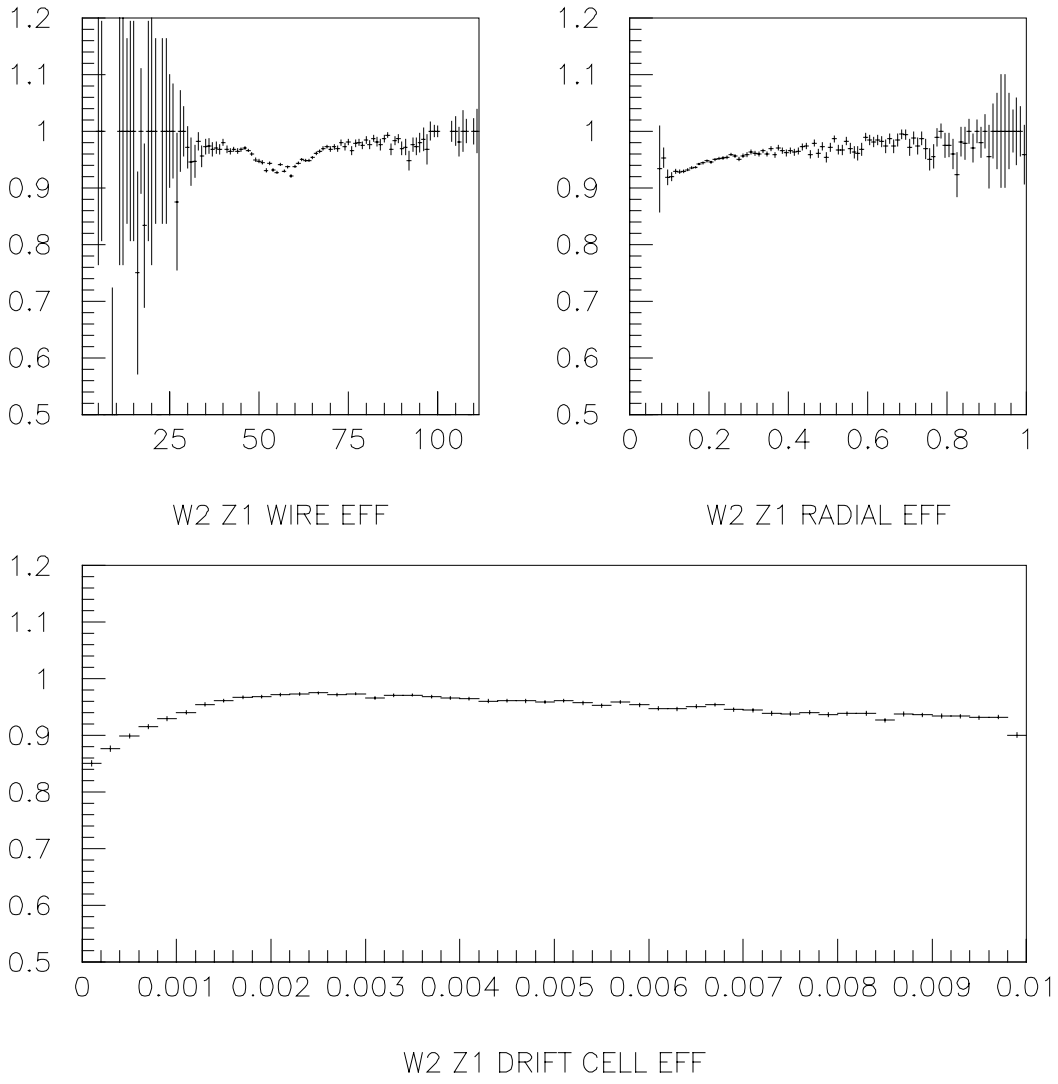

Figure 6.4:
Efficiency versus wire number, radial efficiency and the drift cell efficiency for W2-Z1

The multi-wire drift chambers were parametrized by first separately fitting the efficiency within the drift cell and making a fit of the radial efficiency, then combining the two efficiencies in the form:

$$\varepsilon = 1 - \frac{\left(1 - \varepsilon_{Radial}\right)\left(1 - \varepsilon_{Drift}\right)}{1 - \varepsilon_{average}}. \tag{6.3}$$

Here ε_{Radial} is the radial efficiency from the fit, ε_{Drift} is the fitted efficiency within the drift cell and $\varepsilon_{Average}$ is the average plane efficiency.

The efficiency versus element number for the trigger 1 hodoscopes is shown in figure 6.5. These planes were fit using the average efficiency.

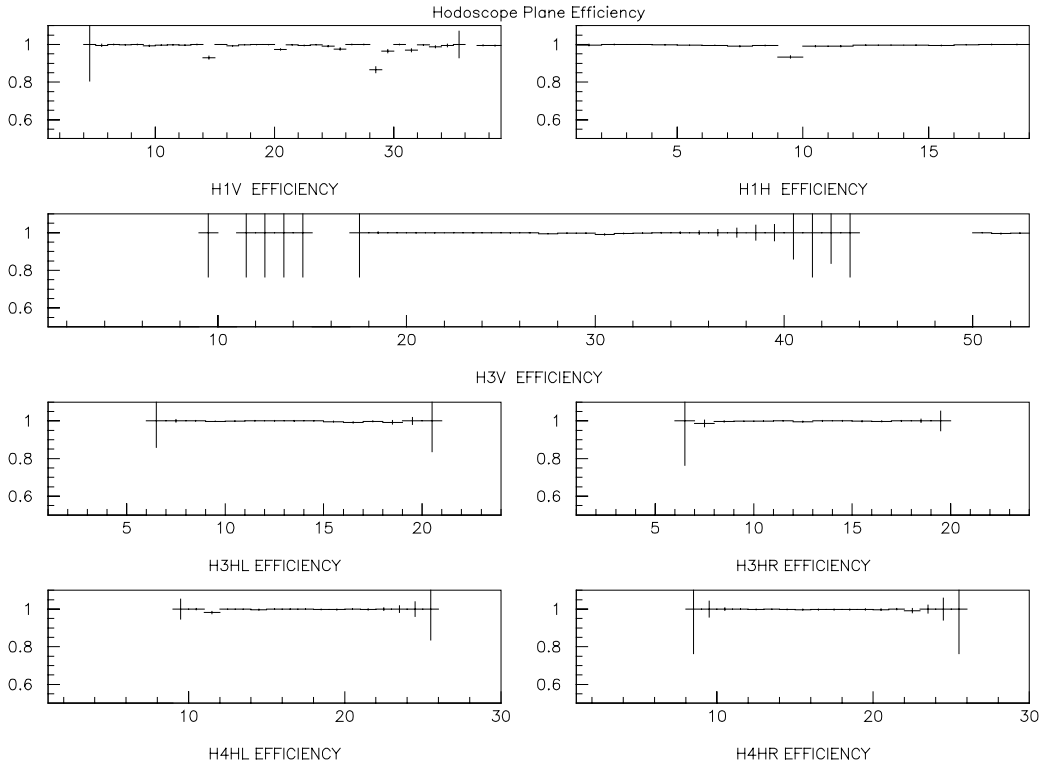

Figure 6.5:
The efficiency versus element number for the trigger 1 hodoscopes.

6.2.3.2. Problem planes

While on the whole the parametrization of the efficiency went smoothly, there were three major problems that needed considerable extra work to model. These problems were, the efficiency as a function of position along the wire or hodoscope element, the aging of W12 and the background in both W45 and P45.

The normal efficiency calculations, as stated above, assume a uniform efficiency along the wire or hodoscope element. When this assumption is not true some corrective action must be taken. This problem has manifested itself in two ways; in W67B some of the central wires did not have a uniform efficiency and in the central elements of H1H and H1V there were a few strips with a position dependent efficiency.

In W67 this is true for one wire in particular, wire number 18 of plane W67B Z5, as shown in figure 6.6. Because of the redundancy of Z-planes in W67 this wire could simply be removed from the track reconstruction.

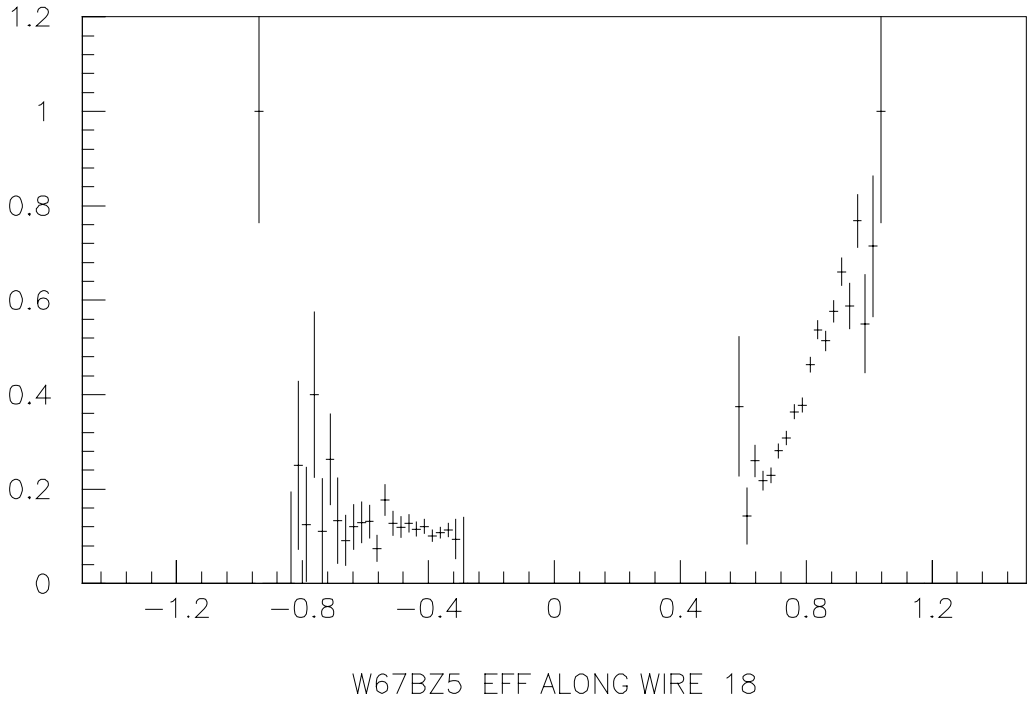

Figure 6.6:
The efficiency along the wire for wire #18 of plane W67B-Z5.

For problematic hodoscope elements, however there was no redundancy so rather than “killing” a bad element the efficiency was fitted with a linear function of the position and this fit was used as a correction to the analysis program. The problematic hodoscope elements; numbers 14 and 28 of plane H1V and element number 9 of plane H1H are shown in figure 6.7, along with one good element (number 10 of plane H1H) for comparison.

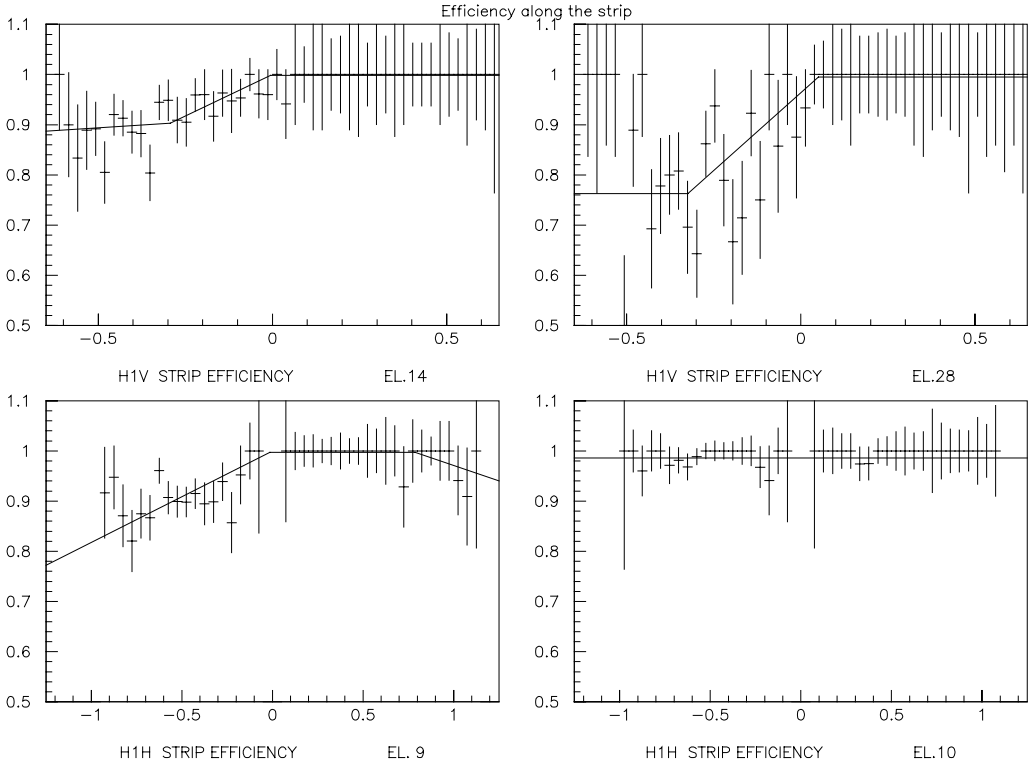

Figure 6.7:
The alongside efficiency and fits for the elements:
H1V #14, H1V #28, H1H #9 and H1H #10.

The single most time consuming problem was aging for some of the W12 planes. The best guess as to the cause of this problem was hydrocarbon buildup on the readout wires. It manifested itself as a drop in the efficiency, primarily in the central region, and differences in the drift cell efficiency. An example of this problem, for one plane, is seen in figure 6.8:

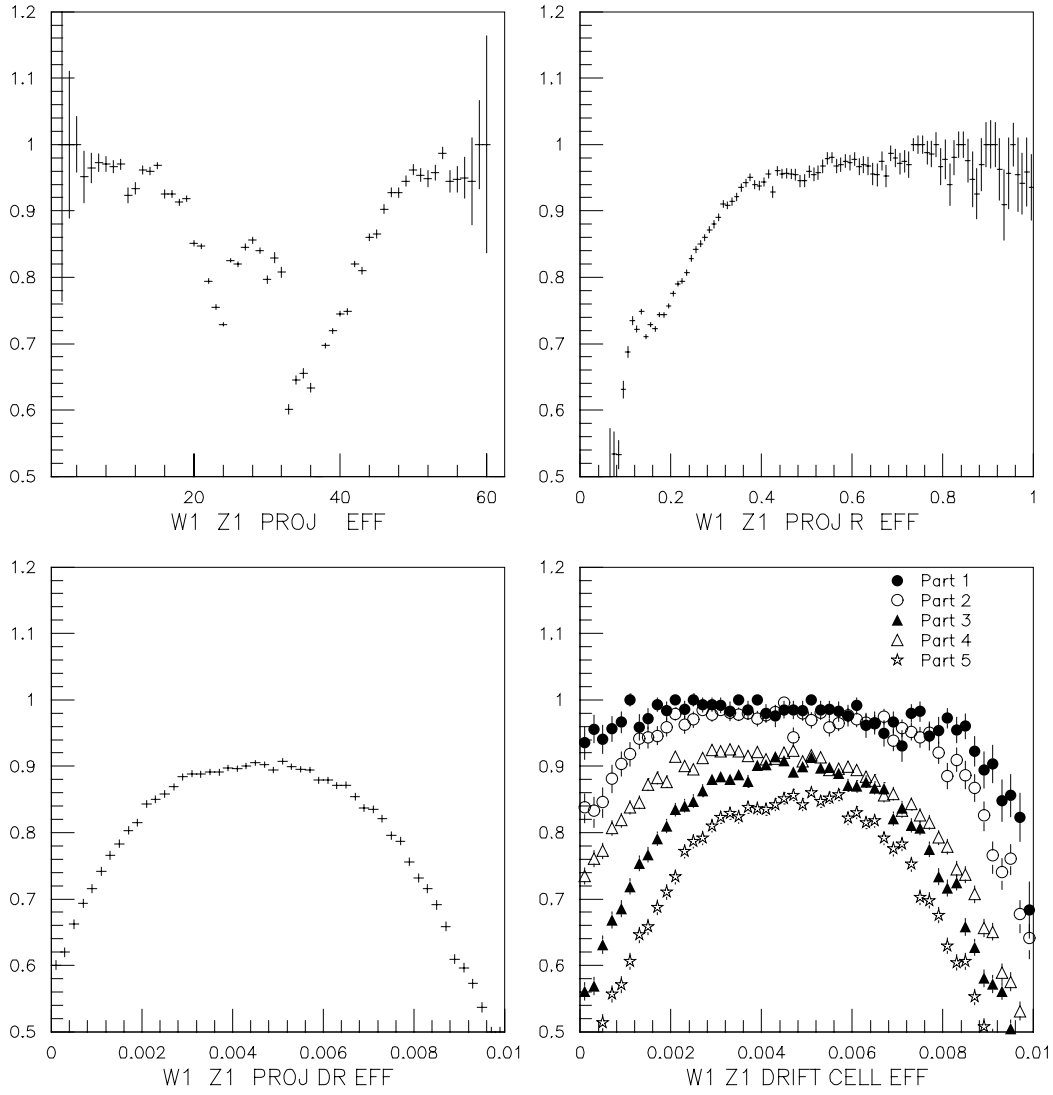

Figure 6.8:
The plots of the efficiency of plane W1 Z1.

In this figure the plots of the efficiency versus wire number, the radial efficiency, the average drift cell efficiency for the whole plane and an overlay of the drift cell

efficiencies, for some of the different parts of the plane, are shown (for comparison with a good plane, see figure 6.4).

Because the efficiency within the drift cell changed drastically for different regions a new method of parametrization was developed. This method involved separating the plane into different parts. Each part is then separately fitted using the normal drift chamber method and then joined together for input into the Monte Carlo track reconstruction program. The problematic planes in W12 were: W1-Y1, W1-Z1, W1-θ1, W2-Y2 and W2-θ1.

The high background in the W45/P45 region leads to loss of tracks and thus an overestimation of the efficiency. This effect was small for the P45 proportional chambers and could be corrected for in the analysis program with a parametrization based on the kinematic variable *y*. The losses in P45 were due to high hit multiplicity caused by background. In W45 the losses were caused by leak through of charge from one drift cell to another, causing multiple hits; in addition to high multiplicity from the background. Because of the long dead time in the readout electronics these multiple hits caused larger track losses and therefore a much larger overestimation of the W45 efficiency. In the region of overlap between P45 and W45, where the P45 chambers add to the track reconstruction, there is good agreement between the W45 and P45 efficiency estimation. However this is not true in the region where only W45 tracks are used for the efficiency calculation. The step in the radial efficiency of Z planes of W45 shows this problem, see figure 6.9. Because the background problem in W45 is not well understood tracks from the region outside of the radius of P45 were excluded from the analysis. This caused a loss of some 25 percent of the data.

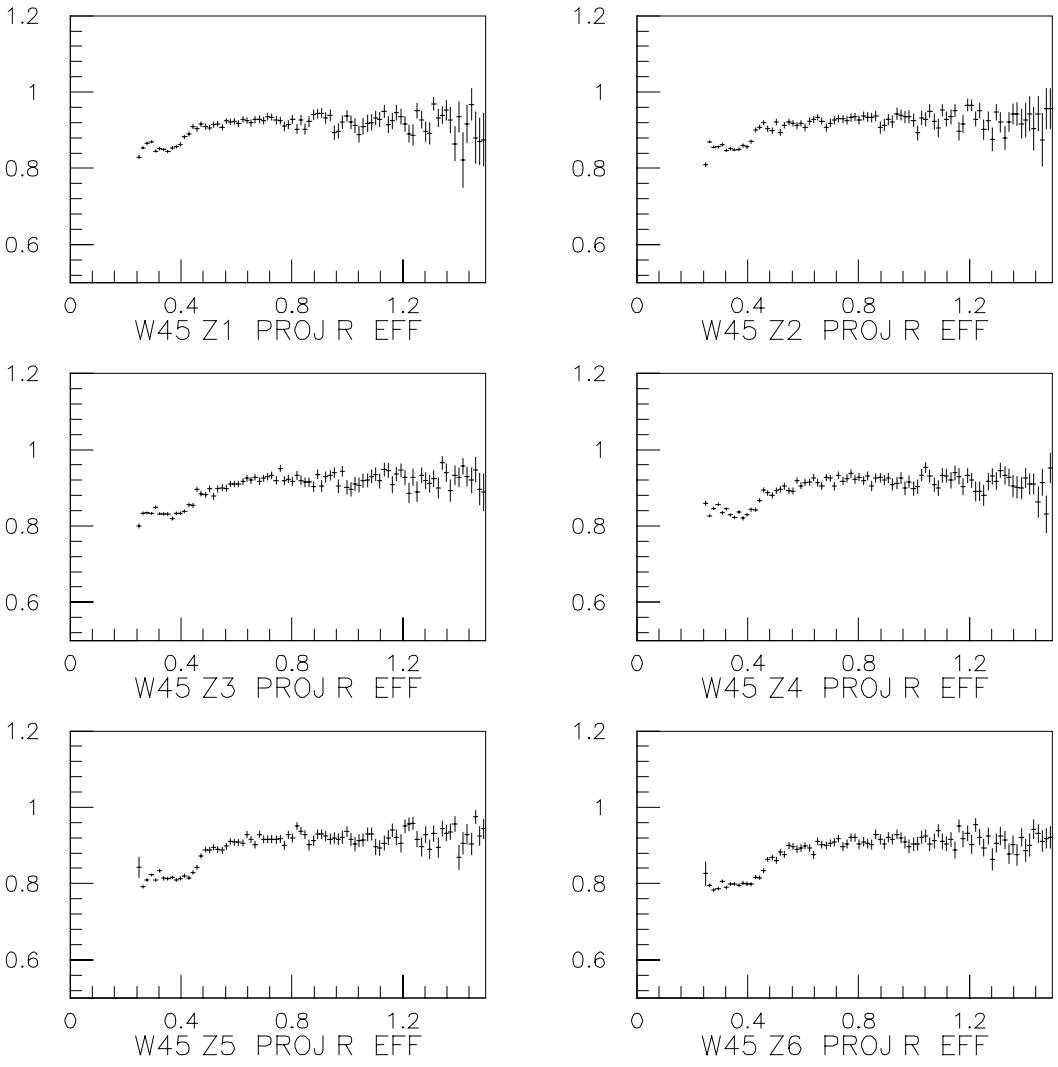

Figure 6.9:
The radial efficiency of the Z planes of W45.

The types of fits used for the various detectors are given in table 6.1:

Table 6.1:
The types of efficiency parametrization used

Detector	Type of Fit	Comments
P0B	Radial	
P0C	Radial	
PV12	Groups of Wires	10 Wires
P0D	Radial	
P123	Groups of Wires	10 Wires for Y, θ planes; 5 Wires for Z
P0E	Radial	From T2
W12	Drift Chamber	(W1Y1, W1Z1, W1θ1, W2Y2, W2θ1 Special)
P0A	Plane Average	
W45	Drift Chamber	
P45	Radial	
W67A	Plane Average	
W67B	Groups of Wires	Individual wires
W67C	Plane Average	
T1 Hodoscopes	Plane Average	

6.3 Monte Carlo Simulation

Because of the complexity of the spectrometer and of the reconstruction software, it is impossible to analytically reproduce a measurement from a given cross section and the efficiencies.

Therefore a computer simulation is performed with events generated primarily from the cross section distribution, called a Monte Carlo simulation. The generated

events are then transformed into hits within the detector using the parametrized efficiencies.

These Monte Carlo events are processed through the full reconstruction software analysis as if they were measured events. The software reconstruction efficiencies are thus also taken into account. In the end these Monte Carlo simulated events are compared to measured data.

The ratio of the data and Monte Carlo events should be equal to unity and independent of any variable. Examples are given in figures 6.10 and 6.11, where the ratios of data and Monte Carlo events are shown as a function of the kinematics variables. In this example the results are satisfactory. This is less so however in figures 6.12 and 6.13, the plots of ratios of data and Monte Carlo events, as a function of the radial position in various detectors. The reconstruction in the downstream target by P45 in particular shows a problem. The remedy has not yet been found, but the influence on the final results does not seem to be significant. The comparison between the simulated and measured efficiency supports this.

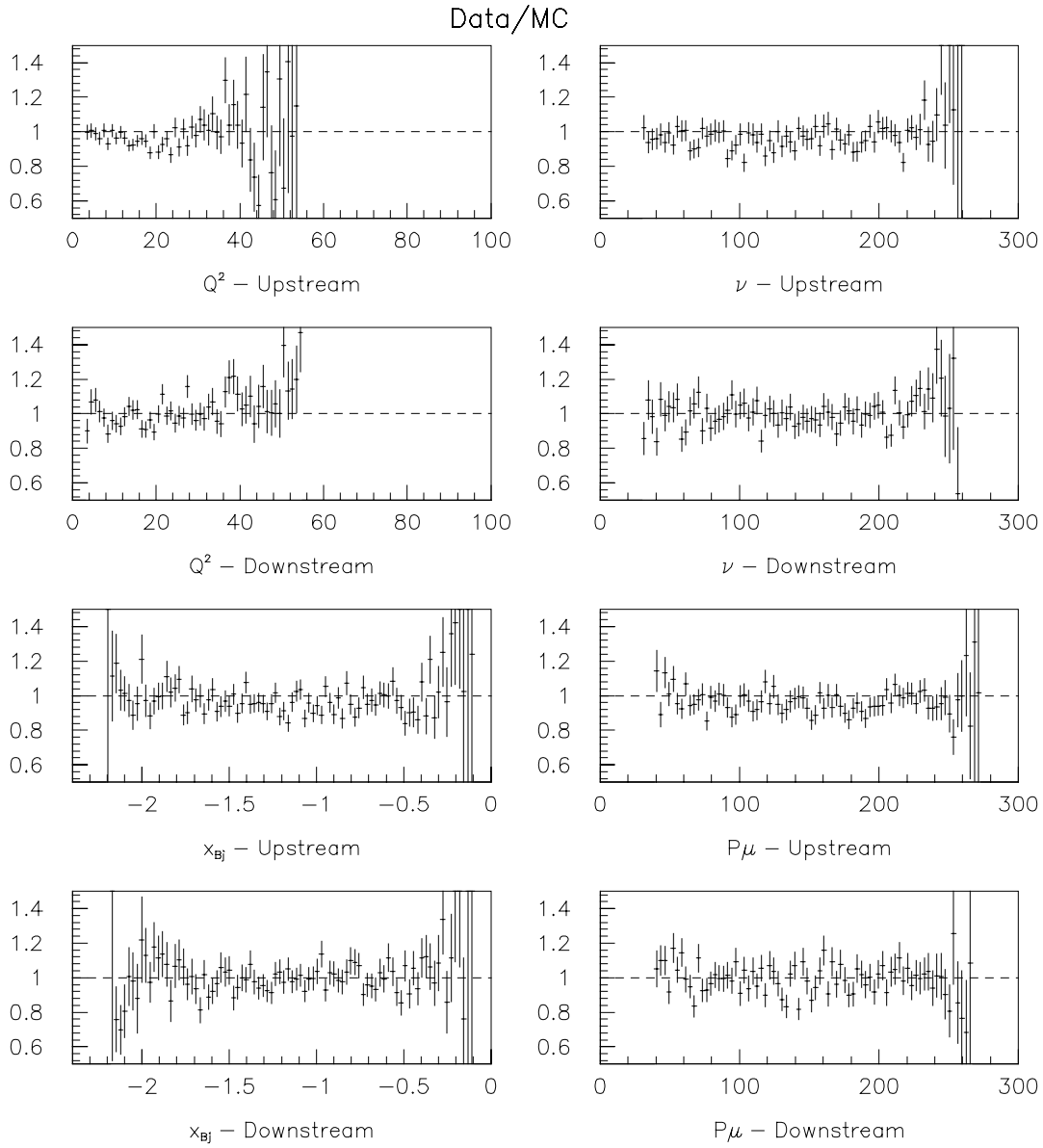

Figure 6.10:
The ratio of data and Monte Carlo events, for Q^2, ν, x_{Bj} and P'_{μ} from deuterium.

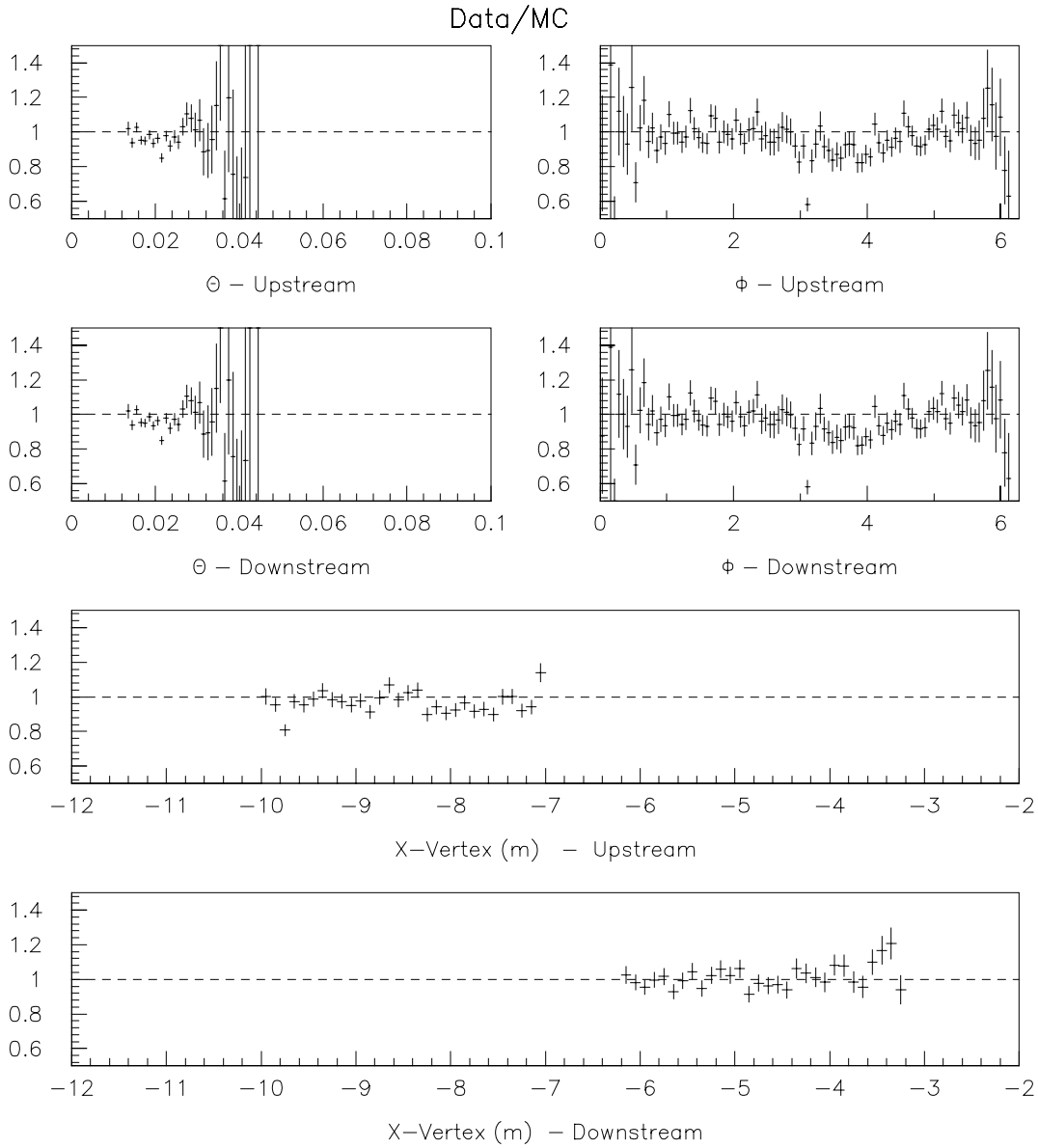

Figure 6.11:
The ratio of data and Monte Carlo events, for θ, ϕ and the **x**-position of the interaction vertex, from deuterium.

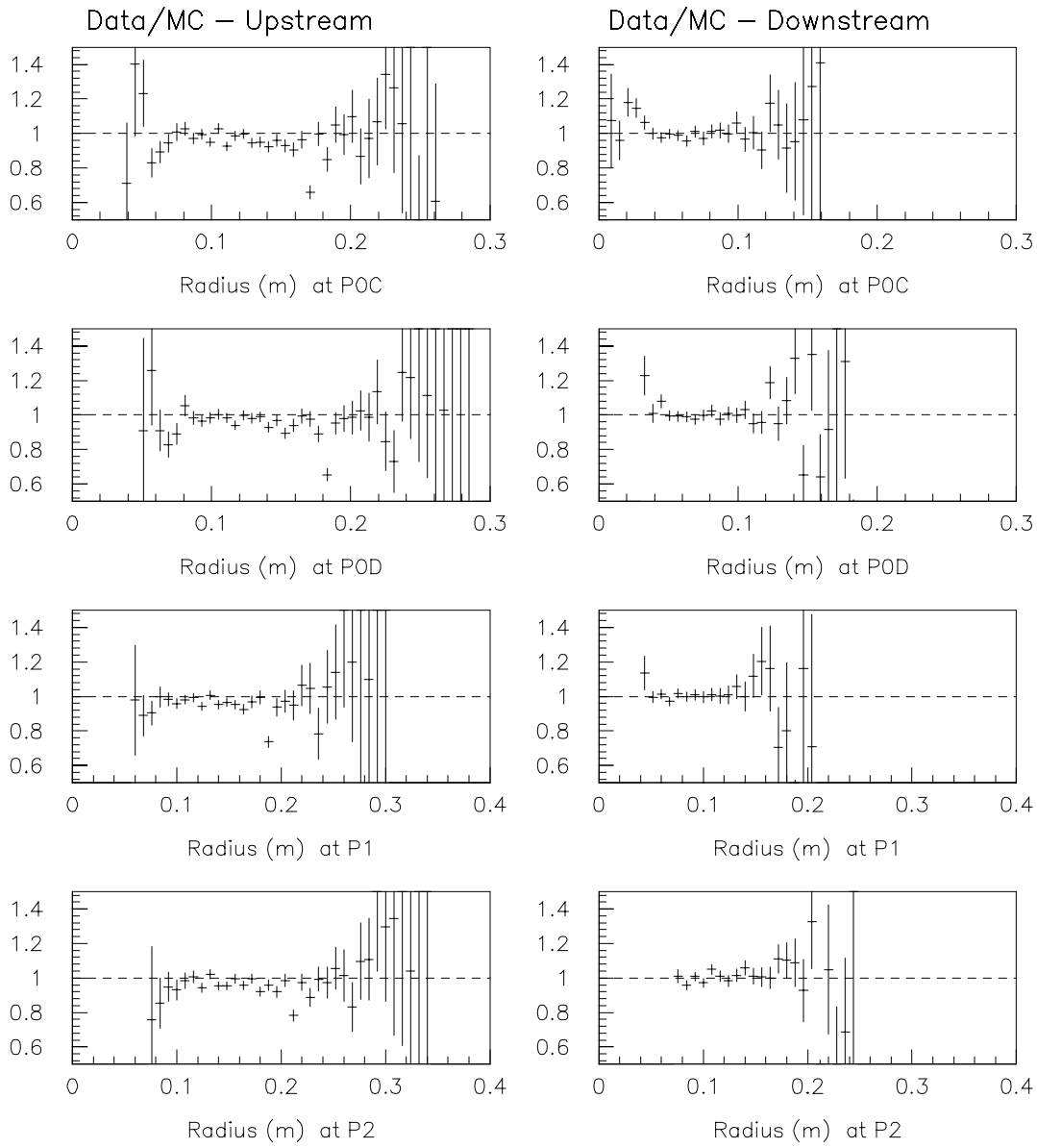

Figure 6.12:
The ratio of data and Monte Carlo events, in the P0C, P0D P1 and P2 detectors, from deuterium.

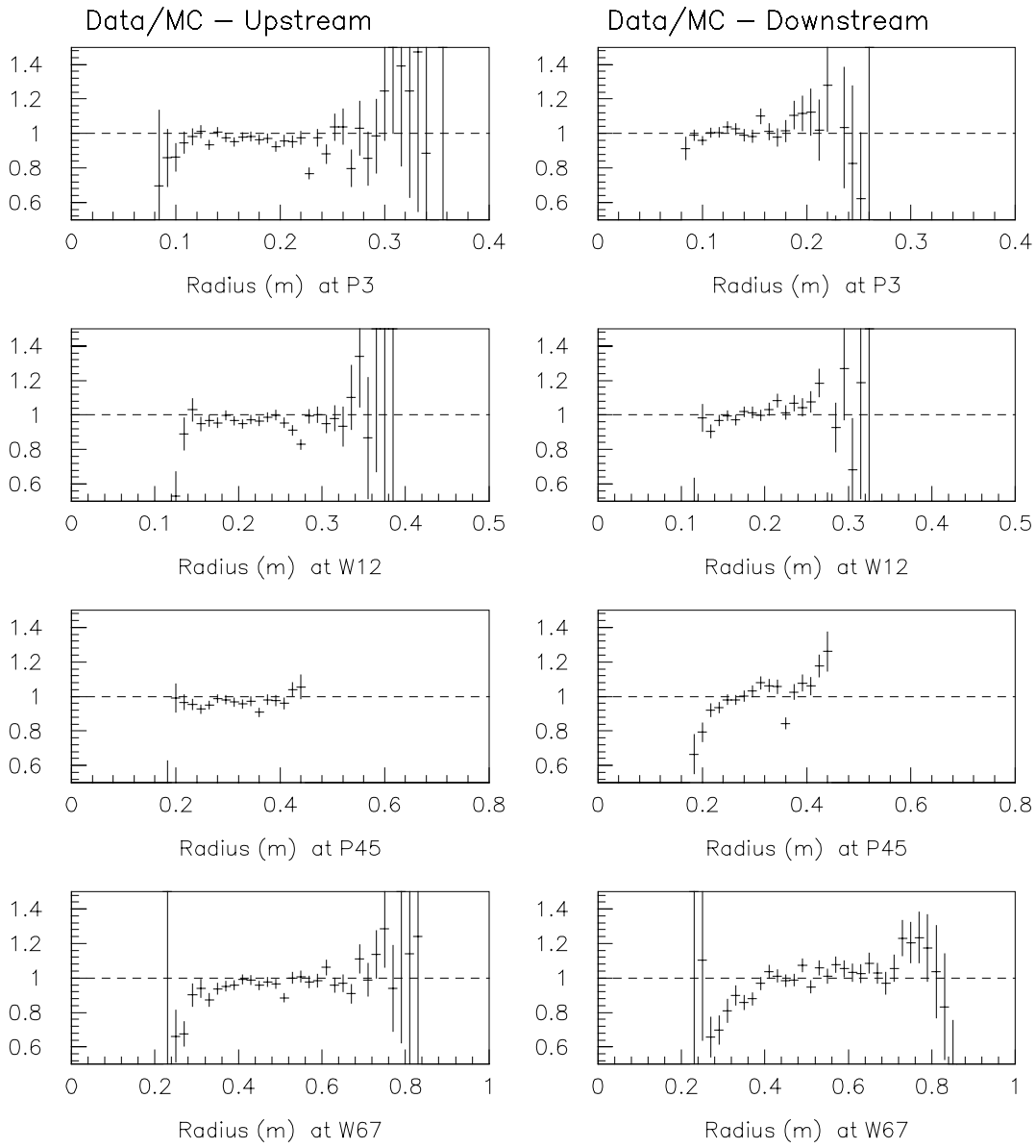

Figure 6.13:
The ratio of data and Monte Carlo events, in the P3, W12, P45 and W67 detectors, from deuterium.

Another check that was done on the Monte Carlo simulation was the calculation of the simulated efficiency to be compared to the measured efficiency. An example of such a comparison is shown in figure 6.14; the efficiency of a problematic plane in W12 is seen to be reasonably well reproduced.

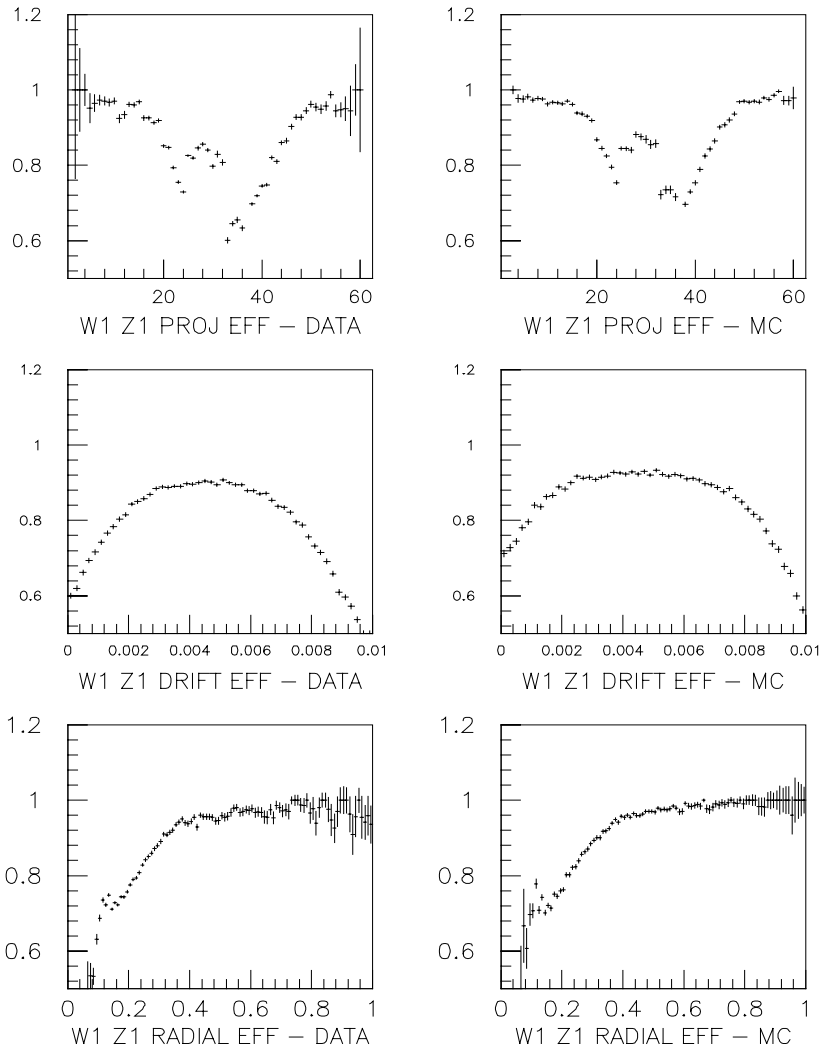

Figure 6.14: Comparison of data and Monte Carlo reconstruction for a problematic plane in W12.

An example of a plane that was not properly reproduced is seen by the slight drop in the radial efficiency (below 0.3 m) in figure 6.15. However when this plane was removed from the calculations only minor changes in that detector were observed, because of the redundant number of reconstruction planes. This caused a loss of 3.5% of the data.

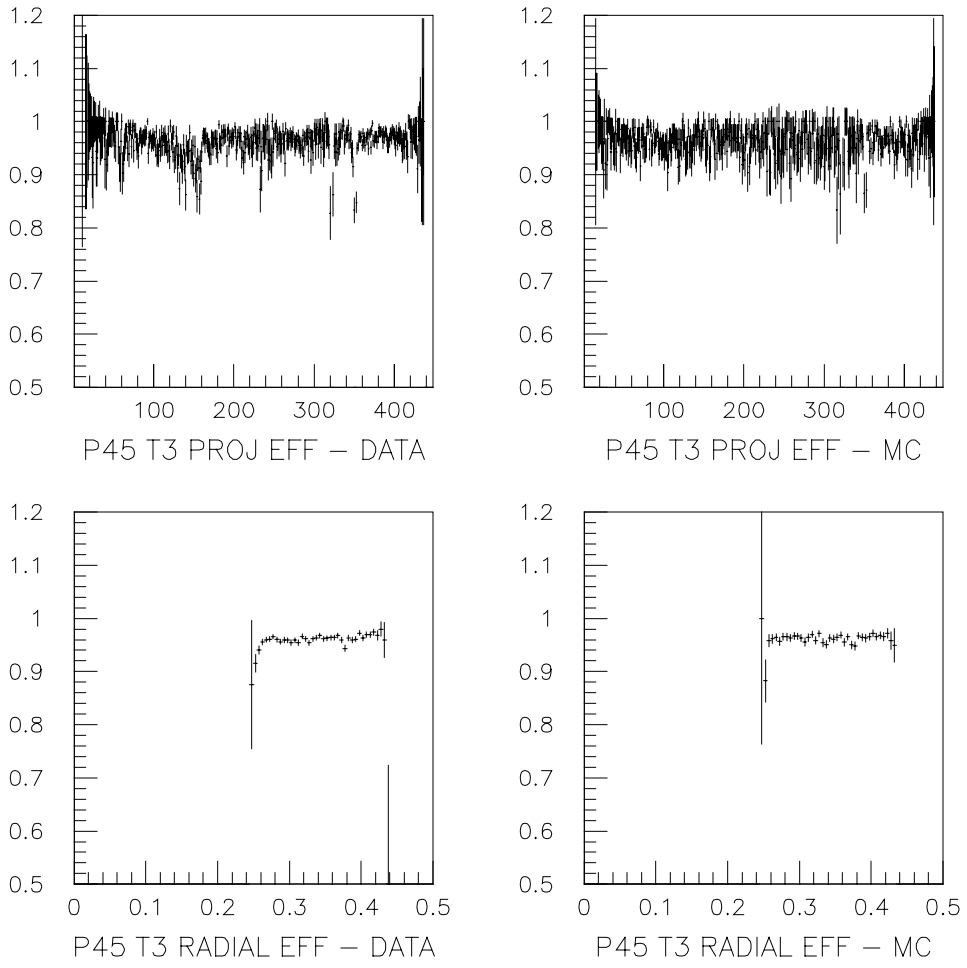

Figure 6.15:
A comparison of data and Monte Carlo reconstruction for the plane $\theta 3$ in P45.

After making various checks, final cuts were set on both the detector coordinates and the kinematic variables. These kinematics cuts are shown in table 6.2 and the detector cuts are shown in table 6.3:

Table 6.2:
The accepted range of the kinematic variables.

Variable	Upstream target	Downstream target
x_{Bj}	$0.004 \le x_{Bj} \le 1.0$	$0.004 \le x_{Bj} \le 1.0$
Q^2	$Q^2 \ge 2.0\ (\mathrm{GeV/c})^2$	$Q^2 \ge 3.0\ (\mathrm{GeV/c})^2$
ν	$\nu \ge 30.0$ GeV	$\nu \ge 30.0$ GeV
y	$y \le 0.9$	$y \le 0.9$
θ	$\theta \ge 13$ mrad	$\theta \ge 15$ mrad
P'_{μ}	$P'_{\mu} \ge 40.0$ GeV/c	$P'_{\mu} \ge 40.0$ GeV/c

Table 6.3
The various detector cuts used

Detector	Events Cut	Reason for cut
PV1	R<7.1 cm	Limit of efficiency fit
P1, P3	R<6.5 cm	Region of poor efficiency
P2	R<7.5 cm	Region of poor efficiency
P0D	R<3.0 cm	Region of poor efficiency
BMS-Trigger Time	ABS(BMS-Trigger)<4 ns	Insure good time correlation

The numbers of events that were cut and the numbers of remaining events, for each target position, are given in table 6.4:

Table 6.4:
The results of the kinematics and detector cuts.

	Target Position			
	D_2 upstream	H_2 downstream	H_2 upstream	D_2 downstream
Initial events	100184	31908	50514	66276
Failed kinematics cuts	40703	13012	22161	26515
Failed detector cuts	18166	8526	9475	17570
Remaining events	41315	10370	18878	22191

6.4 F_2 Results

After determining the spectrometer acceptance with the Monte Carlo simulation, each accepted Monte Carlo event was weighted with the one-photon exchange cross section times a radiative correction factor η. This factor is given by: $\eta = \sigma^{tot}/\sigma^{1\gamma}$. For the calculation of η one requires as input the F_2 structure function and the ratio of the longitudinal to transverse absorption cross sections, *R*. These inputs were taken from the latest published results[4]. The structure function F_2 for this period was calculated by taking the data over Monte Carlo result multiplied by the input F_2 value, at every x_{Bj} and Q^2 point.

To compare the data with the Monte Carlo results, both must be normalized to the same flux. The data is normalized by dividing the number of events by the muon flux

measured with the normalization triggers. The Monte Carlo results are normalized to the number of events in the generation space such that:

$$\phi_{MC} = \frac{N_{MC}}{A N_{Tgt}}. \tag{6.4}$$

Here N_{MC} is the total number of generated Monte Carlo events, N_{Tgt} is the number of target nucleons and A is the area of integration of the kinematic region. The area of integration of the kinematic region is simply $A = (\nu_{\max} - \nu_{\min})\left(\mathrm{Log}\,Q^2_{\max} - \mathrm{Log}\,Q^2_{\min}\right)$, since the Monte Carlo events are generated uniformly in ν and $1/Q^2$.

Comparisons of the two normalization triggers and the upstream versus downstream acceptance were made from numbers calculated from a simple fit to a constant, of the ratio of the data to the Monte Carlo events, for some of the kinematic variables. The results are shown in table 6.5:

Table 6.5:
Trigger 3/4 and Trigger 10 Normalization

Data/MC Deuteron	QSQ	VNU	XBJ	Y	X-Vertex	Average
T3 - Up	0.9773	0.9746	0.9732	0.9752	0.9762	0.9753
T3 - Down	1.0170	1.0100	1.0130	1.0110	1.0160	1.0134
T10 - Up	0.9614	0.9576	0.9574	0.9588	0.9595	0.9589
T10 - Down	0.9971	0.9891	0.9929	0.9897	0.9965	0.9931
T3/T10 -Up	101.7%	101.8%	101.7%	101.7%	101.7%	101.7%
T3/T10 -Down	102.0%	102.1%	102.0%	102.2%	102.0%	102.0%
Up/Down - T3	96.1%	96.5%	96.1%	96.5%	96.1%	96.2%
Up/Down - T10	96.4%	96.8%	96.4%	96.9%	96.3%	96.6%

Data/MC Proton	QSQ	VNU	XBJ	Y	X-Vertex	Average
T3 - Up	0.9793	0.9751	0.9744	0.9750	0.9798	0.9767
T3 - Down	1.0130	1.0060	1.0030	1.0060	1.0110	1.0078
T10 - Up	0.9626	0.9576	0.9567	0.9587	0.9624	0.9596
T10 - Down	0.9962	0.9900	0.9911	0.9890	0.9953	0.9923
T3/T10 -Up	101.7%	101.8%	101.9%	101.7%	101.8%	101.8%
T3/T10 -Down	101.7%	101.6%	101.2%	101.7%	101.6%	101.6%
Up/Down - T3	96.7%	96.9%	97.1%	96.9%	96.9%	96.9%
Up/Down - T10	96.6%	96.7%	96.5%	96.9%	96.7%	96.7%

The difference between the two normalization triggers is caused by an improper calibration of the time window of trigger 10 (See section 3.6.2). Therefore trigger 3 was used for the flux normalization for the data.

Figure 6.16 shows the x_{Bj} dependence of the structure function F_2, averaged over Q^2 and plotted with statistical errors only, for both the proton and the deuteron. The comparison of the extracted value of F_2 with the input structure function F_2 is shown in

both figures, 6.15 and 6.16. The plotted points are given with statistical errors only and the line shown is the fit, taken from the BCDMS[2], NMC[4] and SLAC[1] data, of the input value of F_2.

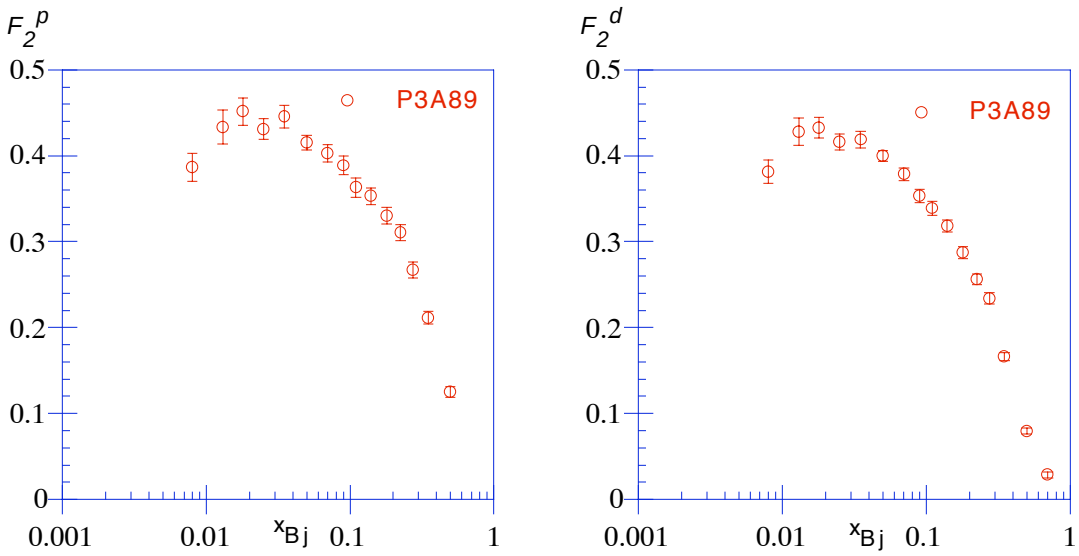

Figure 6.16:
The F_2 structure function versus x_{Bj} for the proton and the deuteron.

The NMC is currently in the process of analyzing the proton and deuteron F_2 structure functions. This analysis will combine the data from the 1986 and 1987 periods, which had beam energies of 90 and 280 GeV, with the data from 1989. The data from 1989 had beam energies of 120, 200 and 280 GeV. This thesis deals with data from only one of the 1989 periods with beam energy of 280 GeV. Therefore the results presented in the following tables are not the final results from the NMC analysis and should be taken as preliminary results.

The results, as a function of x_{Bj} and Q^2, for the proton F_2 structure function are given in table 6.6 and seen in figure 6.17. The systematic errors are taken from the latest NMC F_2 publication[4]:

Table 6.6:
The proton structure function F_2^p. (Q^2 in $(\text{Gev/c})^2$)

Q^2	$F_2^p(x_{Bj},Q^2)$	Stat. error	Syst. error	Q^2	$F_2^p(x_{Bj},Q^2)$	Stat. error	Syst. error
At x_{Bj}=0.0080				At x_{Bj}=0.0700			
3.47	0.3864	0.0166	0.0185	11.62	0.4019	0.0246	0.0051
At x_{Bj}=0.0125				14.92	0.3942	0.0157	0.0044
4.56	0.4330	0.0178	0.0140	19.61	0.4074	0.0149	0.0044
5.43	0.4335	0.0198	0.0180	25.23	0.4196	0.0329	0.0053
At x_{Bj}=0.0175				At x_{Bj}=0.0900			
5.62	0.4722	0.0320	0.0127	11.72	0.3999	0.0334	0.0057
6.84	0.4515	0.0160	0.0134	15.05	0.3516	0.0184	0.0048
At x_{Bj}=0.0250				19.84	0.3979	0.0166	0.0052
7.22	0.4111	0.0172	0.0084	26.00	0.4266	0.0225	0.0057
8.92	0.4249	0.0144	0.0094	At x_{Bj}=0.1100			
10.93	0.4460	0.0228	0.0131	11.83	0.3714	0.0425	0.0062
At x_{Bj}=0.0350				14.95	0.3473	0.0239	0.0054
9.12	0.3961	0.0208	0.0061	19.78	0.3504	0.0171	0.0053
11.47	0.4408	0.0154	0.0075	26.30	0.3720	0.0201	0.0058
14.26	0.4575	0.0246	0.0095	34.28	0.4863	0.0506	0.0073
At x_{Bj}=0.0500				At x_{Bj}=0.1400			
9.22	0.4191	0.0305	0.0050	14.97	0.3587	0.0220	0.0059
11.55	0.3893	0.0145	0.0045	20.03	0.3584	0.0149	0.0055
14.85	0.4198	0.0127	0.0051	26.52	0.3564	0.0148	0.0056
18.89	0.4534	0.0202	0.0060	35.37	0.3289	0.0245	0.0057

Table 6.6 (continued):
The proton structure function F_2^p. (Q^2 in $(\text{Gev/c})^2$)

Q^2	$F_2^p(x_{Bj},Q^2)$	Stat. error	Syst. error	Q^2	$F_2^p(x_{Bj},Q^2)$	Stat. error	Syst. error
At x_{Bj}=0.1800				At x_{Bj}=0.2750			
5.08	0.3207	0.0250	0.0055	15.88	0.3070	0.0497	0.0046
19.88	0.3123	0.0163	0.0049	19.99	0.2384	0.0165	0.0031
26.81	0.3332	0.0158	0.0053	26.77	0.2867	0.0174	0.0035
34.94	0.3551	0.0217	0.0056	35.39	0.2856	0.0197	0.0030
45.47	0.3336	0.0407	0.0056	46.40	0.2606	0.0277	0.0026
At x_{Bj}=0.2250				At x_{Bj}=0.3500			
15.24	0.2740	0.0248	0.0048	20.68	0.1953	0.0154	0.0022
19.90	0.2834	0.0157	0.0041	26.84	0.2091	0.0114	0.0027
26.59	0.3282	0.0166	0.0043	35.29	0.2116	0.0126	0.0036
34.89	0.3130	0.0190	0.0042	46.99	0.2163	0.0172	0.0040
45.91	0.3553	0.0332	0.0048	At x_{Bj}=0.5000			
				27.90	0.1193	0.0103	0.0059
				35.52	0.1244	0.0079	0.0064
				46.43	0.1261	0.0101	0.0078

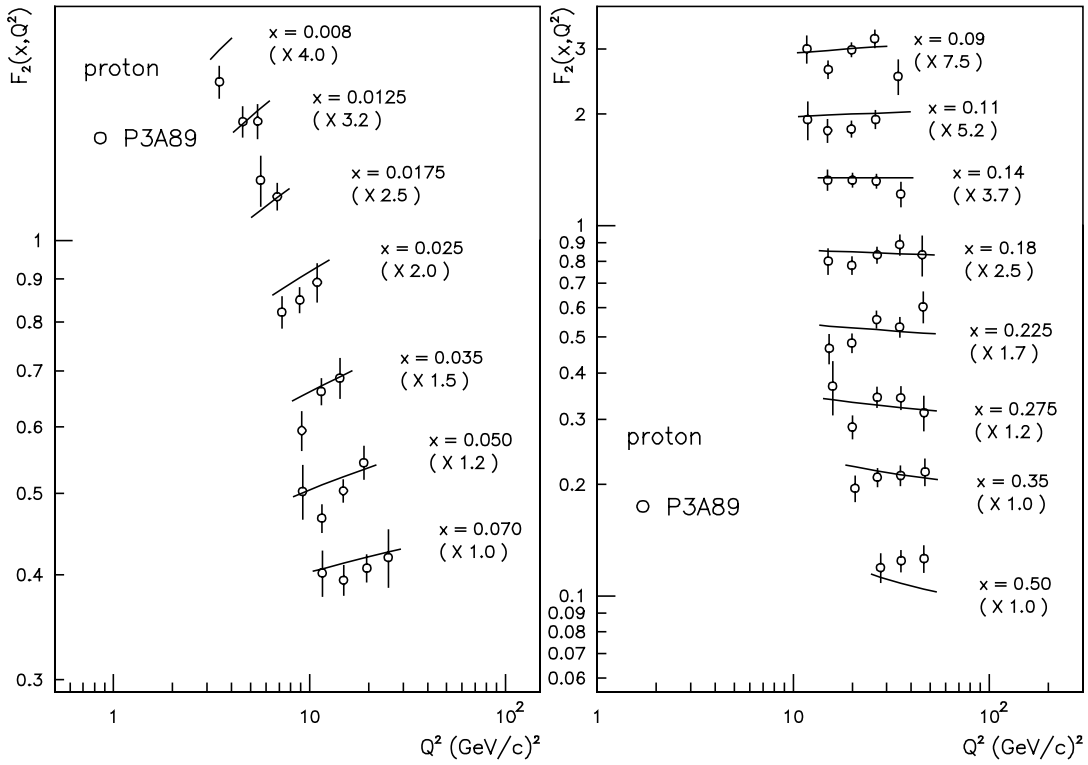

Figure 6.17:
The F_2 structure function of the proton versus Q^2 for each x_{Bj} bin, compared to the curves that represent the parametrizations taken from the BCDMS[2], NMC[4] and SLAC[1] data.

The results, as a function of x_{Bj} and Q^2, for the F_2 structure function of the deuteron are given in table 6.7 and seen in figure 6.18. The systematic errors are taken from the latest NMC F_2 publication[4]:

Table 6.7:
The deuteron structure function F_2^d. (Q^2 in $(\text{Gev/c})^2$)

Q^2	$F_2^d(x_{Bj},Q^2)$	Stat. error	Syst. error	Q^2	$F_2^d(x_{Bj},Q^2)$	Stat. error	Syst. error
At x_{Bj}=0.0080				At x_{Bj}=0.0700			
3.49	0.3812	0.0136	0.0142	11.62	0.3601	0.0186	0.0045
At x_{Bj}=0.0125				15.01	0.3642	0.0114	0.0042
4.55	0.4135	0.0140	0.0088	19.66	0.3836	0.0105	0.0046
5.43	0.4279	0.0158	0.0118	25.50	0.4144	0.0231	0.0057
At x_{Bj}=0.0175				At x_{Bj}=0.0900			
5.59	0.4078	0.0234	0.0080	11.73	0.3433	0.0249	0.0047
6.84	0.4326	0.0122	0.0085	15.08	0.3451	0.0143	0.0041
At x_{Bj}=0.0250				19.81	0.3399	0.0111	0.0039
7.24	0.3992	0.0133	0.0063	25.98	0.3860	0.0152	0.0046
8.91	0.4094	0.0107	0.0068	At x_{Bj}=0.1100			
10.90	0.4325	0.0168	0.0089	11.78	0.4043	0.0392	0.0060
At x_{Bj}=0.0350				15.00	0.3273	0.0185	0.0044
9.11	0.4042	0.0167	0.0055	19.91	0.3181	0.0121	0.0037
11.46	0.4068	0.0111	0.0057	26.40	0.3591	0.0142	0.0040
14.20	0.4500	0.0180	0.0078	34.29	0.4171	0.0325	0.0049
At x_{Bj}=0.0500				At x_{Bj}=0.1400			
9.27	0.3773	0.0233	0.0047	14.98	0.3134	0.0165	0.0046
11.57	0.3946	0.0115	0.0049	19.91	0.3188	0.0108	0.0040
14.84	0.3911	0.0091	0.0052	26.59	0.3082	0.0099	0.0035
18.93	0.4295	0.0141	0.0064	35.18	0.3490	0.0177	0.0039

Table 6.7 (continued):
The deuteron structure function F_2^d. (Q^2 in $(\text{Gev/c})^2$)

Q^2	$F_2^d(x_{Bj},Q^2)$	Stat. error	Syst. error	Q^2	$F_2^d(x_{Bj},Q^2)$	Stat. error	Syst. error
At x_{Bj}=0.1800				At x_{Bj}=0.2750			
14.98	0.2710	0.0185	0.0043	16.03	0.2506	0.0363	0.0031
19.83	0.2880	0.0122	0.0040	19.87	0.2206	0.0127	0.0025
26.53	0.2719	0.0104	0.0033	26.64	0.2334	0.0117	0.0029
35.19	0.3140	0.0145	0.0037	35.37	0.2383	0.0128	0.0031
45.22	0.2898	0.0259	0.0033	47.19	0.2570	0.0192	0.0044
At x_{Bj}=0.2250				At x_{Bj}=0.3500			
15.04	0.2697	0.0209	0.0042	20.67	0.1462	0.0099	0.0017
19.93	0.2415	0.0112	0.0033	26.81	0.1599	0.0072	0.0018
26.77	0.2591	0.0108	0.0034	35.38	0.1804	0.0083	0.0029
35.14	0.2638	0.0124	0.0033	46.61	0.1574	0.0100	0.0034
46.22	0.2727	0.0199	0.0035	At x_{Bj}=0.5000			
				27.92	0.0987	0.0068	0.0047
				35.50	0.0794	0.0043	0.0033
				46.96	0.0800	0.0054	0.0038

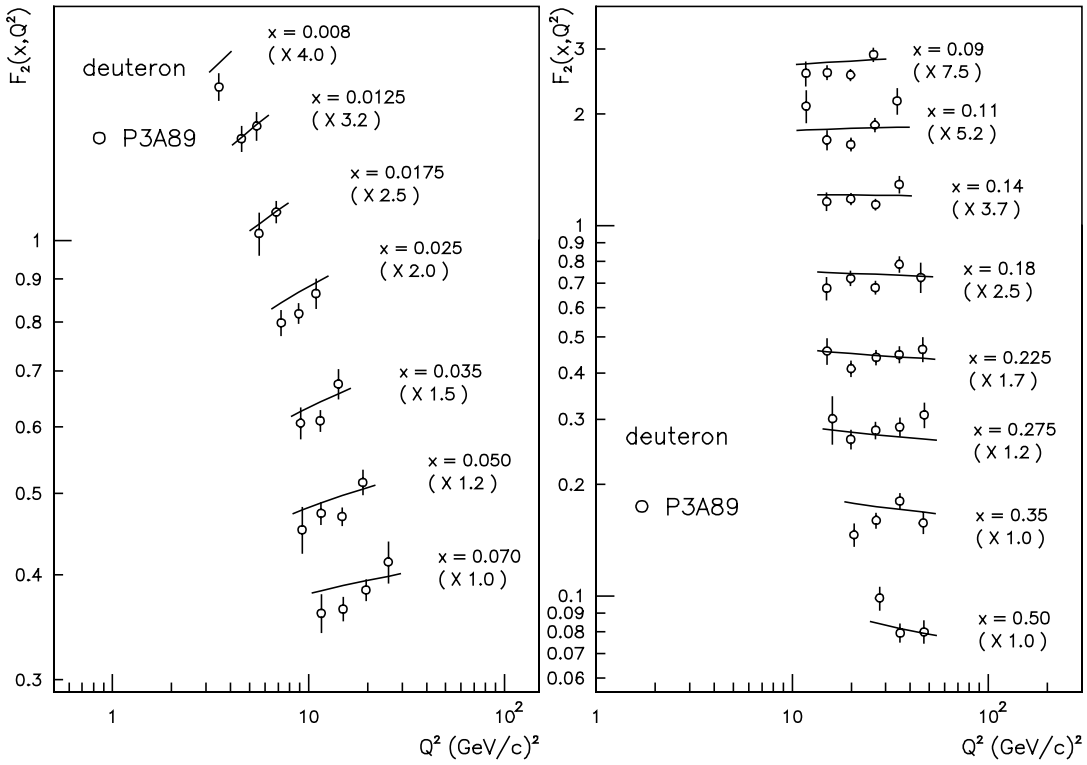

Figure 6.18:
The F_2 structure function of the deuteron versus Q^2 for each x_{Bj} bin, compared to the curves that represent the parametrizations taken from the BCDMS[2], NMC[4] and SLAC[1] data.

The contributions to the systematic errors are: the error from the radiative corrections; the errors due to the calibration of the energy of the incoming and scattered muons; the error due to the reconstruction efficiency; the error due to the input F_2 and the error in the knowledge of the acceptance. All of these contributions to the systematic error were added together in quadrature. The errors due to the calibration, the reconstruction efficiency and the acceptance should be the same as in the previous results[4]. However the errors due to the input F_2 and the radiative corrections should have improved since these results used the latest values from the latest NMC publication[4] as input. Therefore the systematic errors are taken from the latest NMC F_2 publication[4] (see appendix 8.3) and are used as an upper limit on the estimate of the systematic error given in both table 6.6 and table 6.7.

Structure functions F_2 at $Q^2 = 5\ (\mathrm{GeV/c})^2$ based on recent parton distributions parametrized from structure function data are shown in figure 6.19. These recent parametrizations were generated by the CERN program library's PDFLIB[5]. The two curves shown, (KMRS-B0)[6] and (MT-S1)[7], are constrained by precise data in the kinematic region $x_{Bj} \geq 0.07$, and fail to describe the behavior of the data in the lower x_{Bj} region. The third curve, (GRV)[8], is further constrained by experimental data thus giving a fair description of the present data. While the fourth, (MRS-D0)[9], was constrained by the latest NMC[4] data and therefore fits the data well, thus showing the improvement in the parametrization of F_2 brought about by the current data.

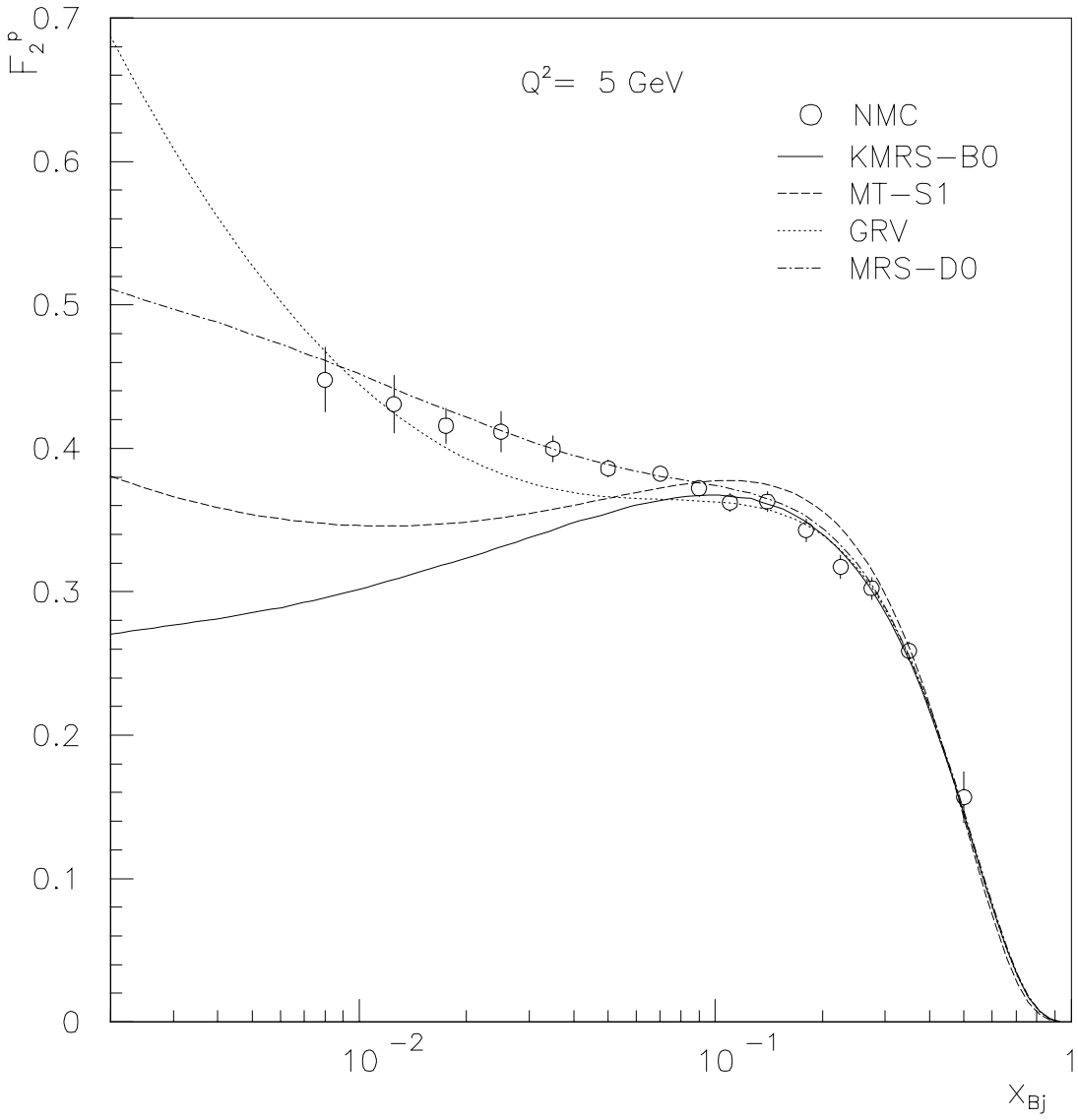

Figure 6.19:
Parametrizations of the proton structure function F_2.

In conclusion the structure function F_2 obtained from this period is in good agreement with the input value of F_2 and will thus add to the improvement in the errors of the overall NMC analysis. By extending the measurement of the F_2 structure function for the proton and deuteron over the kinematic range $0.006 < x_{Bj} < 0.6$ and $0.5 < Q^2 < 55\ (\mathrm{GeV/c})^2$, the data is seen to exhibit logarithmic scaling violations down to small values of x_{Bj}, even at low Q^2. Data in the low-x_{Bj} domain turned out to be essential for the proper determination of parton distributions.

References: Chapter 6

1 L. Whitlow *et al., Phys. Lett.* **B282** (1992) 475.

2 BCDMS, A. C. Benvenuti *et al., Phys. Lett.* **B223** (1989) 485;
BCDMS, A. C. Benvenuti *et al., Phys. Lett.* **B237** (1990) 592.

3 EMC-NA2, J. J. Aubert *et al., Nucl. Phys.* **B259** (1985) 189;
EMC-NA2, J. J. Aubert *et al., Nucl. Phys.* **B293** (1987) 740.

4 NMC, P. Amaudruz *et al., Phys. Lett.* **B295** (1992) 159.

5 H. Plothow-Besch, "Parton Density Functions", Proc. 3rd Workshop on detector and Event Simulations in High Energy Physics, Amsterdam, 8-12 April 1991;
Program PDFLIB; CERN Program Library Pool W5051 (1991).

6 J. Kwieciμski *et al., Phys. Rev. D* **42** (1990) 3645.

7 J. G. Morfin and W. K. Tung, *Z. Physik* **C52** (1991) 13.

8 M. Glück, E. Reya and M. Vogt, *Z. Physik* **C53** (1992) 127.

9` A. D. Martin, R. G. Roberts and W. J. Stirling, Durham Preprint, DTP/92-16 (1992).

7. Conclusion

The data presented in this thesis were obtained from the simultaneous measurement of deep inelastic muon scattering on hydrogen and deuterium targets at a nominal incident energy of 280 GeV. The data was from the SPS data taking period, P3A, of 1989. This data covered the kinematic range $0.002 \le x_{Bj} \le 0.80$ and $0.5 \le Q^2 \le 200\ (\mathrm{GeV/c})^2$. The data from the NMC experiment has cleared up the discrepancy between the EMC[1] and BCDMS[2] experimental results. The data presented in this thesis are in good agreement with previous NMC results[3]; therefore, similar conclusions can be drawn. These conclusions are presented here separately for the two main analysis subjects, the analysis of the ratio F_2^n/F_2^p and the analysis of the structure function F_2 for both the proton (F_2^p) and the deuteron (F_2^d).

7.1 F_2^n/F_2^p Ratio Analysis

The data used for the measurement of neutron and proton structure function ratio, F_2^n/F_2^p, covered the kinematic range $0.002 \le x_{Bj} \le 0.80$ and $0.5 \le Q^2 \le 200\ (\mathrm{GeV/c})^2$. The data are in good agreement with previous NMC results[4]. While having fewer statistics in only one period of data taking than those results, the systematic errors of the present data are similar in size and thus also small. The following conclusions can be made:

1) The x_{Bj} dependence of the ratio, averaged over Q^2, shows no evidence of sizable shadowing in deuterium. The ratio at the lowest measured value of x_{Bj} is consistent with unity.

2) The determination of $R^d - R^p$ was extended below the previous[5] range of $0.1 < x_{Bj} < 0.9$ to $x_{Bj} \ge 0.01$. The results are compatible with the previous NMC result[6]. These results show no x_{Bj}-dependence and are compatible with zero. They also are compatible with the predictions of perturbative QCD[7], within rather small errors.

3) The Gottfried Sum calculated for the data presented in this thesis is consistent with previous results[8] and is significantly less then the predicted[9] value of 1/3.

7.2 F_2 Structure Function Analysis

In conclusion the structure function F_2 calculated for this period is in good agreement with the input value of F_2 and will thus add to the improvement in the errors of the overall NMC analysis. The measurement of the F_2 structure function for the proton and deuteron has been extended over the kinematic range to $0.006 < x_{Bj} < 0.6$ and $0.5 < Q^2 < 55\ (\text{Gev/c})^2$ and so far some conclusions have been made[10]:

1) The data exhibit logarithmic scaling down to small values of x_{Bj}, even at low Q^2.

2) Where the data overlaps with the previous SLAC[11] and BCDMS[2] data, a good agreement between all three experiments is seen.

3) Prior to the inclusion of the NMC[10] data, the parametrizations[12] recently generated of parton distributions failed to describe the x_{Bj}-dependence of F_2 below x_{Bj}=0.07.

References: Chapter 7

1 EMC, J.J. Aubert *et al., Nucl. Phys.* **B259** (1985) 189;
EMC, J.J. Aubert *et al., Nucl. Phys.* **B293** (1987) 740.

2 BCDMS, A. C. Benvenuti *et al., Phys. Lett.* **B223** (1989) 485;
BCDMS, A. C. Benvenuti *et al., Phys. Lett.* **B237** (1990) 592.

3 NMC, D. Allasia *et al., Phys. Lett.* **B249** (1990) 366;
NMC, P. Amaudruz *et al., Nucl. Phys.* **B371** (1992) 3;
NMC, P. Amaudruz *et al., Phys Rev. Lett.* **66** (1991) 2712;
NMC, P. Amaudruz *et al.*, *Phys. Lett.* **B295** (1992) 159.

4 NMC, D. Allasia *et al., Phys. Lett.* **B249** (1990) 366;
NMC, P. Amaudruz *et al., Nucl. Phys.* **B371** (1992) 3.

5 L. W. Whitlow *et al., Phys. Lett.* **B250** (1990) 193.

6 NMC, P. Amaudruz *et al., Phys. Lett.* **B294** (1992) 120.

7 G. Altarelli and G. Martinelli, *Phys. Lett.* **B76** (1978) 89.

8 NMC, P. Amaudruz *et al., Phys Rev. Lett.* **66** (1991) 2712.

9 K. Gottfried, *Phys. Rev. Lett.* **18** (1967) 1174.

10 NMC, P. Amaudruz *et al.*, *Phys. Rev. Lett.* **B295** (1992) 159.

11 L. Whitlow *et al., Phys. Lett.* **B282** (1992) 475.

12 H. Plothow-Besch, "Parton Density Functions", Proc. 3rd Workshop on detector and Event Simulations in High Energy Physics, Amsterdam, 8-12 April 1991;
Program PDFLIB; CERN Program Library Pool W5051 (1991).

8. Appendix

To calculate the structure function ratio F_2^n/F_2^p both the density factor κ and the effect of the hydrogen-deuterium (HD) contamination must be determined. This is done in sections 8.1 and 8.2, respectively.

The contributions to the systematic errors of the structure functions F_2^p and F_2^d are given in section 8.3.

8.1. Determination of the density factor κ

The density factor κ is the ratio of the number of nucleons per unit area for the respective targets, and is defined as:

$$\kappa = \frac{\rho_p}{\rho_d} = \frac{n_p L_{H_2}}{n_d L_{D_2}} = \frac{V_{D_2}^{mol}}{L_{D_2}} \Big/ \frac{V_{H_2}^{mol}}{L_{H_2}} = \frac{V_{D_2}^{mol}}{V_{H_2}^{mol}} \frac{L_{H_2}}{L_{D_2}}, \tag{8.1}$$

where ρ is the density, n is the number of scattering centers per unit volume $n = N_0 / V^{mol}$, N_0 is Avogadro's number, V^{mol} is the molar volume (liters/mol) and L is the length of the target (mm). It should be noted that the value for $V_{D_2}^{mol}$ assumes pure deuterium and that the HD contamination is corrected for separately. The liquid hydrogen is considered to be pure. Since both the lengths of targets and their densities vary with the operating temperature, this temperature must be found.

With the fixed over-pressure, the operating pressure of the liquid targets was measured during the experiment; therefore, the respective operational temperatures of the liquid hydrogen and the liquid deuterium are determined from the Rutherford tables[1] of temperature as a function of the vapor pressure. The pressure of the targets was measured

and maintained such that: $P_{measured}$ is equal to the atmospheric pressure plus a constant over-pressure.

The Atmospheric pressure is measured at Geneva airport and then adjusted for the altitude. The altitude correction at the experimental area is 54±1 mbar[2]. The over-pressure was 125±5 mbar[3]. The over-pressure is maintained to insure that the temperatures of the target are kept at the boiling point, thus forcing the targets to be liquid.

The temperature and therefore the molar volume for the liquid hydrogen can be taken directly from the tables. However, because there was some contamination of the liquid D_2 by HD, the temperature of the liquid deuterium cannot be directly extrapolated from the measured pressure.

The measured pressure of the liquid deuterium is the sum of the partial pressures of D_2 and HD, such that: $P_{D_2 measured} = f_{D_2} P_{D_2} + f_{HD} P_{HD}$, where P_{D_2}, P_{HD}, f_{D_2} and f_{HD} are the pressures and the partial molar fractions of D_2 and HD respectively. The f_{HD} was measured to be : 0.0301±0.24%[4]; therefore, f_{D_2}=0.9699±0.24%. The temperature of the liquid hydrogen is calculated directly from the tables, while an iterative technique is used to calculate the temperature of the liquid deuterium[5].

Starting with the average measured pressure for period P3A89, of 1090.3 ± 5 mbar; the following results are given in table 8.1.

Table 8.1: Temperatures and Molar Volumes of H_2, D_2 and HD			
	H_2	D_2	HD
Temperature in K	20.52	23.84	23.84
Molar Volume in liters/mol	28.595	24.775	27.275

Then, from equation 8.1, the value for κ is:

$$\kappa = 0.86641\frac{L_H}{L_D}. \tag{8.2}$$

The lengths of the targets also change with temperature, using the formula: $L(T) = 3001 - 0.0447(291.15\text{K} - T) \pm 1$ mm[6]. This gives a value for the length of the hydrogen target of: $L_H = 2988.90 \pm 1$ mm and a value for the length of the deuterium target of: $L_D = 2989.05 \pm 1$ mm. So finally for P3A89 the value of κ is: $\kappa = 0.86637 \approx 0.8664$, while for 1986 and 1987 the average value is: $\kappa = 0.86635 \approx 0.8664$, showing good agreement.

For the maximum and minimum atmospheric pressures for the whole of 1989, κ changes only by ±0.0002 (±0.023%), therefore: κ =0.8664±0.0002.

8.2. Effect of the HD contamination of the target.

The correction for the HD contamination of D_2 is done in two parts, first with a correction to the molar volume, $V_{D_2}^{mol}$, and second with a correction to the number of events, N_d. The fraction of HD contamination along with the fraction of D_2 is determined from the following formulae:

$$f_{HD} = \frac{n_{HD}}{n_{HD} + n_{D_2}}, \tag{8.3}$$

$$f_{D_2} = \frac{n_{D_2}}{n_{HD} + n_{D_2}} = 1 - f_{HD}. \tag{8.4}$$

Where n in eqs. 8.3 and 8.4, is the numeric fraction of molecules in the mixture. n_{D_2} is the fraction of D_2 and n_d be the fraction of deuterium and $n_{HD} = n_p$ be the fraction of protons. So if: $n_d = 2n_{D_2} + n_{HD} = 2n_{D_2} + n_p$, and defining α such that:

$$\alpha = \frac{n_p}{n_p + n_d} = \frac{f_{HD}}{2}. \tag{8.5}$$

The actual molar volume, $V_{D_2}^{mol}$, in the targets is of the form: $V_{D_2mix}^{mol} = f_{D_2} V_{D_2}^{mol} + f_{HD} V_{HD}^{mol}$, therefore, the formula for the actual molar volume is:

$$V_{D_2mix}^{mol} = V_{D_2}^{mol} \frac{n_d}{1-\alpha} \left\{ 1 + 2\alpha \left(\frac{V_{HD}^{mol}}{V_{D_2}^{mol}} - 1 \right) \right\}. \tag{8.6}$$

By defining δ such that: $\delta = V_{HD}^{mol} / V_{D_2}^{mol}$. The correction to the molar volume is:

$$V_{D_2mix}^{mol} = V_{D_2}^{mol} \frac{n_d}{1-\alpha} \left(1 + 2\alpha(\delta - 1) \right). \tag{8.7}$$

The correction factor to κ for the molar volume, in terms of α, δ and the pure κ is:

$$\kappa_{mix} = \frac{V_{D_2mix}^{mol}}{V_{H_2}^{mol}} \frac{L_{H_2}}{L_{D_2}} = \kappa \frac{V_{D_2mix}^{mol}}{V_{D_2}^{mol}} = \kappa \frac{n_d}{1-\alpha} \left(1 + 2\alpha(\delta - 1) \right). \tag{8.8}$$

The correction to the number of deuterium events is in the form of partial fractions: $N_d^{mix} \propto \sigma_d^{mix} = n_d \sigma_d + n_{HD} \sigma_{HD} = n_d \sigma_d + n_p \sigma_p$. The formula for σ_d^{mix} is given as:

$$\sigma_d^{mix} = \sigma_d^{corr} \frac{n_d}{1-\alpha}\left(1+\alpha\left(\frac{\sigma_p}{\sigma_d}-1\right)\right). \tag{8.9}$$

By inverting the formula for σ_d^{mix}, the corrected ratio, σ_d/σ_p is:

$$\left[\frac{\sigma_d}{\sigma_p}\right]_{corr} = \frac{\sigma_d^{mix}}{\sigma_p}\frac{1-\alpha}{n_d}\left(1+\alpha\left(\frac{\sigma_p}{\sigma_d}-1\right)\right)^{-1}. \tag{8.10}$$

The formula for the measured ratio is really:

$$\frac{\sigma_d^{mix}}{\sigma_p} = \kappa^{mix}\sqrt{\frac{N_d^{up} N_d^{down}}{N_p^{up} N_p^{down}}}. \tag{8.11}$$

Then, by combining equations 8.8, 8.10 and 8.11, the formula for the true σ_d/σ_p ratio, corrected for the HD contamination, is:

$$\left[\frac{\sigma_d}{\sigma_p}\right]_{corr} = \kappa\sqrt{\frac{N_d^{up} N_d^{down}}{N_p^{up} N_p^{down}}}\frac{\left(1+2\alpha\left(\delta-1\right)\right)}{\left(1+\alpha\left(\frac{\sigma_p}{\sigma_d}-1\right)\right)}. \tag{8.12}$$

With κ=0.8664, α=0.0151 and δ=1.1009 and assuming that σ_p/σ_d is:

$$\frac{\sigma_p}{\sigma_d} = \left(\kappa\sqrt{\frac{N_d^{up} N_d^{down}}{N_p^{up} N_p^{down}}}\right)^{-1}. \tag{8.13}$$

A Taylor's expansion of the corrected σ_d/σ_p ratio is made and gives the approximation:

$$\left[\frac{\sigma_d}{\sigma_p}\right]_{corr} \approx 1.0182\left(0.8664\sqrt{\frac{N_d^{up} N_d^{down}}{N_p^{up} N_p^{down}}}\right) - 0.0151. \tag{8.14}$$

8.3. Contributions to the systematic errors.

The systematic errors were taken directly from a previous NMC publication[7] and each error is the quadratic sum of various contributions. These contributions are: RC, the error from the radiative corrections; E, E', errors due to calibrations of incident and scattered muon energies where the sign corresponds to an increase in energy; RE, error from the reconstruction efficiency correction; FN, error due to the functional form of the F_2 parametrization; AC, error in the knowledge of the acceptance.

The contributions to the total systematic errors for the structure funtion F_2^p, for each x_{Bj} and Q^2 bin, are given in table 8.2. The contributions to the total systematic errors for the structure funtion F_2^d, for each x_{Bj} and Q^2 bin, are given in table 8.3.

Table 8.2:
The contribution to the systematic errors of the structure function F_2^p.

Q^2 $(\mathrm{GeV/c})^2$	RC (%)	E (%)	E' (%)	RE (%)	FN (%)	AC (%)	Total (%)
At $x_{Bj} = 0.0080$							
3.47	3.0	0.4	0.1	1.1	1.2	3.4	4.8
At $x_{Bj} = 0.0125$							
4.56	1.3	0.5	0.0	0.8	0.1	2.8	3.2
5.43	2.9	0.4	0.1	1.1	0.5	2.7	4.2
At $x_{Bj} = 0.0175$							
5.62	0.7	0.5	0.0	0.8	0.3	2.4	2.7
6.84	1.3	0.5	0.1	0.8	0.1	2.5	3.0
At $x_{Bj} = 0.0250$							
7.22	0.4	0.6	0.0	0.8	0.4	1.7	2.1
8.92	0.8	0.5	0.0	0.8	0.3	1.8	2.2
10.93	2.0	0.4	0.1	1.1	0.1	1.8	2.9
At $x_{Bj} = 0.0350$							
9.12	0.3	0.6	-0.1	0.8	0.2	1.1	1.5
11.47	0.5	0.5	0.0	0.8	0.3	1.3	1.7
14.26	1.2	0.4	0.1	0.9	0.4	1.3	2.1
At $x_{Bj} = 0.0500$							
9.22	0.1	0.8	-0.2	0.8	0.1	0.3	1.2
11.55	0.2	0.7	-0.1	0.8	0.1	0.4	1.2
14.85	0.4	0.6	0.0	0.8	0.2	0.5	1.2
18.89	0.8	0.5	0.1	0.8	0.4	0.2	1.3
At $x_{Bj} = 0.0700$							
11.62	0.1	0.9	-0.3	0.8	0.0	0.3	1.3
14.92	0.1	0.7	-0.1	0.8	0.1	0.3	1.1
19.61	0.3	0.6	0.0	0.8	0.2	0.2	1.1
25.23	0.7	0.5	0.1	0.8	0.4	0.2	1.3

Table 8.2 (continued):
The contribution to the systematic errors of the structure function F_2^p.

Q^2 $(\mathrm{GeV/c})^2$	RC (%)	E (%)	E' (%)	RE (%)	FN (%)	AC (%)	Total (%)
At $x_{Bj} = 0.0900$							
11.72	0.0	1.0	-0.4	0.8	0.0	0.5	1.4
15.05	0.1	0.9	-0.2	0.8	0.0	0.6	1.4
19.84	0.2	0.7	-0.1	0.8	0.1	0.7	1.3
26.00	0.3	0.6	0.0	0.8	0.2	0.8	1.3
At $x_{Bj} = 0.1100$							
11.83	0.0	1.2	-0.6	0.8	0.1	0.6	1.7
14.95	0.0	1.0	-0.4	0.8	0.0	0.8	1.6
19.78	0.1	0.8	-0.2	0.8	0.0	1.0	1.5
26.30	0.2	0.7	0.0	0.8	0.1	1.1	1.5
34.28	0.3	0.5	0.1	0.8	0.2	1.1	1.5
At $x_{Bj} = 0.1400$							
14.97	0.0	1.2	-0.5	0.8	0.1	0.6	1.6
20.03	0.0	0.9	-0.3	0.8	0.0	0.9	1.5
26.52	0.1	0.8	-0.1	0.8	0.0	1.1	1.6
35.37	0.1	0.6	0.0	0.8	0.0	1.4	1.7
At $x_{Bj} = 0.1800$							
15.08	0.0	1.3	-0.7	0.8	0.1	0.3	1.7
19.88	0.0	1.1	-0.4	0.8	0.0	0.7	1.6
26.81	0.0	0.9	-0.2	0.8	0.0	1.0	1.6
34.94	0.1	0.8	-0.1	0.8	0.0	1.1	1.6
45.47	0.1	0.7	0.1	0.8	0.1	1.3	1.7

Table 8.2 (continued):
The contribution to the systematic errors of the structure function F_2^p.

Q^2 $(\mathrm{GeV/c})^2$	RC (%)	E (%)	E' (%)	RE (%)	FN (%)	AC (%)	Total (%)
At $x_{Bj} = 0.2250$							
15.24	0.0	1.4	-0.7	0.8	0.0	0.0	1.8
19.90	0.0	1.1	-0.4	0.8	0.0	0.2	1.4
26.59	0.0	0.9	-0.2	0.8	0.0	0.5	1.3
34.89	0.0	0.8	-0.1	0.8	0.0	0.7	1.3
45.91	0.1	0.7	0.1	0.8	0.0	0.8	1.3
At $x_{Bj} = 0.2750$							
15.88	0.0	1.1	-0.4	0.9	0.1	0.1	1.5
19.99	0.0	1.0	-0.2	0.8	0.0	0.1	1.3
26.77	0.0	0.8	-0.1	0.9	0.0	0.1	1.2
35.39	0.0	0.7	0.0	0.8	0.0	0.1	1.1
46.40	0.0	0.6	0.1	0.8	0.0	0.1	1.0
At $x_{Bj} = 0.3500$							
20.68	0.0	0.3	0.5	0.8	0.0	0.5	1.1
26.84	0.0	0.3	0.5	0.8	0.0	0.8	1.3
35.29	0.0	0.4	0.5	0.9	0.1	1.3	1.7
46.99	0.0	0.4	0.5	0.9	0.1	1.5	1.9
At $x_{Bj} = 0.5000$							
27.90	0.0	-2.4	3.4	0.8	0.7	2.4	4.9
35.52	0.0	-1.7	2.8	0.8	0.0	3.9	5.2
46.43	0.0	-1.1	2.3	0.8	0.0	5.6	6.2

Table 8.3:
The contribution to the systematic errors of the structure function F_2^d.

Q^2 $(\mathrm{GeV/c})^2$	RC (%)	E (%)	E' (%)	RE (%)	FN (%)	AC (%)	Total (%)
At $x_{Bj} = 0.0080$							
3.49	1.4	0.4	0.1	1.1	2.2	2.4	3.7
At $x_{Bj} = 0.0125$							
4.55	0.6	0.5	0.0	0.8	0.0	1.8	2.1
5.43	1.4	0.4	0.1	1.1	0.8	1.9	2.8
At $x_{Bj} = 0.0175$							
5.59	0.4	0.6	0.0	0.8	0.3	1.6	2.0
6.84	0.1	0.5	0.1	0.8	0.1	1.7	2.0
At $x_{Bj} = 0.0250$							
7.24	0.2	0.6	0.0	0.8	0.2	1.2	1.6
8.91	0.4	0.5	0.1	0.8	0.0	1.3	1.7
10.90	0.9	0.4	0.1	1.1	0.2	1.4	2.0
At $x_{Bj} = 0.0350$							
9.11	0.1	0.6	-0.1	0.8	0.1	0.9	1.4
11.46	0.3	0.5	0.0	0.8	0.1	1.0	1.4
14.20	0.7	0.4	0.1	0.9	0.3	1.2	1.7
At $x_{Bj} = 0.0500$							
9.27	0.1	0.8	-0.2	0.8	0.0	0.5	1.3
11.57	0.1	0.7	-0.1	0.8	0.1	0.6	1.2
14.84	0.1	0.6	0.0	0.8	0.3	0.8	1.3
18.93	0.2	0.5	0.1	0.8	0.5	1.0	1.5
At $x_{Bj} = 0.0700$							
11.62	0.0	0.9	-0.2	0.8	0.0	0.3	1.3
15.01	0.1	0.7	-0.1	0.8	0.1	0.4	1.1
19.66	0.1	0.6	0.0	0.8	0.2	0.6	1.2
25.50	0.3	0.5	0.1	0.8	0.5	0.8	1.4

Table 8.3 (continued):
The contribution to the systematic errors of the structure function F_2^d.

Q^2 $(\mathrm{GeV/c})^2$	RC (%)	E (%)	E' (%)	RE (%)	FN (%)	AC (%)	Total (%)
At $x_{Bj} = 0.0900$							
11.73	0.0	1.0	-0.4	0.8	0.1	0.2	1.4
15.08	0.0	0.8	-0.2	0.8	0.0	0.3	1.2
19.81	0.1	0.7	-0.1	0.8	0.0	0.4	1.1
25.98	0.1	0.6	0.1	0.8	0.2	0.6	1.2
At $x_{Bj} = 0.1100$							
11.78	0.0	1.1	-0.5	0.8	0.1	0.3	1.5
15.00	0.0	1.0	-0.3	0.8	0.1	0.3	1.4
19.91	0.0	0.8	-0.1	0.8	0.0	0.3	1.2
26.40	0.1	0.6	0.0	0.8	0.1	0.5	1.1
34.29	0.1	0.5	0.1	0.8	0.3	0.6	1.2
At $x_{Bj} = 0.1400$							
14.98	0.0	1.1	-0.4	0.8	0.1	0.3	1.5
19.91	0.0	0.9	-0.2	0.8	0.1	0.3	1.3
26.59	0.0	0.7	-0.1	0.8	0.0	0.4	1.1
35.18	0.1	0.6	0.1	0.8	0.1	0.5	1.1
At $x_{Bj} = 0.1800$							
14.98	0.0	1.2	-0.5	0.8	0.0	0.4	1.6
19.83	0.0	1.0	-0.3	0.8	0.1	0.4	1.4
26.53	0.0	0.8	-0.1	0.8	0.0	0.4	1.2
35.19	0.0	0.7	0.0	0.8	0.0	0.5	1.2
45.22	0.1	0.6	0.1	0.8	0.1	0.5	1.1

Table 8.3 (continued):
The contribution to the systematic errors of the structure function F_2^d.

Q^2 $(\mathrm{GeV/c})^2$	RC (%)	E (%)	E' (%)	RE (%)	FN (%)	AC (%)	Total (%)
At $x_{Bj} = 0.2250$							
15.04	0.0	1.2	-0.5	0.8	0.1	0.3	1.6
19.93	0.0	1.0	-0.3	0.8	0.0	0.4	1.4
26.77	0.0	0.8	-0.1	0.9	0.1	0.5	1.3
35.14	0.0	0.7	0.0	0.8	0.0	0.6	1.2
46.22	0.0	0.6	0.1	0.8	0.0	0.8	1.3
At $x_{Bj} = 0.2750$							
16.03	0.0	0.9	-0.2	0.8	0.2	0.1	1.3
19.87	0.0	0.8	0.0	0.8	0.0	0.2	1.1
26.64	0.0	0.7	0.1	0.9	0.0	0.5	1.2
35.37	0.0	0.6	0.2	0.8	0.0	0.8	1.3
47.19	0.0	0.6	0.2	0.9	0.0	1.2	1.7
At $x_{Bj} = 0.3500$							
20.67	0.0	0.1	0.8	0.8	0.2	0.3	1.2
26.81	0.0	0.2	0.7	0.8	0.0	0.4	1.2
35.38	0.0	0.3	0.6	0.8	0.1	1.2	1.6
46.61	0.0	0.3	0.6	0.8	0.0	1.9	2.2
At $x_{Bj} = 0.5000$							
27.92	0.0	-2.7	3.8	0.9	0.0	0.1	4.7
35.50	0.0	-1.9	3.1	0.9	0.0	1.8	4.2
46.96	0.0	-1.3	2.5	0.8	0.1	3.7	4.7

References: Appendix

1 R. J. Tapper, "Tables of Vapour Pressure and Molar Volume for Hydrogen and Deuterium", Rutherford Laboratory, Chilton, Didcot, Great Britain, NIRL/R/95 (1965).

2 C. Scholz, NMC Internal Report, NMC/89/3 (1989).

3 G. Bochaton, private communication via M. Siebler.

4 C. Scholz, NMC Internal Report, NMC/90/6 (1990).

5 D. Sanders, NMC Internal Report, NMC/92/1 (1992).

6 A. Milsom, NMC Internal Report, NMC/90/6 (1990).

7 NMC, P. Amaudruz *et al., Phys. Lett.* **B295** (1992) 159.